CONSEQUENCES OF MODE STRUCTURE ON PLASMA PARAMETERS IN ELECTRON CYCLOTRON RESONANCE SOURCES USED FOR MATERIALS PROCESSING

BY

RONALD LEONEL KINDER

B.S. University of Illinois at Urbana-Champaign, 1997
B.S. University of Illinois at Urbana-Champaign, 1997

THESIS

Submitted in partial fulfillment of the requirements
for the degree of Master of Science in Nuclear Engineering
in the Graduate College of the
University of Illinois at Urbana-Champaign, 1998

Urbana, Illinois

RED BORDER FORM

CONSEQUENCES OF MODE STRUCTURE ON PLASMA PARAMETERS IN ELECTRON CYCLOTRON RESONANCE SOURCES USED FOR MATERIALS PROCESSING

Ronald Leonel Kinder, M. S.
Department of Nuclear Engineering
University of Illinois at Urbana-Champaign, 1998
Mark J. Kushner, Advisor

Low pressure (<5 mTorr) electron cyclotron resonance (ECR) sources are being developed for downstream etching and deposition, and production of radicals for surface treatment. The spatial coupling of microwave radiation to the plasma in these systems is a concern due to issues related to the uniformity of dissociation, electron heating, and ultimately process uniformity.

To investigate these issues, a finite-difference-time-domain (FDTD) simulation for microwave injection and propagation has been developed. The FDTD simulation has been incorporated as a module in the 2-dimensional Hybrid Plasma Equipment Model (HPEM). In the FDTD simulation, plasma dynamics are coupled to the electromagnetic fields through a tensor form of Ohm's law. During each iteration through the model, the FDTD simulation uses a leap-frog scheme for time integration of Maxwell's equations, using time steps that are 30% of the Courant limit until a steady state is reached.

Studies suggest that certain electromagnetic modes provide better uniformity of ion fluxes to the wafer over larger areas and that obtaining uniform fluxes may require a power deposition profile that is peaked off-axis. It has been seen that lower order TE(0,n) circular modes tend to produce higher ion fluxes to the substrate, while higher order modes produce greater uniformity across the substrate.

Acknowledgements

I would like to acknowledge the Semiconductor Research Corporation (SRC), the National Science Foundation (NSF) and the Multidisciplinary University Research Initiative (MURI) for supporting this work.

I would like to give thanks to my advisor, Mark J. Kushner, for taking a lost soul and giving it direction. His patience, understanding, and wisdom has allowed me to grow professionally and personally.

I am also grateful to all my fellow, past and present, ODP comrades: Dr. Shahid Rauf, Dr. Eric Keiter, Dr. Robert Hoekstra, Xudong Xu, Da Zhang, Junqing Lu, Dan Cronin, Kelly Voyles, Dr. Michael Grapperhaus, Dr. Fred Huang, and Dr. Helen Hwang.

A special thanks goes to all those people who, at one time or another, have supported, encouraged and given me the strength to overcome the next obstacle. Papa Guayo, tia Pati, David, Ana, los Caceros, mi Julia, los Guerreros, and the infinitely many others for family members for demonstrating, even at a distance, that without each other we are nothing. To my beloved friends, Marcelo Venegas, Laura Vargas, Pancho Castelan, Luis Cortes, Derrick Garcia, the Chavez family, the Rodriguez family, the Messinger family, the Sebastians and the countless others that have given me the inspiration and courage to follow my dreams.

To my dearest Erica for believing in me, giving me faith anew, and for truly making me want to be a better man.

And finally, to my adoring mother, Elvira Oxom, who has performed the ultimate sacrifice. There are no words in our vocabulary that can express what you mean to me. Only through you have I achieved and only through you will I always persevere.

TABLE OF CONTENTS

I. Introduction

Current requirements for plasma processing of microelectronics devices include development of high plasma density sources that provide high deposition and etching rates, with enhanced process uniformity over large area wafers. Due to their ability to obtain a high degree of ionization and a relatively high electron temperature at low gas pressures, electron-cyclotron-resonance (ECR) sources are being developed for downstream etching and deposition, and production of radicals for surface treatment. Despite the widespread use for these sources, only recently have comprehensive numerical studies of ECR sources been performed. In order to begin optimizing these sources, an understanding of the ECR heating process must be obtained.

In an ECR discharge, an electromagnetic wave propagates along a dc magnetic field towards a resonance zone where the wave energy is absorbed by a collisionless heating mechanism. In a typical ECR reactor, a microwave field is transmitted through a window into a low pressure chamber. There is a decreasing static magnetic field in the processing chamber with $\omega_{ce}(z) > \omega$ at the window, where $\omega_{ce}(z)$ is the electron cyclotron frequency and ω is the applied microwave frequency. The use of a steady state magnetic field allows for operation at high density and low pressure without use of a cavity resonance provided there is a resonance between ω and ω_{ce} somewhere in the discharge. The fundamental components of the wave are the right-hand polarized (RHP) wave and the left-hand polarized (LHP) wave. With a significant plasma density ($> 10^{10}$ cm^{-3}) , the LHP is usually cutoff, while the RHP wave propagates and can be absorbed in the region of the cyclotron resonance. In the resonance zone, the conductivity has a Lorentzian line

shape with a full width at half maximum in the magnetic field corresponding to $\Delta\omega_{ce}$ equal to twice the electron collision frequency.[1] This dependence on collision frequency enables the efficient power transfer to the plasma at low pressures.

Efficient ECR coupling requires that the electron-neutral collision frequency be much smaller than the electron cyclotron frequency. Under these operating conditions, diffusion perpendicular to the magnetic field lines is reduced, thus reducing plasma losses to the wall. However, due to enhanced confinement of electrons by the static magnetic field lines, radial ionization profiles and charged particle densities tend to be strongly nonuniform. Such non-uniformities in ionization profiles and charge particle distributions will transfer to the ion fluxes reaching the substrate and eventually degrade flux uniformity.

The spatial coupling of microwave radiation to the plasma in ECR systems is a concern due to issues related to the uniformity of dissociation, electron heating, and ultimately process uniformity. The uniformity of the ion flux at the substrate depends strongly on the profile and location of the power deposition. Studies by Graves *et al.*[2] suggest that uniform conditions at the substrate surface appear to require a power profile peaked off-axis. Hidaka *et al.*[3] obtained similar results. Their studies showed that ECR plasma sources using a circular TE_{01} mode provide better uniformity over a larger area than that produced by conventional TE_{11} mode microwaves.[3] In the case of the TE_{11} mode, the electric field has a strong peak at the center of the waveguide. This may cause the peaking of the plasma density at the central region, while the plasma density near the sidewall decreases because of recombination of charged particles on the sidewall.[4] On the

other hand, the TE_{01} mode has a peak off axis. This strong electric field near the wall may compensate for recombination losses at the wall.

Considerable effort has been expended on numerical analysis and experimental measurements of microwave propagation in ECR plasmas. Stevens and Checchi[5] developed a predictive 1-D model by combining a simple plasma density model with a ray tracing method to achieve a first approximation to the self-consistent ECR system. Wu, Graves, and Kilgore[6] studied the behavior of compact 2-D ECR plasma sources by using a using a hybrid electron fluid particle ion and particle neutral model. In addition, non-uniform depletion of neutral gas was examined by using a 2D Monte Carlo method. Lieberman and Gottscho[7] used a spatially averaged global model based on particle and energy conservation to simulate ECR behavior.

In recent studies the finite-difference time-domain (FDTD) method has been used to study the electromagnetic fields inside a compact ECR source. For example, Muta *et al.*[8] has investigated microwave propagation in ECR plasmas by using a FDTD method. They performed one-dimensional simulations of the microwave propagation and discussed the characteristics of wave propagation through comparisons with their microwave ray tracing method measured by interferometry. Tan and Grotjohn[9] solved for electromagnetic fields inside an unmagnetized plasma-loaded microwave cavity reactor using the FDTD method using three-dimensional cylindrical coordinates. The electrical behavior of the discharge inside the reactor was modeled by solving the electron momentum transport equation. More recently Gopinath and Grotjohn[10] developed a three-dimensional electromagnetic particle-in-cell (PIC) model to simulate a compact ECR source. The FDTD technique was used to model the microwave fields. The PIC

technique was used to model the dynamics of both the electrons and the ions in the plasma.

To investigate some of the previously discussed issues, a FDTD simulation for microwave injection and propagation has been developed. The FDTD simulation was incorporated as a module in the 2-dimensional Hybrid Plasma Equipment Model (HPEM).[11-13] Plasma dynamics are coupled to the electromagnetic fields through a tensor form of Ohm's law. The FDTD simulation uses a leap-frog scheme for time integration, with time steps that are 30% of the Courant limit until reaching the steady state. Power deposition calculated in the FDTD module is then used in solving the electron energy equation.

1.2 References

1. M. A. Lieberman and A. J. Lichtenberg, Priciples of Plasma Discharges and Materials Processing, John Wiley and Sons, Inc., New York, 1994.
2. D. B. Graves, H. Wu, and R. K. Porteous, *Jpn. J. Appl. Phys.*, vol. 32, p. 2999, 1993.
3. R.Hidaka, T. Yamaguchi, N. Hirotsu, T. Ohshima, R. Koga, M. Tanaka, and Y. Kawai, *Jpn. J. Appl. Phys.*, vol. 32, p. 174, 1993.
4. H. Kim, Y. Tuchihashi, K. Matsuo, K. Muraoka, and M. Akazaki, *T. IEEE Jpn.*, 109-A, p. 149, 1989.
5. J. E. Stevens and J. L. Cecchi, *Jpn. J. Appl. Phys.*, vol. 32, p. 3007, 1993.
6. H. Wu, D. B. Graves, M. Kilgore, *Plasma Sources Sci. Technol.*, vol. 6, p. 231, 1997.
7. M. A. Lieberman and R. A. Gottscho, *Physics of Thin Films*, 1994.
8. H. Muta, T. Sakoda, Y. Ueda, and Y. Kawai, *Jpn. J. Appl. Phys.*, vol. 36, p. 872, 1997.
9. W. Tan and T. A. Grotjohn, *J. Vac. Sci. Technol. A*, vol. 12, p. 1216, 1994.
10. V. P. Gopinath and T. A. Grothjohn, *IEEE Transactions in Plasma Science*, vol. 23, p. 602, 1995.
11. P. L. G. Ventzek, M. Grapperhaus and M. J. Kushner, *J. Vac. Sci. Technol. B*, vol. 16, p. 3118, 1994.
12. M. J. Grapperhaus and M. J. Kushner, *J. Appl. Phys*, vol. 81, p. 569, 1997.
13. S. Rauf and M. J. Kushner, *J. Appl. Phys.*, vol. 81, p. 5966, 1997.

II. Model Description

2.1 Hybrid Plasma Equipment Model (HPEM)

The HPEM is a two-dimensional, plasma equipment model developed at the University of Illinois.[1-6] The HPEM has the capability of modeling complex reactor geometries and wide variety of operating conditions. The HPEM allows for a variety of plasma heating sources and gas chemistries. The base two-dimensional HPEM consists of an electromagnetic module (EMM), an electron energy transport module (EETM) and a fluid kinetics simulation (FKS). Electromagnetic fields and corresponding phases are calculated in the EMM. Specifics on the EMM module will be discussed in Section 2.4 Electromagnetic fields calculated in the EMM are used in the EETM to generate electron energy distribution functions as a function of position and phase. Methods on determining the electron distribution function will be discussed in Section 2.2. The electron distribution functions are used to generate sources for electron impact processes and electron transport coefficients. Parameters determined in the EETM are transferred to the FKS where momentum and continuity equations are solved for all heavy particles. A drift diffusion formulation is used for electrons to enable an implicit solution of Poisson's equation for the electric potential. The FKS solves for species densities and fluxes. Details of the FKS module will be discussed in Section 2.3. The species densities and electrostatic fields produced in the FKS are transferred to the EMCS and the EMM. These modules are iterated until a converged solution is obtained. A flowchart of the HPEM is shown in Figure 2.1. Note the HPEM has numerous other modules that are described in greater detail elsewhere.[1-6]

2.2 The Electron-Energy Transport Module (EETM)

The EETM solves for electron impact sources and electron transport properties by using electric and magnetic fields computed in the EMM and FKS. There are two methods for determining these parameters. The first method determines the electron temperature by solving the electron energy equation. The second method uses a Monte Carlo simulation for electron transport to gather statistics used to generate the electron energy distribution (eed) as a function of position.

The electron energy equation method first solves the zero order Boltzman equation for a range of predetermined Townsend values to create a table that provides an eed for each Townsend value. Once the eed isobtained, an average temperature, defined as $\frac{2}{3}$ $<\varepsilon>$, where $<\varepsilon>$ is the average energy, is computed from the eed. Electron mobility, thermal conductivity, energy loss rates due to collisions, and electron impact rate coefficients are also determined from the eed's.

With all these parameters known as a function of electron temperature, the following steady state electron energy equation is solved,

$$\nabla k \nabla T_e + \nabla \cdot \left(\Gamma T_e\right) = P_{heating} - P_{loss}, \qquad (2.2.1)$$

where T_e is the electron temperature, *k* is the thermal conductivity, Γ is the electron flux, $P_{heating}$ is the power deposition rate, and P_{loss} is the power loss to collisions. Equation (2.2.1) is solved by successive over relaxation, with transport coefficients being updated according to the local electron temperature.

The second method for determining electron transport properties is by the Electron Monte Carlo Simulation (EMCS). The EMCS simulates electron trajectories according to local electric and magnetic fields and collision processes. Initially the electrons are given a Maxwellian distribution and randomly distributed in the reactor weighted by the current electron density. Particle trajectories are computed using the Lorentz equation,

$$\frac{d\bar{v}}{dt} = \frac{q_e}{m_e}\left(\bar{E} + \bar{v} \times \bar{B}\right), \tag{2.2.2a}$$

and

$$\frac{d\bar{r}}{dt} = \bar{v}, \tag{2.2.2b}$$

where $\bar{v}$, $\bar{E}$, and $\bar{B}$ are the electron velocity, local electric field, and magnetic field respectively. Equations (2.2.2) are updated using a second order predictor corrector method. The electron energy range is divided into discrete energy bins. Within an energy bin, the collision frequency, ν_i, is computed by summing all the possible collisions within the energy range,

$$n_i = \left(\frac{2e_i}{m_e}\right)^{\frac{1}{2}} \sum_{j,k} s_{ijk} N_j, \tag{2.2.3}$$

where ε_i is the average energy within the bin, σ_{ijk} is the cross section at energy *i*, for species *j* and collision process *k*, and N_j is the number density of species *j*. The free-flight time is randomly determined from the maximum collision frequency. After the free-

flight, the type of collision is determined by the energy of the pseudoparticle. The corresponding energy bin in referenced and a collision is randomly selected from that energy bin, with a null reaction making up the difference between the maximum and actual collision frequency. At the end of the EMCS, the electron temperature, collision frequency and electron impact rate coefficients are determined by convolving the electron energy distribution function with the process cross section.

2.3 Fluid-Chemical Kinetics Simulation (FKS)

The FKS solves the fluid transport equations to provide species densities and fluxes. The module also includes chemical reactions and a solution of Poisson's equation and/or an ambipolar field solution for the electric potential and time-dependent electrostatic fields. Electron transport coefficients and electron impact rates needed to solve the fluid and potential equations are obtained from the EETM. Ion and neutral transport coefficients are obtained from a database or by using Lenard-Jones parameters.

The species densities are calculated from the continuity equation,

$$\frac{\partial N_i}{\partial t} = -\nabla \cdot \Gamma_i + S_i , \qquad (2.3.1)$$

where N_i, Γ_i, and S_i are the species density, flux, and source for species *i*. The flux for each species can be determined by using a drift diffusion or a heavy body momentum equation. Electron densities are determined using the drift diffusion formulation,

$$\Gamma_i = \mu_i q_i N_i \bar{E}_s - D_i \nabla N_i , \qquad (2.3.2)$$

where μ_i is the mobility of species *i*, D_i is the diffusion coefficient, q_i is the species charge in units of elementary charge, and E_s is the electrostatic field. Heavy ion and neutral fluxes can be determined by using the previous drift diffusion method or by using the heavy body momentum equation,

$$\frac{\partial \Gamma_i}{\partial t} = -\frac{1}{m_i}\nabla\left(N_i kT_i\right) - \nabla\cdot\left(N_i\,\bar{v}_i\bar{v}_i\right) + \frac{q_i}{m_i}N_i\bar{E} - \sum_j \frac{m_j}{m_i + m_j}N_i N_j\left(\bar{v}_i - \bar{v}_j\right)\nu_{ij}, \qquad (2.3.3)$$

where T_i is the species temperature, $\bar{v}_i$ is the species velocity given by Γ_i / N_i, and ν_{ij} is the collision frequency between species *i* and species *j*.

Solutions to Equations (2.3.2-2.3.3) requires knowledge of the local electrostatic fields. Electrostatic fields can be determined in two ways. The first method solves Poisson's equation for the electric potential. Using the drift diffusion equation, (2.3.2), an implicit form of Poisson's is,

$$\nabla\cdot\left(\left(\varepsilon - \Delta t\sigma + \Delta te\sum_i q_i{}^2\mu_i N_i{}^2\right)\nabla\phi^{t+\Delta t}\right) = -\rho^t + \Delta te\nabla\cdot\left(\sum_i q_i D_i \nabla N_i{}^t - \sum q_j\Gamma_j{}^t\right), \qquad (2.3.4)$$

where σ is the material conductivity and is nonzero only outside of the plasma region, *e* is elemental charge, q_i, μ_i, N_i, and Γ_i are the charge state, mobility, density, and the flux of species *i* at time *t*, respectively; Γ_j is the flux for species *j* at time *t*, and $\phi^{t+\Delta t}$ is the electric potential at time $t + \Delta t$. The summations over *i* are taken for those species using the drift diffusion formulation and the summation over *j* is taken for those species using

the momentum equation. Equation (2.3.4) is a modified form of Poisson's equation and is solved using the successive over relaxation (SOR) method. The time step taken in the charged-particle update requires that the fields do not reverse in a single time step. This is known as the dielectric relaxation time. It can be interpreted as the Courant limit on Poisson's equation. The implicit method described here allows the time steps to be larger than the dielectric relaxation time.

The second method for determining the electric potential uses an ambipolar approximation. Using this assumption, the electron density is computed assuming that the plasma is quasi-neutral at all points. The flux conservation equation can be written, after substituting the drift diffusion formulation,

$$\sum_i q_i \nabla \cdot \left(q_i n_i \mu_i \nabla \phi - D_i \nabla n_i \right) = \sum_i q_i S_i \,, \tag{2.3.5}$$

where S_i is the electron source function. Equation (2.3.5) can be rewritten to give an Poisson-like equation for the electrostatic potential,

$$\nabla \cdot \left(\sum_i q_1^{\,2} n_i \mu_i \nabla \phi \right) = \sum_i \left(q_1 D_i \nabla n_i \right) + \sum_i q_1 S_i \,, \tag{2.3.6}$$

where the summation is now taken over all the charged species, including electrons. This Poisson-like equation is discretized and solved using a SOR method. By solving for the electrostatic potential using the ambi-polar approximation the time step is only limited by the Courant limit.

2.4 The Electromagnetic Module (EMM)

In the current model developed here, the electromagnetic fields, $E(r,z,f)$ and $B(r,z,f)$, are solved for in the entire volume of the reactor using a FDTD method starting with the following forms of Maxwell's equations,

$$\nabla \times \overline{\mathrm{E}} = - \frac{\partial \overline{\mathrm{B}}}{\partial t}, \tag{2.4.1a}$$

$$\nabla \times \overline{\mathrm{H}} = \overline{\mathrm{J}} + \frac{\partial \overline{\mathrm{D}}}{\partial t}, \tag{2.4.1b}$$

$$\nabla \cdot \overline{\mathrm{D}} = \rho . \tag{2.4.1c}$$

Using the assumption of charge neutrality (ρ=0) and that the dielectric parameters μ, σ, and ε are independent of time, we consider a 2-dimensional, cylindrical grid with electromagnetic components of the following form,

$$\overline{\mathrm{E}}(r,z) = \mathrm{E}_\theta \hat{q}, \tag{2.4.2a}$$

$$\overline{\mathrm{B}}(r,z) = \mathrm{B}_r \hat{\mathrm{r}} + \mathrm{B}_z \hat{\mathrm{z}}. \tag{2.4.2b}$$

Substituting into Equations (2.4.1) the following system of equations are obtained. These are equivalent to Maxwell's equations in a cylindrical coordinate system (r, q, z),

$$\frac{\partial \mathrm{E}_q}{\partial t} = \frac{1}{me}\left(\frac{\partial \mathrm{B}_r}{\partial z} - \frac{\partial \mathrm{B}_z}{\partial r}\right) - \frac{|\overline{s}|}{e}\mathrm{E}_q , \tag{2.4.3a}$$

$$\frac{\partial B_r}{\partial t} = \frac{\partial E_q}{\partial z}, \tag{2.4.3b}$$

$$\frac{\partial B_z}{\partial t} = -\frac{1}{r}\frac{\partial (rE_q)}{\partial r}. \tag{2.4.3c}$$

In Equations (2.4.3), the following identities, $\bar{J} = \bar{\bar{\sigma}} \cdot \bar{E}$, $\bar{B} = m\bar{H}$, and $\bar{D} = e\ \bar{E}$ were used. The transverse electric fields (TE) used in the simulations have $\bar{k} \cdot \bar{E} = 0$, with components E_θ, B_r, and B_z as previously shown. The spatial locations of components of $\bar{E}$ and $\bar{B}$ may be chosen so as to provide centered spatial differencing. The simulations performed here use an alternating direction implicit scheme with a $2\frac{1}{2}$ dimension alternating grid. Azimuthal electric fields are calculated at grid points, while magnetic fields are calculated at locations shifted by half a grid cell, as shown in Figure 2.2.

The FDTD simulation uses a leap-frog scheme for time integration of Maxwell's equations. The electric fields are calculated at time t and the magnetic fields are calculated at time $t + \Delta t/2$. The finite differencing representation of Maxwell's equations is given by,

$$\frac{E_\theta(i,j)^{t+\Delta t} - E_\theta(i,j)^{t}}{\Delta t} = \frac{1}{\mu\varepsilon}\left(\frac{B_r(i,j+\frac{1}{2}) - B_r(i,j-\frac{1}{2})}{\Delta z} - \frac{B_z(i+\frac{1}{2},j) - B_z(i-\frac{1}{2},j)}{\Delta r} \right)^{t+\frac{\Delta t}{2}} - \frac{\sigma}{\varepsilon} E_\theta(i,j)^{t+\Delta t}, \tag{2.4.4a}$$

$$\frac{B_r(i, j+\frac{1}{2})^{t+\frac{\Delta t}{2}} - B_r(i, j+\frac{1}{2})^{t-\frac{\Delta t}{2}}}{\Delta t} = \frac{E_\theta(i, j+1) - E_\theta(i, j)}{\Delta z}, \qquad (2.4.4b)$$

$$\frac{B_z(i+\frac{1}{2}, j)^{t+\frac{\Delta t}{2}} - B_z(i+\frac{1}{2}, j)^{t-\frac{\Delta t}{2}}}{\Delta t} = \frac{\left(r(i+1, j)\, E_\theta(i+1, j) - r(i, j)\, E_\theta(i, j)\right)}{\left(r(i, j) + \frac{\Delta r}{2}\right)\Delta r}, \qquad (2.4.4c)$$

where r ,σ, μ, and ε are the radius, conductivity, permittivity and permeability of the medium, respectively, at location (i, j) [Note: (i, j) corresponds to (r,z)]. Δr and Δz are the grid sizes in the r- and z- directions and Δt is the integration time step. The Courant condition on the allowed time step for time integration is given by

$$\left(\frac{1}{\Delta r^2} + \frac{1}{\Delta z^2}\right)^{-\frac{1}{2}} \frac{1}{c} > \Delta t \ , \qquad (2.4.4)$$

where c is the speed of light in the medium.

The conduction current density, $\bar{J}$, in the plasma is related to the electron drift velocity, $\bar{v}$, by,

$$\bar{J} = q\, n_e\, \bar{v}, \qquad (2.4.5)$$

where n_e is the plasma density. To obtain an expression for $\bar{v}$, a first moment is formed by multiplying the Boltzmann equation by $\bar{v}$ and integrating over velocity. Assuming a

Maxwellian distribution function and neglecting pressure gradients, the drift velocity is obtained from,

$$\frac{d\bar{v}}{dt} = \frac{q}{m}(\bar{E} + \bar{v} \times \bar{B}) - n_m \bar{v}, \tag{2.4.6}$$

where ν_m is the electron momentum transfer collision frequency. The electric fields and currents are assumed to be driven harmonically at a frequency ω (rads/s) and are represented by a traveling wave propagating in the $\hat{z}$ direction,

$$\bar{E}(r,z) = E_0(r,z) \exp(i(\omega t - kz)), \tag{2.4.7a}$$

$$\bar{J}(r,z) = J_0(r,z) \exp(i(\omega t - kz)) = q\, n_e\, v_0(r,z) \exp(i(\omega t - kz)). \tag{2.4.7b}$$

Substituting Equation (2.4.7) into Equation (2.4.6), the following is obtained,

$$a\bar{v} = \bar{E} + \bar{v} \times \bar{B}, \tag{2.4.8}$$

where $\alpha = m/q\,(i\omega + \nu_m)$. Equation (2.4.8) can be written in the following form,

$$\bar{v} = \bar{\bar{M}}^{-1} \cdot \bar{E}, \tag{2.4.9}$$

where

$$\bar{\bar{M}} = \begin{pmatrix} a & -B_z & B_q \\ B_z & a & -B_r \\ -B_q & B_r & a \end{pmatrix}. \tag{2.4.10}$$

Combining Equation (2.4.9) with Equation (2.4.5), a tensor form of Ohm's law is obtained,

$$\bar{J} = q\, n_e\, \bar{v} = q\, n_e\, \bar{\bar{M}}^{-1} \cdot \bar{E} = \bar{\bar{\sigma}} \cdot \bar{E}\,. \tag{2.4.11}$$

Since B_θ, E_r, and E_z are zero, equation (2.4.11) can be expanded as,

$$\begin{pmatrix} J_r \\ J_\theta \\ J_z \end{pmatrix} = \frac{q\, n_e}{\alpha\left(\alpha^2 + B_r{}^2 + B_z{}^2\right)} \begin{pmatrix} \left(\alpha^2 + B_r{}^2\right) & B_z\alpha & B_r B_z \\ -B_z\alpha & \alpha^2 & B_r\alpha \\ B_r B_z & -B_r\alpha & \left(\alpha^2 + B_z{}^2\right) \end{pmatrix} \begin{pmatrix} 0 \\ E_\theta \\ 0 \end{pmatrix}. \tag{2.4.12}$$

The azimuthal conduction current density, J_θ, is,

$$J_\theta = \frac{q\, n_e}{\alpha\left(\alpha^2 + B_r{}^2 + B_z{}^2\right)}\, \alpha^2\, E_\theta\,. \tag{2.4.13}$$

To incorporate J_θ into Maxwell's equations, only the real component is considered. This is justified by the fact that Maxwell's equations represent real, instantaneous fields. If an electric field is used to excite a gas discharge or to heat the electrons, then the energy absorbed is proportional to the real part of the conductivity. The real component of Equation (2.4.13) is,

$$\mathrm{Re}\left[J_q\right] = \left[\frac{1 + \dfrac{w^2 + w_{cyc}^{\ 2}}{n_m^{\ 2}}}{\left[1 + \dfrac{w_{cyc}^{\ 2} - w^2}{n_m^{\ 2}}\right]^2 + \left[\dfrac{2w}{n_m}\right]^2}\right]\left(\frac{q^2 n_e}{m_e n_m}\right)E_q\,, \qquad (2.4.14)$$

where $\omega_{cyc} = q\,|B_{tot}| / m_e$, is the magnitude of the cyclotron frequency. This equation is identical to that presented by Cherrington.[7] If the collision frequency is reasonably small with respect to the frequency of the electromagnetic field ($\nu_m^{\ 2} << \omega^2$) and if the electromagnetic frequency approaches the cyclotron frequency, then

$$\mathrm{Re}\left[s_\perp\right] \approx \frac{q^2 n_e n_m}{2 m_e}\left[\frac{1}{n_m^{\ 2} + (w - w_{cyc})^2}\right]. \qquad (2.415)$$

If $\omega = \omega_{cyc}$ the conductivity peaks in a resonant manner and exhibits a Lorentzian line shape with a full width at half maximum of $2\nu_m$. The peak in the conductivity can be understood as the condition under which the motion of the electron in the magnetic field is synchronous with the driving electromagnetic field, setting up a condition under which the electron continuously gains energy from the electric field. This is analogous to the conditions achieved in a steady state electric field where the velocity of the electrons (or the current) is impeded by collisions ($\mathrm{Re}[\sigma] \sim 1/\nu_m$). Hence, collisions limit the amount of energy absorbed by electrons, but transfer electron energy to the neutral gas. The absorption of the microwave energy is by both ions and electrons. However, since work the done on a charged particle by an electric field varies inversely as the particle mass, the energy imparted to an electron is significantly greater than the energy imparted to an

ion. Therefore, direct energy transfer from the incident electric fields to the ions can be neglected here. Transfer of the electromagnetic energy to the neutral gas takes place through Joule (elastic and inelastic heating) following electron cyclotron heating of the electron gas.

The total power per unit volume delivered to the plasma by the electromagnetic field is,

$$\langle P \rangle_{absorbed} = \frac{1}{2} \mathrm{Re}\left[\mathbf{E} \cdot \bar{\bar{\sigma}} \mathbf{E}^{*} \right], \tag{2.4.16}$$

where $\mathbf{E}$ is the complex electric field. Expanding the product in Equation (2.4.16), and considering only the azimuthal component, the power deposited in the plasma is,

$$\langle P \rangle_{absorbed} = \frac{1}{2} s_{\perp} \left| E_q \right|^2 . \tag{2.4.17}$$

The phases of the electric field, needed in the EETM, are calculated by performing a Discrete Fourier Transform (DFT) of the electric fields over one microwave cycle. The DFT is performed after the fields have converged. Convergence is assumed to occur after the incident waves have traversed the reactor several times. During the calculation of the DFT, the time step is adjusted to incorporate enough temporal points to resolve the DFT. The phase is then computed as the imaginary part of the DFT divided the real part of the DFT.

The DFT is calculated by,

$$E(k) = \sum_{n=0}^{N-1} E_{\theta}(n)\, e^{-j\left(\frac{2\pi}{N}\right)kn}, \qquad (2.4.18)$$

where $E(k)$ is the DFT of the electric field, k is the harmonic number, and N is an appropriately large integer to achieve proper temporal resolution. For these simulations the fundamental harmonic, k = 1, was used along with N = 100 temporal points. The phase was then calculated as,

$$\phi(i, j) = \frac{\mathrm{Im}[E(i, j, k=1)]}{\mathrm{Re}[E(i, j, k=1)]}, \qquad (2.4.19)$$

where Im[E(i,jk=1)] and Re[E(i,jk=1)] are the imaginary and real parts of the DFT, respectively.

When time domain electromagnetic fields are obtained using finite difference techniques in an unbounded space, there must ultimately be a method of limiting the domain in which the field is computed. This is achieved here by truncating the mesh and using absorbing boundary conditions at those artificial boundaries which simulates the unbounded space. Due to the nature of the $2\frac{1}{2}$ dimension alternating direction implicit scheme, boundary conditions which use constant gradients for electromagnetic fields cause spurious reflections of the incident waves. To remove these unwanted reflections back into the waveguide a linearized first order wave equation was imposed as a boundary condition to simulate empty space,

$$\frac{\partial E_\theta{}^{n+1}}{\partial z} + \frac{\partial E_\theta{}^{n}}{\partial z} = \frac{1}{c}\left(\frac{\partial E_\theta(i, j)}{\partial t} + \frac{\partial E_\theta(j-1)}{\partial t} \right). \tag{2.4.20}$$

In these simulations, the system of interest uses circular TE(0,n) microwave mode fields injected along the axis of a cylindrically symmetric downstream reactor to excite the plasma. The complex electric and magnetic field components for circular TE mode waves as,

$$E_\theta = A_{mn} \frac{\beta_r}{\varepsilon} J'_m(\beta_r r)[C_2 \cos(m\phi) + D_2 \sin(m\phi)]\exp(-j\beta_r z), \tag{2.4.21a}$$

$$H_\rho = -A_{mn} \frac{\beta_z \beta_r}{\omega\mu\varepsilon} J'_m(\beta_r r)[C_2 \cos(m\phi) + D_2 \sin(m\phi)]\exp(-j\beta_r z), \tag{2.4.21b}$$

$$H_z = -jA_{mn} \frac{\beta_r{}^2}{\omega\mu\varepsilon} J_m(\beta_r r)[C_2 \cos(m\phi) + D_2 \sin(m\phi)]\exp(-j\beta_r z), \tag{2.4.21c}$$

where E_θ, H_r, and H_z, are the complex azimuthal electric field, radial magnetic field intensity, and axial magnetic field intensity, respectively, and $J(\beta_r r)$ and $J'(\beta_r r)$ are the Bessel functions and their derivatives.[8] Likewise β_r is defined as,

$$\beta_r = \frac{\chi'_{mn}}{a}, \tag{2.4.22}$$

where χ'_{mn} is the zeroes of $J'(\beta_r a)$ and a is the radius of the waveguide.

In this work, $m = 0$ and $z = 0$. The instantaneous field vectors are given by the real part of the product of the complex field and the time harmonic variation $e^{-j\omega t}$. Incident waves having these amplitudes were introduced as a boundary condition on a dielectric window. These fields produce electric field distributions which are zero on the axis of symmetry and the metallic edges of the waveguide, and have a peak off axis. The number of nodes between the axis of symmetry and the waveguide edge will vary accordingly to the mode of excitation. Typical electric fields are shown in Figure 2.3 for modes $n = 1$ and $n = 2$.

The effects of absorbing boundary conditions are shown in Figure 2.4. A circular transverse electric TE(0,1) field mode, operating at 3.0 GHz, was injectedat the top (z=50 cm) of a metallic waveguide and propagates towards the bottom (z=0 cm) of the open ended waveguide. In case (a), a constant electric field gradient boundary condition was imposed at the bottom of the waveguide. As the electromagnetic wave reached the lower boundary, the imposed boundary condition pinned the electromagnetic field at zero thereby causing a spurious reflection of the incident wave. The reflected wave combined with the incident wave to create a standing wave pattern, as can be seen in Figure 2.4. In case (b), a linearized first order wave equation was imposed as a boundary condition to simulate unbounded surroundings. In this case, spurious reflections of the incident wave were removed.

2.6 References

1. P. L. G. Ventzek, R. J. Hoekstra and M. J. Kushner, *J. Vac. Sci. Technol. B*, vol. 12, p. 416, 1993.
2. P. L. G. Ventzek, M. Grapperhaus and M. J. Kushner, *J. Vac. Sci. Technol. B*, vol. 16, p. 3118, 1994.
3. W. Z. Collison and M. J. Kushner, *Appl. Phys. Lett.*, vol. 68, p. 903, 1996.
4. M. J. Kushner, W. Z. Collison, M. J. Grapperhaus, J. P. Holland and M. S. Barnes, *J. Appl. Phys.*, vol. 80, p. 1337, 1996.
5. M. J. Grapperhaus and M. J. Kushner, *J. Appl. Phys*, vol. 81, p. 569, 1997.
6. S. Rauf and M. J. Kushner, *J. Appl. Phys.*, vol. 81, p. 5966, 1997.
7. B. E. Cherrington, Gaseous Electronics and Gas Lasers, Pergamon Press, New York, 1979.
8. C. A. Balanis, Advanced Engineering Electromagnetics, John Wiley & Sons, New York, 1989.

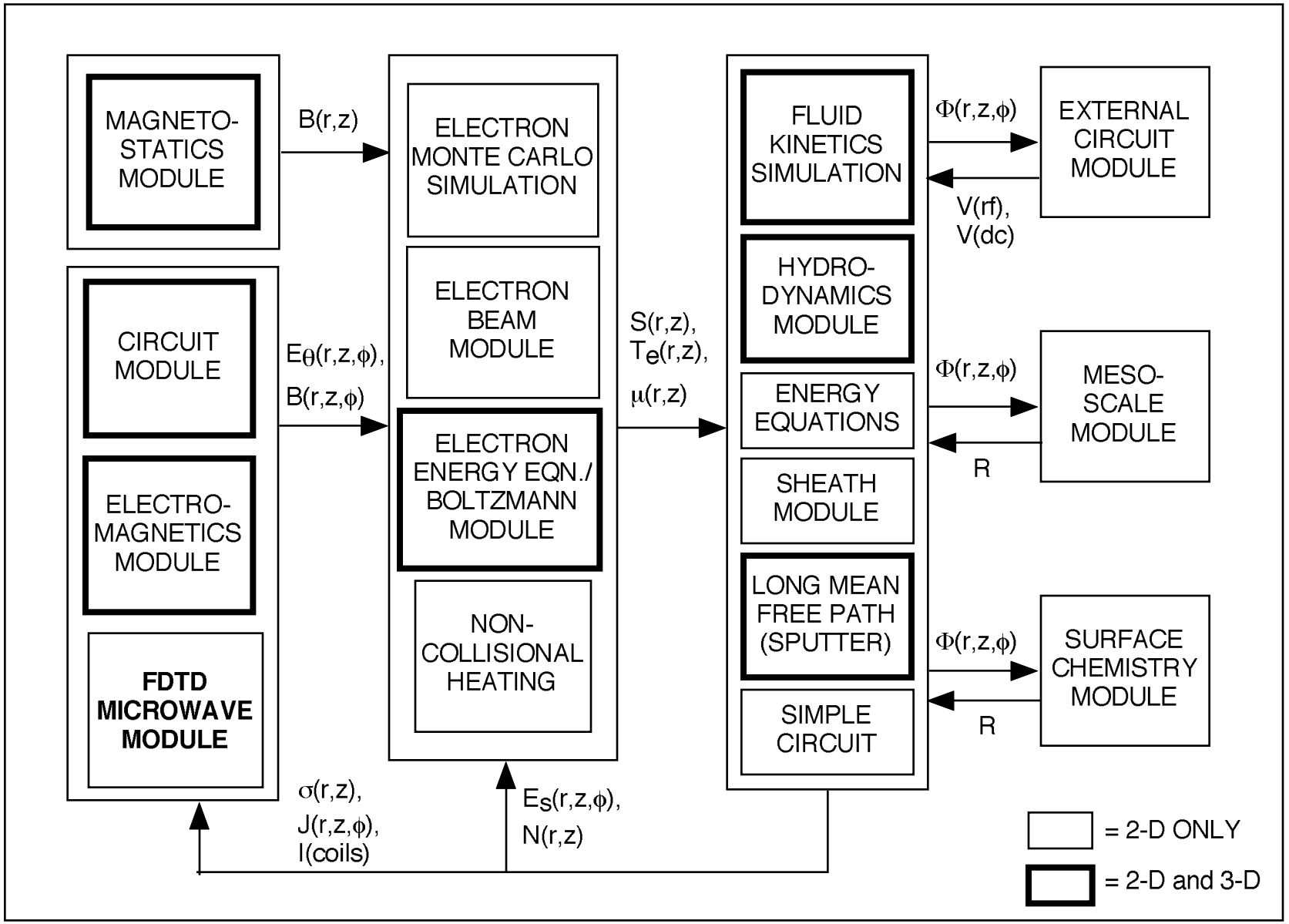

Figure 2.1 Flow chart of Hybrid Plasma Equipment Model (HPEM)

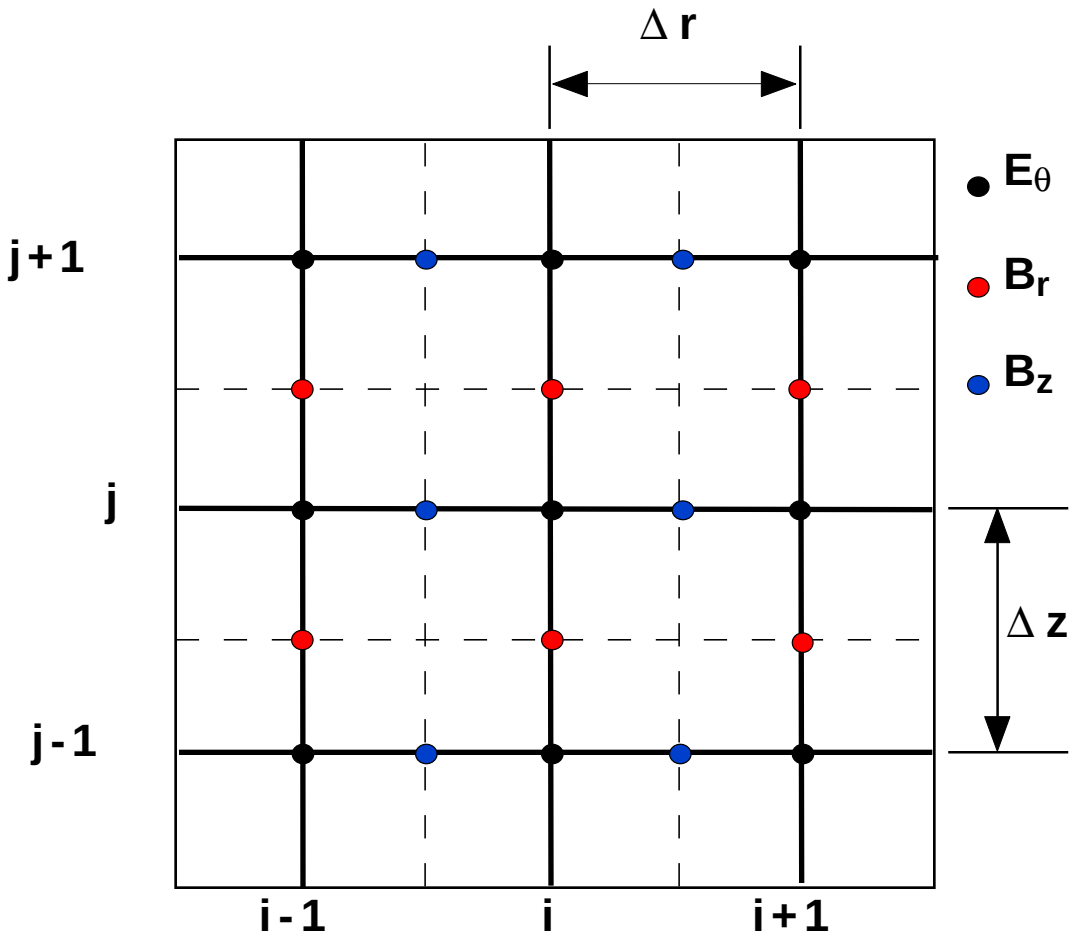

Figure 2.2 Grid locations for azimuthal electric field, axial magnetic field, and radial magnetic field in the alternating direction implicit scheme.

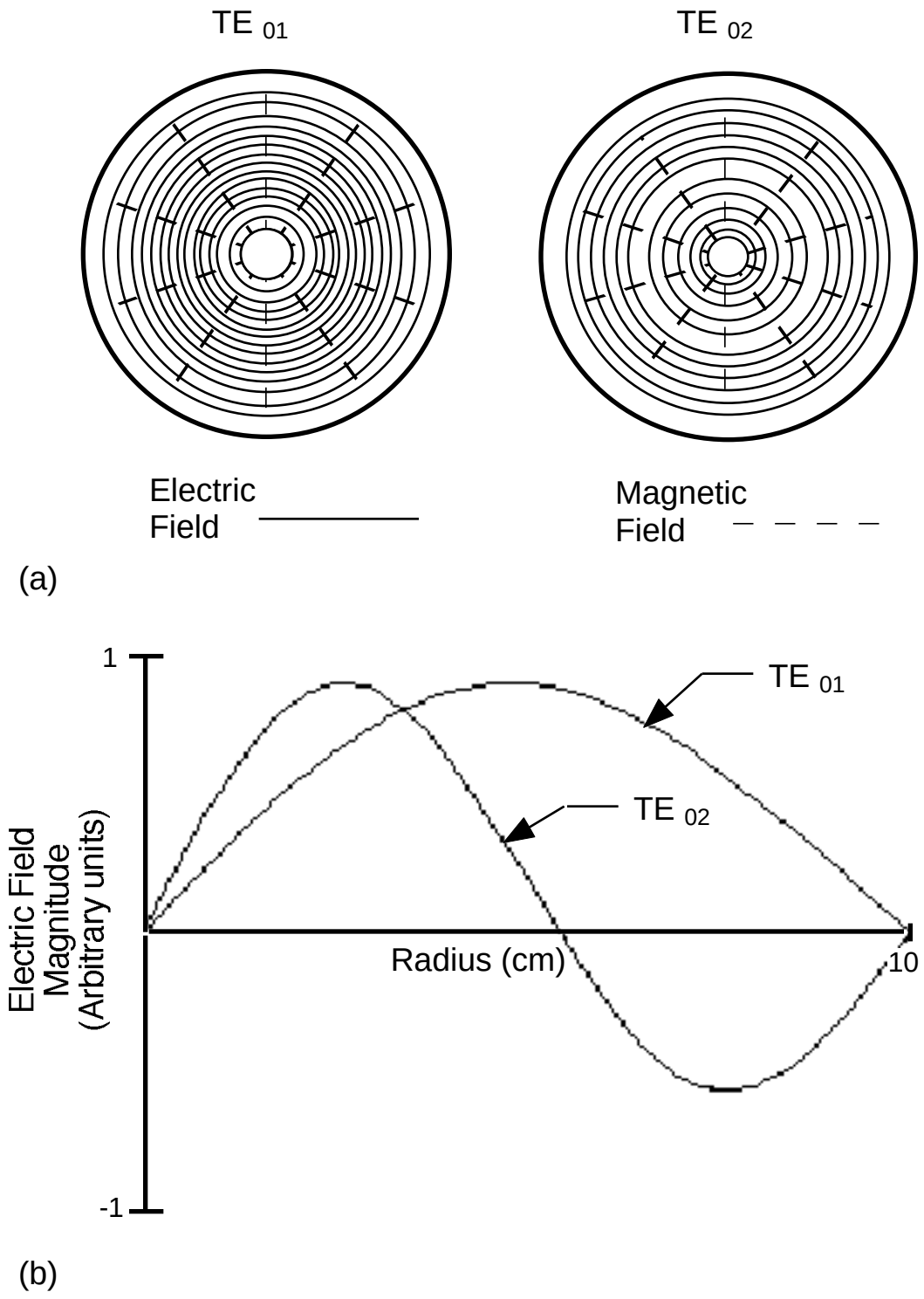

Figure 2.3 (a) Electric and magnetic field distributions for TE_{01} and TE_{02} modes as seen along the direction of propagation. (b) Radial electric field magnitude for TE_{01} and TE_{02} modes.

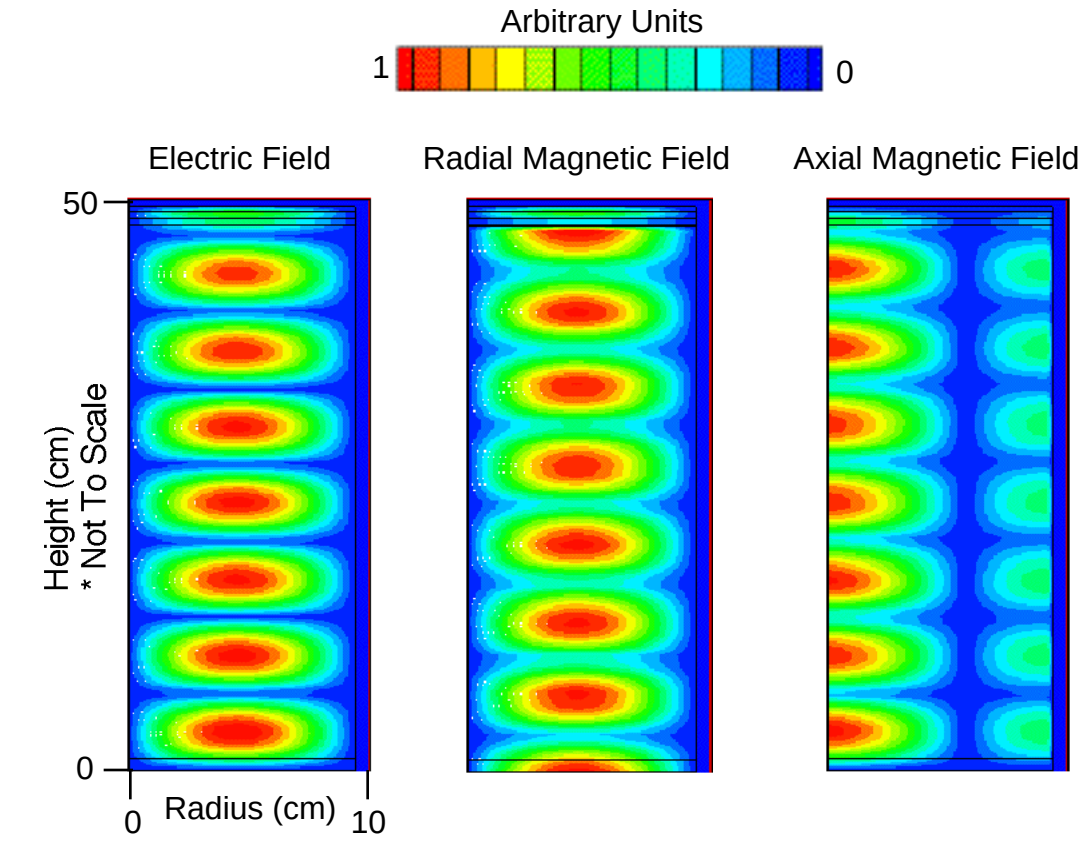

a)

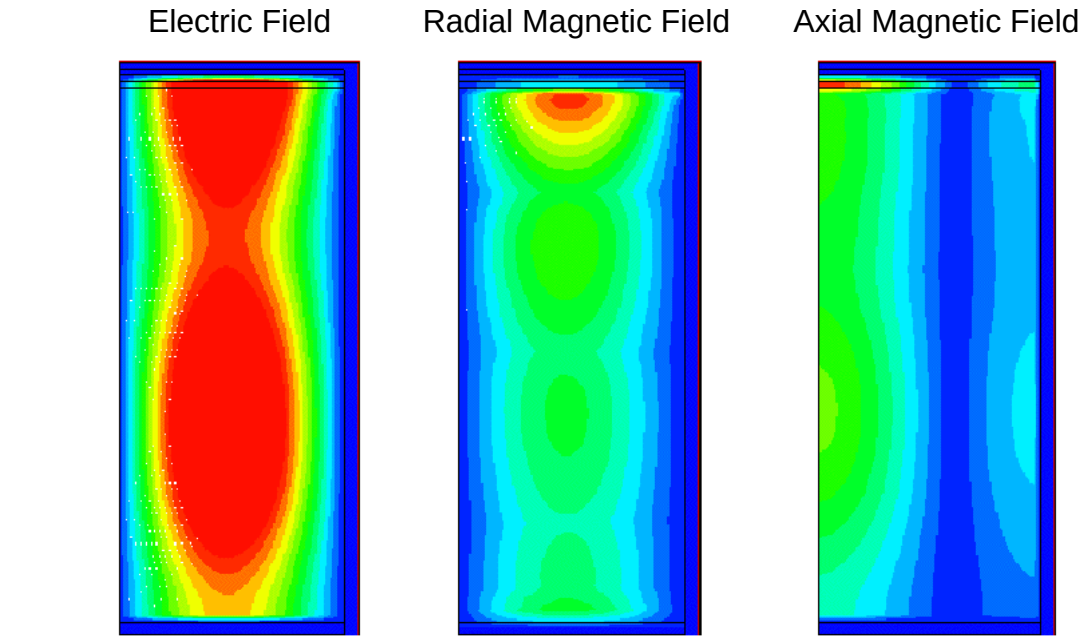

b)

Figure 2.4 Azimuthal electric, radial magnetic, and axial magnetic fields for varying bottom boundary conditions. Results for (a) constant electric field gradient (b) a linearized first order wave equation boundary condition at the bottom of the waveguide are shown.

III. Consequences of Mode Structure, Magnetic Field Configuration, and Operating Conditions on ECR Plasma Parameters

3.1 Simulated Reactor Geometry, Operating Conditions, and Base Case Analysis.

The ECR model simulates a cylindrical reactor shown in Figure 3.1. Gases are injected into the reactor through a ring nozzle located near the microwave window and are exhausted downstream through a pump port. Nitrogen is used as the feedstock gas. Gas pressure was varied from 0.5 – 50 mTorr and flow rates were varied from 5 – 20 sccm resulting in residence times of a few milli-seconds. Typical operating power ranged from 500 – 1500 W. The collisional processes for neutral particles and ions were, (1) ionization, excitation, and momentum transfer collisions between electrons and neutral particles, (2) Coulomb collisions between electrons and ions, (3) charge exchange collisions between ions and neutral particles, and (4) momentum transfer collisions among neutral particles. The full reaction scheme is listed in Table 3.1. Electron impact reactions with molecular nitrogen include excitation up to the eighth vibrational state and the third electronic state of N_2. The vibrational and electronic states used in the model are the sum of all the vibrational and electronic states created by electron impact collisions, respectively.

Excitation of the electron gas occurs through ECR coupling of the incident microwave field in the presence of the magnetic field produced by the coils surrounding the throat region of the chamber. Transverse electric microwave fields, TE(0,n), operating at 2.00 GHz, were used to sustain the plasma. Although in commercial reactors a 2.45 GHz microwave is frequently used, a lower frequency was used in these

simulations to reduce the computation time. For proper computation of wave propagation, a minimum number of grid points are needed. The grid resolution for in the direction of propagation must be at least 80 grid points per wavelength. Resolution in the direction perpendicular to propagation can be coarser, with about 40 grid points per wavelength. The grid dimensions used here were 160 points in the axial direction and 55 points in the radial direction, for a total of 8,800. Applying the previous criterion, the total number of points needed for the same geometry operating at 2.45 GHz is 12,740. By using a frequency of 2.00 GHz, the cpu time is reduced by 33%, while the results obtained at the lower frequency are comparable to those obtained at 2.45 GHz.

i) Plasma Parameters

The base case was N_2 at 1 mTorr, 10 sccm and 750 W. The circularly transverse electric fields are injected at the top of the reactor through a waveguide antenna. The wave propagates through the dielectric window and into the processing chamber. A static magnetic field is generated by a direct current solenoid, designed to produce a resonance zone in the throat of the chamber. Magnetic field lines and contours are shown in Figure 3.2. The top set of magnetic coils are use to determine the location of resonance, while the bottom coil is used to enhance confinement of charged species and allow tailoring of the flux profile to the wafer surface. Base case simulations used only the upper most top coil and the subcoil. For the given geometry and operating conditions, the primary resonance occurs in the upper region of the reactor where B = 714 Gauss. There is also a secondary resonance located downstream that occurs when the subcoil is used. When $\omega_{cyc} = \omega$, the conductivity peaks in a resonant manner and exhibits a Lorentzian line shape, as

shown in the left side of Figure 3.3 (b). The axial profile of the static magnetic field and the conductivity, at a radius of r = 5 cm, are shown in Figure 3.4 (a). The conductivity reaches a peak value of 0.035 Ω^{-1}-cm^{-1} in the resonance zone (z = 19.5 cm) and falls off by a factor of 10^4 in a 2.2 cm axial range, having a full width at half maximum ($\Delta\omega_{ce}$) of twice the collision frequency, $2\nu_m$.

As the electromagnetic wave approaches the resonance zone, the magnitude of the wave falls of by a factor of 10 from its initial value. The axial profile of the incident electric field and power deposition in the chamber at a radius of r = 5 cm are shown in Figure 3.4 (b). At the input window (z = 26 cm) the electric field amplitude is 184.2 V-cm^{-1}, which falls monotonically to 27.8 V-cm^{-1} in the resonance region. At these operating conditions, 85% of the incident wave is absorbed before the middle of the resonance zone. There is a small amount of transmission of the incident electromagnetic wave into the downstream region, as shown in Figure 3.3 (a) and 3.4 (b). The amount of transmission is a sensitive function of gas pressure. When transmission does occur, reflected waves off surfaces in the downstream region (i.e. the wafer) can create interference patterns with the transmitted wave. This combination can produce a small standing wave pattern in the downstream region, as shown in Figure 3.4 (b). The axial magnetic field component of the wave is seen to follow the same as for azimuthal electric field profiles as shown in the right side of Figure 3.3 (a). The magnetic field falls off at a comparable rate to the azimuthal electric field. The enhanced magnetic field at the edge of the wafer is caused by steep gradients in the finite difference approximation.

Power deposition in the reactor is given by Equation 2.4.16 and is shown in the right side of Figure 3.3 (b). The power deposition follows the conductivity along the axial

direction, exhibiting a Lorenztian line shape, while it reflects the profile of the azimuthal electric field component along the radial direction. Power deposition occurs predominantly within 3% of the resonance zone, although a small amount of power deposition occurs near the bottom coil due to the second resonance region created by the subcoil. Peak values of power deposition are 15.2 W-cm^{-3} in the resonance region and fall off by a factor of 10^4 in a 2.6 cm axial distance downstream. In the upstream region, the continual absorption of the incident electromagnetic wave produces a small amount of power deposition that constitutes about 2% of the total.

Electron temperatures in ECR sources are typically higher than those obtained using inductively coupled plasma (ICP) devices.[1] Electron temperatures can exceed 8 eV for pressures below 0.5 mTorr. Electron temperatures in the resonance region reflect radial power deposition distributions, and have a peak value of 7.1 eV, as shown in the left side of Figure 3.5 (a). In the steady state, the plasma generation by ionization of neutrals is in balance with plasma losses due to diffusion. The solenoidal magnetic field minimizes diffusion losses to the chamber walls. Diffusion therefore mainly occurs along the magnetic field lines thereby allowing the radial electron temperature distribution to maintain its profile far into the downstream region.

Due to a large electron mobility along the magnetic field lines, electrons initially quickly transport out of the system, leaving ions behind and building a space charge potential. This condition leads to ambi-polar diffusion of ions and the production of a electropositive plasma. The high electron temperatures tend to produce a large electric potential which has a uniform profile throughout the processing chamber, as shown in the right side of Figure 3.5 (a).

ii) Gas dynamics

The ionization rates and electron densities are shown in Figure 3.6 (a). The ionization rate has a maximum off axis near the peak in the electron temperature. The peak value of the ionization rate in the resonance zone is 1.07×10^{16} cm^{-3}-sec^{-1} and the off axis distribution is maintained downstream. This distribution results from the enhanced transport of hot electrons along the magnetic field lines which allows for ionization to occur downstream. The electron density peaks in the resonance zone with a value of 1.58×10^{11} cm^{-3}. For these operating conditions, the radial distribution of densities tend to reflect their radial sources, due to the strong radial confinement of electrons by the magnetic field which enable the off axis distribution to be maintained downstream. Due to the small amount of power deposition that occurs near the subcoil, there is a local peak in the electron density. It will be shown in Section 3.5 that the electron density is a sensitive function of pressure.

The distribution of $N_2(X\ ^1\Sigma_g^+)$ and its source are shown in Figure 3.6 (b). The depletion of N_2 occurs primarily by electron impact reactions. Therefore the gas density has a minimum in the off axis region were the ion density peaks. However, production of N_2 is dominated by recombination at the walls and is strongest at the dielectric window, were the density of excited species is the highest. The vector arrows shown in Figure 3.8 represent gas flow in the reactor chamber.

The $N_2(X\ ^1\Sigma_g^+, v=1)$ density and its source are shown in Figure 3.7 (a). Depletion of the vibrational state occurs through electron impact reactions which produce the electronic state $N_2(A\ ^3\Sigma_u^+)$. These reactions occur at high electron temperatures since the threshold energy is ~ 6 eV. Therefore, the $N_2(X\ ^1\Sigma_g^+\ v=1)$ production rate is negative and

follows the off axis peak in the ionization. In the volume beyond the radius of the substrate the electron temperature decreases to the point where excitation to the first electronic state is not important, thereby reducing losses enabling the production rate to peak. The density of $N_2(X\ ^1\Sigma_g^+, v=1)$ reflects the off axis sink in the production rate.

The $N_2(A\ ^3\Sigma_u^+)$ density and source are shown in Figure 3.7 (b). The electronic state is primarily produced through electron impact reactions with the ground state, $N_2(X\ ^1\Sigma_g^+)$ and the first vibrational state, $N_2(X\ ^1\Sigma_g^+\ v=1)$. Results suggest that excitation from the ground state to the electronic state is in large part achieved through a vibrational transition. The spatial distribution of excitation of $N_2(A\ ^3\Sigma_u^+)$ production follows that for ionization and is peaked off axis. However, there is also a local peak in the production rate near the dielectric window. This is due to a small peak in the density of the vibrational state that occurs near the window. In this region, electron temperatures are high enough to produce excitation from $N_2(X\ ^1\Sigma_g^+\ v=1)$ to $N_2(A\ ^3\Sigma_u^+)$. Steep gradients in the radial direction suggest that the electronic state is short lived and its density depends largely on local reaction kinetics.

The production of ground state atomic nitrogen, $N(^4S^0)$, occurs dominantly through the dissociation of ground state molecular nitrogen, $N_2(X\ ^1\Sigma_g^+)$. Density and sources for $N(^4S^0)$ are shown in Figure 3.8 (a). Production is peaked off axis and reflects electron densities. Atomic nitrogen densities are uniform throughout the reactor, but exhibit peaks at the walls surface from the quenching of $N(^2D^0)$ and neutralization of $N^+(^3P)$. Density and sources for the $N(^2D^0)$ state are shown in Figure 3.8 (b). The radial gradients of $N(^2D^0)$, suggest that it has a short lifetime and that densities largely depend on local reaction kinetics, similar to $N_2(A\ ^3\Sigma_u^+)$.

Density and ionization rates for charged species $N_2^+(X\ ^2\Sigma_g^+)$ and $N^+(^3P)$ are shown in Figure 3.9. Production of $N_2^+(X\ ^2\Sigma_g^+)$ occurs predominately through an electron impact collision with $N_2(X\ ^1\Sigma_g^+)$, while the production of $N^+(^3P)$ occurs predominately through a charge exchange collision with $N_2^+(X\ ^2\Sigma_g^+)$. Both charged species have production and density peaks off axis. However, $N_2^+(X\ ^2\Sigma_g^+)$ retains its off axis peak further downstream than $N^+(^3P)$ because the diffusion perpendicular to the magnetic field lines is smaller for the heavier $N_2^+(X\ ^2\Sigma_g^+)$ ion than the $N^+(^3P)$ ion.

3.2 Experimental Validation of Ion Saturation Current

To validate predictions of flux to the substrate, experiments conducted at Kyushu University were simulated.[2] The experimental apparatus consisted of a TE_{01} microwave source at 2.45 GHz. The ion saturation current density and the plasma potential were measured by a cylindrical Langmuir probe 1 mm in diameter. The simulation geometry and operating conditions resemble the experiment except that the length of the reactor in the simulations is half of the experiment. The ion saturation current density is given by,

$$I = 2\,e\,n_s\left(\frac{2\,e\left|\Phi_p - V_B\right|}{m}\right)^{\frac{1}{2}} \qquad (3.2.1)$$

where e, n_s, Φ_p, V_B, and m are the electric charge, ion density, plasma potential, probe potential, and ion mass. The radial distribution of the ion saturation current density was compared to the experimental results shown by Hidaka *et al*. The N_2 pressure is 0.5 mTorr with a power deposition of 3 kW. The radial distribution of the ion saturation

current density for both experiment and computation are in good agreement, as shown in Figure 3.10. The radial ion saturation current density in the case of the TE_{01} mode is uniform within 5% over an 8 inch diameter. Since the saturation current was obtained from the plasma potential, such uniformity might have been expected from the uniformity of the plasma potential distribution shown in the right side of Figure 3.5 (a). The dependence of ion saturation current density on input microwave power is shown in Figure 3.11. Theoretical predictions follow experimental trends with the saturation current increasing linearly in proportion to microwave power.

3.3 Activation of Subcoil

Base case simulations were conducted with the magnetic subcoil activated. Results based on parametric studies conducted with and without activation of subcoil are discussed in this section. Magnetic field line configurations without and with activation of the subcoil are shown in Figure 3.12. The bottom coil is used to enhance confinement of charged species. By producing a solenoidal magnetic field configuration, diffusion losses to the walls are significantly reduced. The average reactor electron density as a function of power with and without activation of the subcoil is shown in Figure 3.13. The electron density is higher with the subcoil than without. The electron density did increase with increasing power without the subcoil but the slope is smaller than with the coil. At a power of 500 W, the electron density is increased by 100% when operating with the subcoil as compared to operating without the subcoil. At a power level of 1500 W, the electron density is increased by more than 230%. This apparent saturation of the absorbed power is qualitatively similar to measurements made in other systems using probes[3] and

interferometry.[4] This effect has been attributed to a failure of the microwaves to propagate in an overdense plasma.[5]

The effects of activating the subcoil on electron temperature as a function of power are shown in Figure 3.14. A larger electron temperature is obtained without activation of the subcoil. The decrease in average electron temperature with the subcoil is due to reduced diffusion losses. Ionization efficiency of the neutral gas is also enhanced with the subcoil, as shown in Figure 3.15. The reactor average ion to neutral density ratio follows the same dependence as the electron density. These results suggest that the electron density may not be limited by the apparent saturation of absorbed power, as previously mentioned, but instead may be limited by the diffusion losses.

Another benefit using the subcoil is to allow tailoring of the ion fluxes to the wafer surface. The solenoidal magnetic field configuration causes the plasma density to maintain the radial profile it had in the resonance zone near the substrate surface. The effects of subcoil activation on the ion flux to the substrate are shown in Figure 3.16. The increase in ion flux with increase in power reflects the overall increase in the reactor average plasma density.

Flux uniformity is defined as,

$$\text{Flux uniformity} = 1 - \frac{\left|\Phi_{\text{Peak}} - \Phi_{\text{Average}}\right|}{\Phi_{\text{Average}}}, \qquad (3.3.1)$$

where Φ_{Peak} and Φ_{Average} are the peak and average ion flux, respectively. The ion flux profiles with and without activation of the subcoil are different at of 1 mTorr. Without

activation of the subcoil, the flux profiles have a 83% uniformity at 1,000 W and a 95% uniformity at 500 W. This trend is due to the tieing of flux to magnetic field lines, which cause enhanced radial divergence and a subsequent loss of the plasma to the walls. With the subcoil, ion flux profiles tend to reflect the off axis plasma density peaks shown in Figure 3.16. The ion flux profiles become increasingly non-uniform at higher power levels. At 500 W, flux profiles have a 86% uniformity, while at 1,000 W uniformity falls to 69%. Flux profiles for neutral species incident on the substrate show similar results. Fluxes for $N_2(X\ ^1\Sigma_g^+, v=1)$, $N_2(A\ ^3\Sigma_u^+)$, $N(^4S^0)$, and $N(^2D^0)$ reflect their off axis density peaks, as shown in Figures 3.17 - 3.20.

Ion fluxes at higher pressures (> 1 mTorr) show a significant decrease. In the limit where the cyclotron frequency is much larger than the collision frequency, diffusion perpendicular to the magnetic field lines increase with the rate of collisions at higher pressures while the mobility and diffusion coefficient parallel to the magnetic field is inversely proportional to the collision frequency. Axial diffusion losses decrease along the axial direction at higher pressures, while there is an increase in cross field diffusion.

The second reason is due to the decrease in axial diffusion losses. As diffusion parallel to the field lines is decreased at higher pressures, the residence times are lengthened, thereby increasing the probability for cross field diffusion to occur. These coupled effects tend to produce a more uniform plasma density profile in the downstream region, as shown by the ion flux profiles at the substrate in Figure 3.21. At 1 mTorr, the ion flux profile is affected by the activation of the subcoil. At these operating conditions the plasma density is peaked off axis in the resonance zone. Due to the activation of the subcoil, the off axis peak is shifted downstream and is reflected in the flux profile.

As the pressure is increased, with the subcoil on, the magnitude of the flux decreases. However, the uniformity of the flux profile is improved because the plasma density profile has become more uniform in the downstream region. Flux magnitudes for $N_2(X\ ^1\Sigma_g^+, v=1)$ and $N(^2D^0)$ increase with increasing pressure, as shown in Figure 3.22 and 3.23. Subcoil activation tends to increase the fluxes because of an increased in the rate of electron impact processes. The uniformity of the flux of these longed lived neutrals do not have a strong dependence on subcoil activation, but instead are sensitive to increased pressure gradients at the substrate surface that are at higher pressures. However, the uniformity of the flux for $N_2(A\ ^3\Sigma_u^+)$, shown in Figure 3.24, is strongly dependent on subcoil activation implying that the flux is sensitive to chemical kinetics close to the substrate. The flux for ground state atomic nitrogen, shown in Figure 3.25 had little dependence on subcoil activation, at higher pressures, and had uniformity above 95%.

Overall, these results suggest that use of the subcoil causes the flux to the substrate to more closely reflect the reactor density profiles. An increase in power leads to the enhancement of any non-uniformities present in the flux profile. At higher pressures the sensitivity on subcoil activation is decreased and the uniformity of the flux is improved.

3.4 Results for Varying Modal Structures

Higher order circular TE_{on} modes have several off axis peaks in the electric field depending on the harmonic used. The use of higher order modes is believed to create several off axis power deposition peaks and thereby provide greater uniformity at the

substrate. Incident electromagnetic wave profiles for TE_{02} mode fields are shown in Figure 3.26 (a). The azimuthal electric field component of the incident wave has an off axis node that produces two peaks in the field intensity. The magnitude of the outer peak is smaller than the inner peak as per the derivative of the Bessel function (Eq. 2.4.18a). The power deposition profile, shown in Figure 3.26 (b), reflects the field intensity of azimuthal electric field component. When using the TE(0,2) mode, the off axis zero produces two separate regions of power deposition. However, the power deposited in the outer peak is less than that deposited in the inner peak by a factor of two. The power deposition profile follows the conductivity profile along the axial direction and exhibits a Lorenztian line shape similar to the TE_{01} mode.

Enhanced diffusion along the magnetic field lines allows the radial electron temperature distribution to maintain its profile far into the downstream region as shown in Figure 3.26 (b). Similar to the TE_{01} modes, higher order modes have enhanced thermal conductivity along the magnetic field lines. However for the higher modes, the radial electron temperature does not directly reflect the radial power deposition profiles. The radial profiles for the power deposition and electron temperature in the resonance zone for TE_{01} and TE_{02} modes, are shown in Figure 3.27. In the TE_{01} case, the electron temperature reflects the off axis peak in the power deposition. While in for the TE_{02} mode field, the radial electron temperature profile exhibits only one off axis peak produced by the inner power deposition peak. The superposition from both peaks causes the temperature distribution to be constant as a function of radius outside of the first node in the power deposition radial profile. The central peak in the radial temperature for the

TE_{02} case produces ionization rate distributions that are peaked closer to the axis of symmetry than those produced for the TE_{01} case, as shown in Figure 3.28.

The electron temperatures as a function of power for the TE_{01} and TE_{02} modes are shown Figure 3.29. In the resonance zone, electron temperatures tend to be higher for higher electric field modes. For the TE_{02} mode, the superposition of two power deposition peaks produces higher temperature distributions than those produced by the TE_{01} mode. Likewise in the resonance zone, electron densities tend to be higher for the higher modes. Since the electron temperature is higher in this region, local ionization rates will tend to be higher for the higher order modes, producing an increase in the local value of the electron density. However, reactor averaged electron production rates are higher for the lower modes because of lower diffusion losses that occur at the lower temperature. This produces a higher reactor average plasma density for the TE_{01} mode than the TE_{02} mode, as shown in Figure 3.30. In addition, the reactor average electron temperature, shown in Figure 3.29 is lower for the TE_{01} mode. Such a decrease in the reactor average electron temperature for the lower TE_{01} mode is due to reduced diffusion losses and the cooling of the electron gas due to elastic collisions that occurs at the higher densities. Subsequently, the ion to neutral density ratio is higher for the lower mode structure. As shown in Figure 3.31, the TE_{01} mode structure is more efficient in the overall ionization of the gas.

Ion flux profiles tend to reflect the off axis peaks in ionization rates and plasma densities. The ion flux shows the effect of the inner peak in the power deposition for the TE_{02} mode, as shown in Figure 3.32. The peak values for the higher order modes are higher than those produced by the lower mode fields. However, since the position of the

higher TE_{02} peak is at a smaller radius (r = 1.8 cm) than the peak value of the lower TE_{01} peak (r = 3.9 cm), the overall average ion flux to the substrate is higher for the lower mode, as shown in Figure 3.33. Fluxes profiles for all neutral species show similar trends by reflecting the off axis peak in the power deposition. The peak flux values are not significantly increased by the higher mode fields, as shown in Figures 3.34 - 3.37.

3.5 Pressure Dependence

Plasma parameters are a sensitive function of chamber pressure. Electron temperature dependence on gas pressure is shown in Figure 3.38. The average electron temperature increases slowly at higher pressures, from 1 eV at 50 mTorr to 3 eV at 2 mTorr, and increases at a faster rate below 2 mTorr, reaching a value of ~ 8 eV at 0.5 mTorr. This increase in electron temperature is due to the plasma's ability to efficiently absorb microwave energy, a decrease in collisional cooling that occur in the low pressure regime and larger diffusion losses which require a higher ionization rate to compensate.

Parametric studies show that as the pressure is decreased below 2 mTorr, there is a shift in the peak electron density towards the center of the reactor as shown in Figure 3.39. At 10 mTorr the plasma is peaked at the location of peak power deposition and becomes increasingly uniform toward the substrate surface. At 1 mTorr, the plasma density is peaked again near the location of peak power deposition, but is slightly shifted inward due to diffusion effects. The density maintains its off axis peak far into the downstream region. At 0.5 mTorr, the density has shifted and is now peaked towards the center of the chamber. For these operating conditions, the reactor average electron density peaks around 1 mTorr at a value of 1.25×10^{11} cm^{-3}, as shown in Figure 3.40. As

the pressure is decreased, the average plasma density falls to a value of 5.0×10^{10} cm^{-3} at 0.5 mTorr. As the pressure is increased above 1 mTorr the average plasma density falls off, but at a more gradual rate, to a value of 8.0×10^{10} cm^{-3} at 50 mTorr.

The ion flux to the substrate, shown in Figure 3.41, reflects the shift towards the center at pressures below ~ 1 mTorr. The average ion flux and uniformity are shown in Figure 3.42. At 10 mTorr, the ion flux peaks near a radius of 5 cm at a value of 8.5×10^{15} cm^{-2}-s^{-1}, with a uniformity of 78%. As the pressure decreases below 1 mTorr the peak in the ion flux density shifts towards the center of the reactor and the peak in ion flux increases to 5.0×10^{16} cm^{-2}-s^{-1} at 0.75 mTorr. However, the uniformity falls to 45%. At 0.5 mTorr the ion flux profile peaks at the center with peak value of 2.75×10^{15} cm^{-2}-s^{-1}, while the uniformity begins to increase to a value of 60%. The average ion flux peaks at a pressure of 0.75 mTorr, while uniformity reaches its lowest. These results indicate that there exists an optimal pressure were both average ion flux and uniformity can be efficiently maximized. This efficiency is shown in Figure 3.43 as the product of the average ion flux magnitude and the percent uniformity. The efficiency peaks at a value of 72% for a pressure of 0.75 mTorr.

The decrease in ion flux and increase in flux uniformity is expected in the high pressure regime. The diffusion coefficient parallel to the magnetic field lines decreases with increasing collision frequency. Therefore, in the high pressure regime, the magnitude of the average ion flux has an inverse pressure dependence. Likewise, the increase in the ion flux uniformity is due to the enhancement in the diffusion of charged particles perpendicular to the magnetic field lines. The diffusion coefficient perpendicular to the magnetic field lines goes as, in the limit $\omega_c^2\tau^2 >> 1$,

$$D_{\perp} = \frac{KT\,\nu_m}{m\omega_c^{\,2}}. \qquad (3.5.1)$$

In the low pressure regime, the average ion flux magnitude decreases with decreasing pressure, while the peak-average percent uniformity increases. More significantly, the peak in the plasma density profile shifts toward the center of the reactor suggesting enhanced diffusion perpendicular the magnetic field lines. Such a result is counter-intuitive, since diffusion across the magnetic field lines decreases with decreasing collision frequency. At lower pressures, the collision frequency is expected to decrease accordingly. This increase in collision frequency at lower pressures can be attributed to an increase in the electron temperature. The momentum transfer rate coefficient increases with increasing electron temperature, as shown in Figure 3.44. The momentum transfer rate coefficient and the neutral gas density versus chamber pressure is shown in Figure 3.45. At low pressures, rate coefficient is exponentially increasing due to the rise in the electron temperature. As the pressure increases, the temperature decreases thereby decreasing the value of the rate coefficient. Likewise, as the pressure increases so does the neutral gas density. The collision frequency, which is the product of the momentum transfer rate coefficient and the neutral gas density, is sensitive to temperature in the low pressure regime, while it becomes dependent to neutral gas densities in the high pressure regime. This increase of the collision frequency in the low pressure regime produces enhancement diffusion of charged particles across the magnetic field lines. Overall, diffusion losses are enhanced in both the low and high pressure regimes. There exists an optimal pressure for charged particle confinement, maximizing ion flux to the substrate surface, and flux profile uniformity.

3.6 References

1. S. Rauf and M. J. Kushner, *J. Appl. Phys.*, vol. 81, p. 5966, 1997.
2. R.Hidaka, T. Yamaguchi, N. Hirotsu, T. Ohshima, R. Koga, M. Tanaka, and Y. Kawai, *Jpn. J. Appl. Phys.*, vol. 32, p. 174, 1993.
3. C. A. Outten, J. C. Barbour, and W. R. Wampler, *J. Vac. Sci. Technol. A*, vol. 9, p. 717, 1991.
4. J. E. Stevens, J. L. Cecchi, Y. C. Huang, and R. L. Jarecki, Jr., *J. Vac. Sci. Technol. A*, vol. 9, p. 696, 1991.
5. M. D. Bowden, T. Okamoto, F. Kimura, H.Muta, K. Uchino, and K. Muraoka, *J. Appl. Phys.*, vol. 73, p. 2732, 1993.
6. D. C. Cartwright, S. Trajmar, A. Chutjian, and W. Williams, *Physc. Rev. A*, vol. 16, p. 1041, 1977
7. R. T. Brinkman and S. Trajmar, *Ann. Geophysc.* vol. 26, p. 201, 1970
8. W. L. Borst, *Physc.Rev. A*, vol. 5, p. 648, 1972
9. S. Geltman, *J. Quant. Spect. Rad. Transfer*, vol. 13, p. 601, 1973

Table 3.1 Gas phase reactions for N_2.

Reaction	Rate Coefficient	Ref.
$e + N_2(X\ ^1\Sigma_g^+) \rightarrow e + N_2(X\ ^1\Sigma_g^+, v=1)$	b	6
$e + N_2(X\ ^1\Sigma_g^+) \rightarrow e + N_2(X\ ^1\Sigma_g^+, v=2)$	b	6
$e + N_2(X\ ^1\Sigma_g^+) \rightarrow e + N_2(X\ ^1\Sigma_g^+, v=3)$	b	6
$e + N_2(X\ ^1\Sigma_g^+) \rightarrow e + N_2(X\ ^1\Sigma_g^+, v=4)$	b	6
$e + N_2(X\ ^1\Sigma_g^+) \rightarrow e + N_2(X\ ^1\Sigma_g^+, v=5)$	b	6
$e + N_2(X\ ^1\Sigma_g^+) \rightarrow e + N_2(X\ ^1\Sigma_g^+, v=6$	b	6
$e + N_2(X\ ^1\Sigma_g^+) \rightarrow e + N_2(X\ ^1\Sigma_g^+, v=7)$	b	6
$e + N_2(X\ ^1\Sigma_g^+) \rightarrow e + N_2(X\ ^1\Sigma_g^+, v=8)$	b	6
$e + N_2(X\ ^1\Sigma_g^+) \rightarrow e + N_2(A\ ^3\Sigma_u^+)$	b	7
$e + N_2(X\ ^1\Sigma_g^+) \rightarrow e + N_2(B\ ^3\Pi_g)$	b	7
$e + N_2(X\ ^1\Sigma_g^+) \rightarrow e + N_2(B^1\ ^3\Sigma_u^-)$	b	8
$e + N_2(X\ ^1\Sigma_g^+) \rightarrow e + N_2(a^1\ ^3\Sigma_u^-)$	b	8
$e + N_2(X\ ^1\Sigma_g^+) \rightarrow e + N_2(C\ ^3\Pi_u)$	b	8
$e + N_2(X\ ^1\Sigma_g^+) \rightarrow e + N(^4S^0) + N(^2D^0)$	b	6
$e + N_2(X\ ^1\Sigma_g^+) \rightarrow 2e + N_2^+(X\ ^2\Sigma_g^+)$	b	6
$e + N_2(X\ ^1\Sigma_g^+, v=1) \rightarrow e + N_2(X\ ^1\Sigma_g^+)$	b	6
$e + N_2(X\ ^1\Sigma_g^+, v=1) \rightarrow e + N_2(A\ ^3\Sigma_u^+)$	b	6
$e + N_2(X\ ^1\Sigma_g^+, v=1) \rightarrow 2e + N_2^+(X\ ^2\Sigma_g^+)$	b	6
$e + N_2(A\ ^3\Sigma_u^+) \rightarrow e + N_2(X\ ^1\Sigma_g^+, v=1)$	b	6
$e + N_2(A\ ^3\Sigma_u^+) \rightarrow e + N_2(X\ ^1\Sigma_g^+)$	b	6
$e + N_2(A\ ^3\Sigma_u^+) \rightarrow 2e + N_2^+(X\ ^2\Sigma_g^+)$	b	6
$e + N_2^+(X\ ^2\Sigma_g^+) \rightarrow N(^2D^0) + N(^4S^0)$	1.00×10^{-7}	c
$e + N(^4S^0) \rightarrow e + N(^2D^0)$	b	9
$e + N(^4S^0) \rightarrow e + N(^2P^0)$	b	9
$e + N(^4S^0) \rightarrow 2e + N^+(^3P)$	b	9

$e + N(^2D^0) \rightarrow e + N(^4S^0)$	b	9
$e + N(^2D^0) \rightarrow e + N^+(^3P)$	b	9
$N_2(A\ ^3\Sigma_u^+) + N_2(X\ ^1\Sigma_g^+) \rightarrow 2N_2(X\ ^1\Sigma_g^+)$	1.90×10^{-13}	c
$N_2(A\ ^3\Sigma_u^+) + N(^4S^0) \rightarrow N_2(X\ ^1\Sigma_g^+) + N(^4S^0)$	1.00×10^{-13}	c
$N_2(A\ ^3\Sigma_u^+) + N(^2D^0) \rightarrow N_2(X\ ^1\Sigma_g^+) + N(^4S^0)$	1.00×10^{-13}	c
$N(^2D^0) + N_2(X\ ^1\Sigma_g^+) \rightarrow N(^4S^0) + N_2(X\ ^1\Sigma_g^+)$	2.00×10^{-14}	c
$N(^2D^0) + N(^4S^0) + M \rightarrow N_2(A\ ^3\Sigma_u^+) + M$	2.00×10^{-32}	c
$2N(^4S^0) + M \rightarrow N_2(A\ ^3\Sigma_u^+) + M$	1.00×10^{-32}	c
$2N(^4S^0) + M \rightarrow N_2(X\ ^1\Sigma_g^+) + M$	1.00×10^{-32}	c
$2N_2(A\ ^3\Sigma_u^+) \rightarrow N_2(A\ ^3\Sigma_u^+) + N_2(X\ ^1\Sigma_g^+)$	1.36×10^{-9}	c
$N_2(X\ ^1\Sigma_g^+, v=1) + N_2(X\ ^1\Sigma_g^+) \rightarrow 2N_2(X\ ^1\Sigma_g^+)$	1.00×10^{-13}	c
$N_2(X\ ^1\Sigma_g^+, v=1) + N(^4S^0) \rightarrow N_2(X\ ^1\Sigma_g^+) + N(^4S^0)$	1.00×10^{-14}	c
$N_2(X\ ^1\Sigma_g^+, v=1) + N(^2D^0) \rightarrow N_2(X\ ^1\Sigma_g^+) + N(^4S^0)$	1.00×10^{-14}	c
$N_2^+(X\ ^2\Sigma_g^+) + N(^4S^0) \rightarrow N_2(X\ ^1\Sigma_g^+) + N^+(^3P)$	5.00×10^{-12}	c
$N_2^+(X\ ^2\Sigma_g^+) + N(^2D^0) \rightarrow N_2(X\ ^1\Sigma_g^+) + N^+(^3P)$	1.00×10^{-10}	c
$N_2^+(X\ ^2\Sigma_g^+) + N_2(X\ ^1\Sigma_g^+) \rightarrow N_2(X\ ^1\Sigma_g^+) + N_2^+(X\ ^2\Sigma_g^+)$	1.00×10^{-9}	c
$N_2^+(X\ ^2\Sigma_g^+) + N_2(A\ ^3\Sigma_u^+) \rightarrow N_2(X\ ^1\Sigma_g^+) + N_2^+(X\ ^2\Sigma_g^+)$	1.00×10^{-9}	c
$N_2^+(X\ ^2\Sigma_g^+) + N_2(X\ ^1\Sigma_g^+, v=1) \rightarrow N_2(X\ ^1\Sigma_g^+) + N_2^+(X\ ^2\Sigma_g^+)$	1.00×10^{-9}	c
$N^+(^3P) + N(^4S^0) \rightarrow N(^4S^0) + N^+(^3P)$	1.00×10^{-9}	c
$N^+(^3P) + N(^2D^0) \rightarrow N(^4S^0) + N^+(^3P)$	1.00×10^{-9}	c
$N^+(^3P) + N_2(X\ ^1\Sigma_g^+) \rightarrow N(^4S^0) + N_2^+(X\ ^2\Sigma_g^+)$	1.00×10^{-9}	c
$N^+(^3P) + N_2(A\ ^3\Sigma_u^+) \rightarrow N_2^+(X\ ^2\Sigma_g^+) + N(^4S^0)$	1.00×10^{-9}	c
$N^+(^3P) + N_2(X\ ^1\Sigma_g^+, v=1) \rightarrow N_2^+(X\ ^2\Sigma_g^+) + N(^4S^0)$	1.00×10^{-9}	c

[a] In the FKS, all vibrational excitations of $N_2(X\ ^1\Sigma_g^+)$ are lumped into, $N_2(v)$, which is effectively $N_2(X\ ^1\Sigma_g^+\ v=1)$ and all electronic excitations of $N_2(X\ ^1\Sigma_g^+)$ are lumped into N_2^*, which is effectively $N_2(A\ ^3\Sigma_u^+)$.
[b] Rate coefficients are calculated from electron energy distribution obtained from EETM.
[c] Estimated.

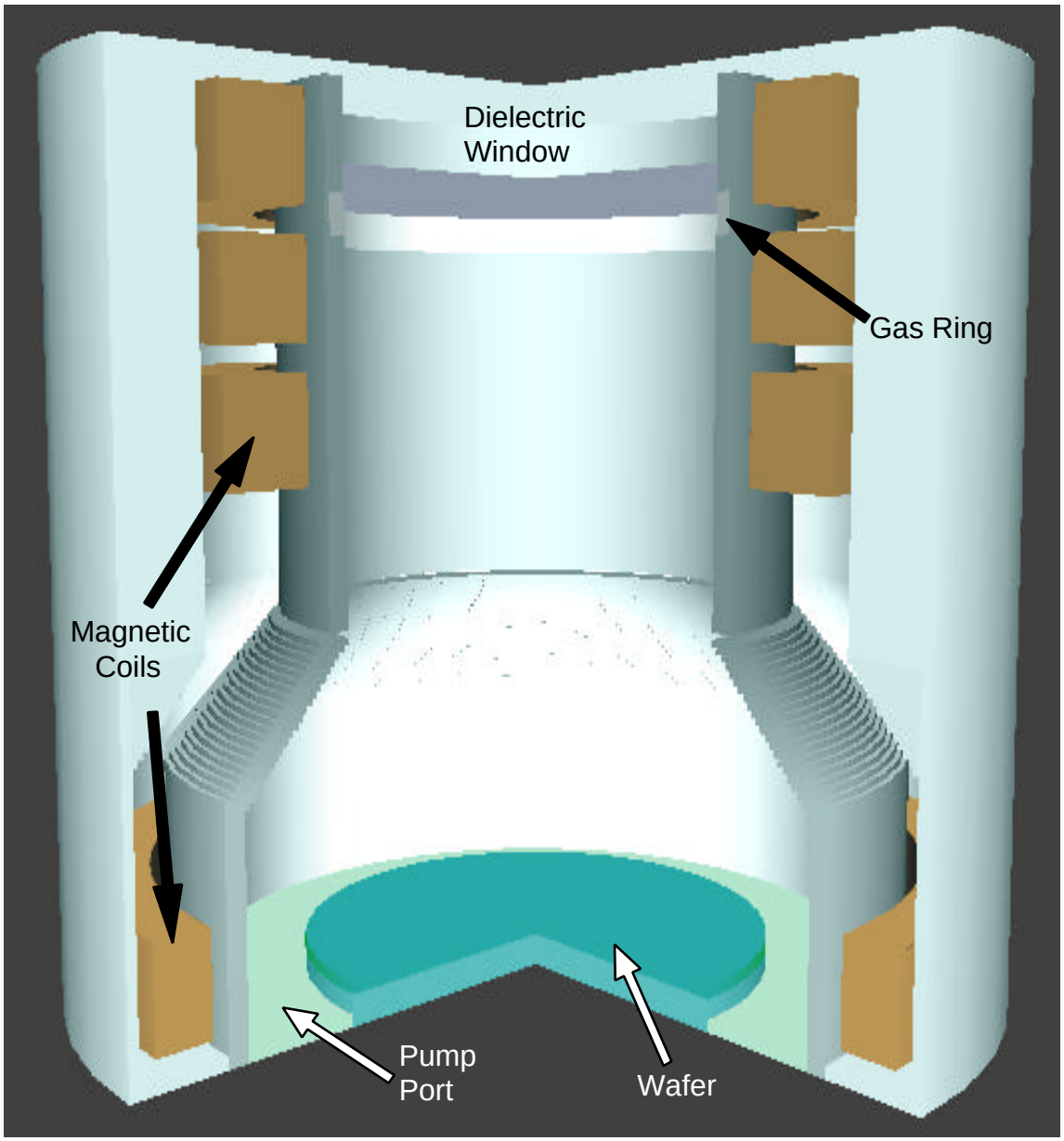

Figure 3.1 Typical electron cyclotron resonance (ECR) tool used for materials processing.

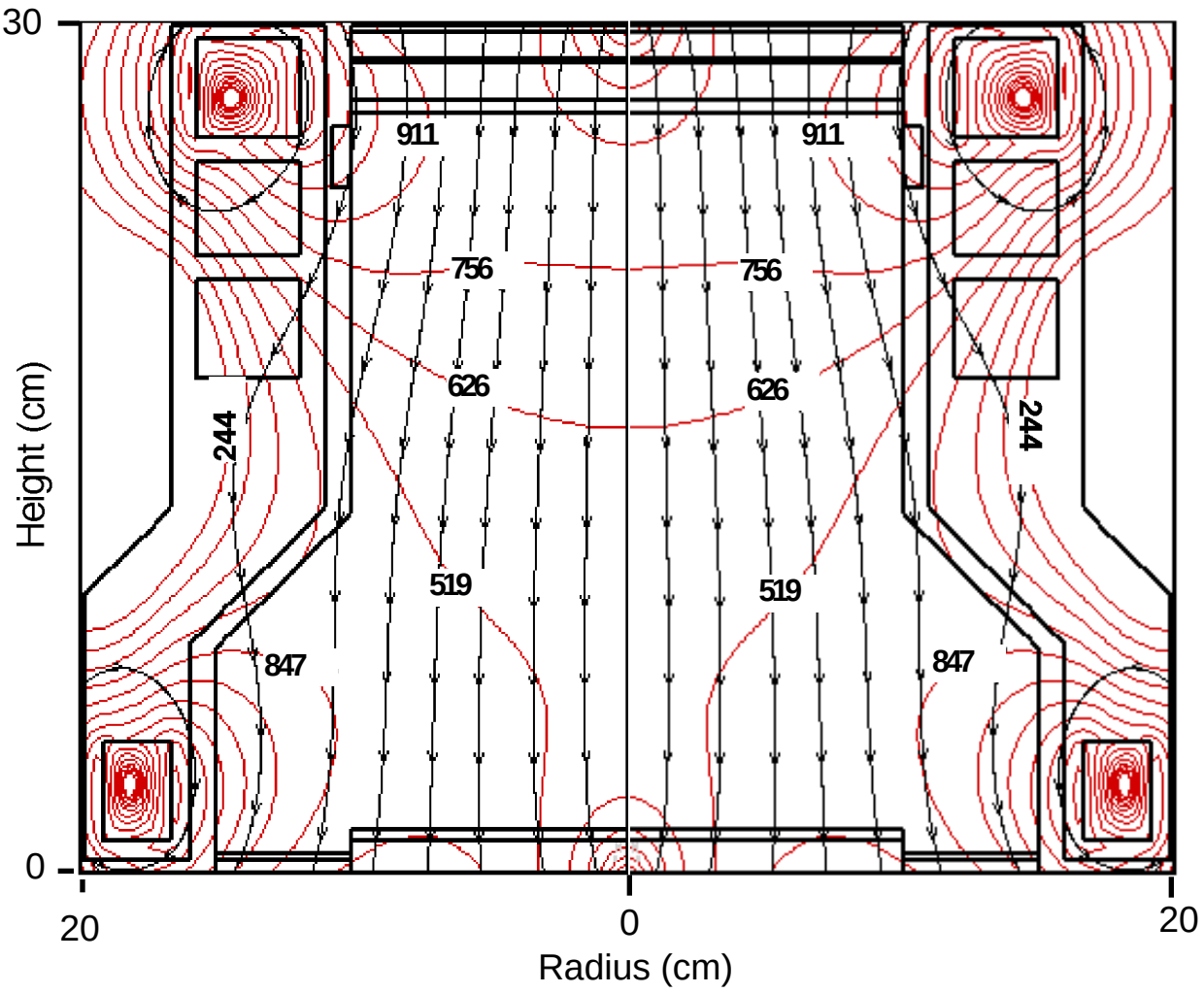

Figure 3.2 Magnetic field configuration inside the ECR reactor. Vector arrows (black) represent magnetic flux lines and contour lines (red) represent magnetic field intensities.

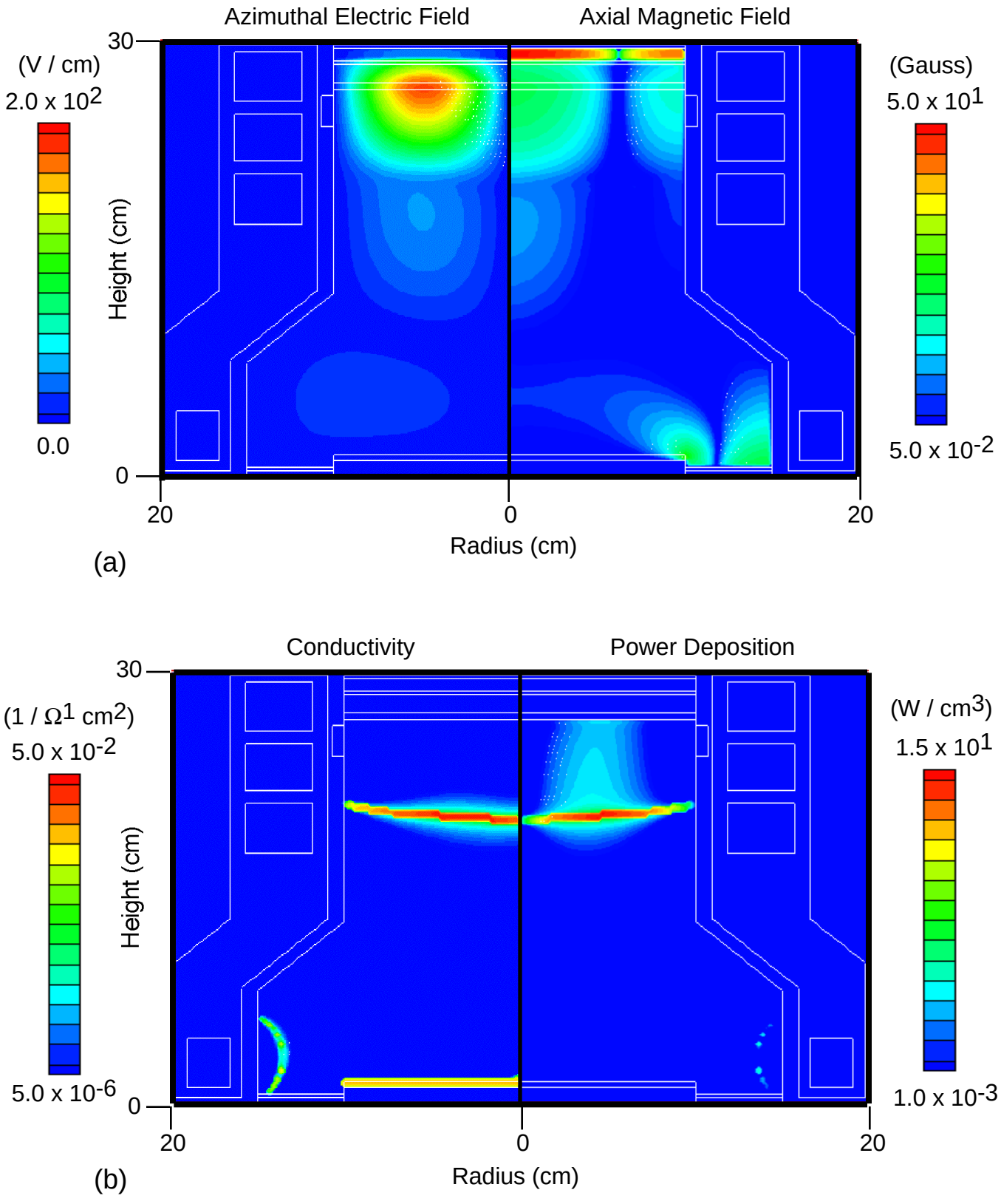

Figure 3.3 Azimuthal electric field component and axial magnetic field component of the incident electromagnetic field (b) plasma conductivity and power deposition inside the ECR processing tool for base case conditions.

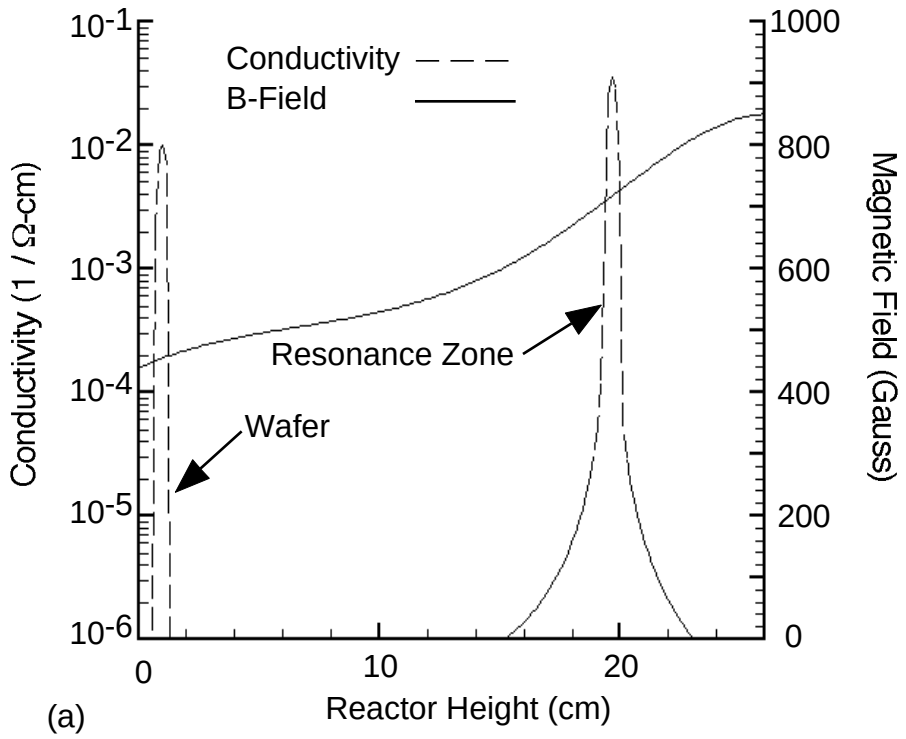

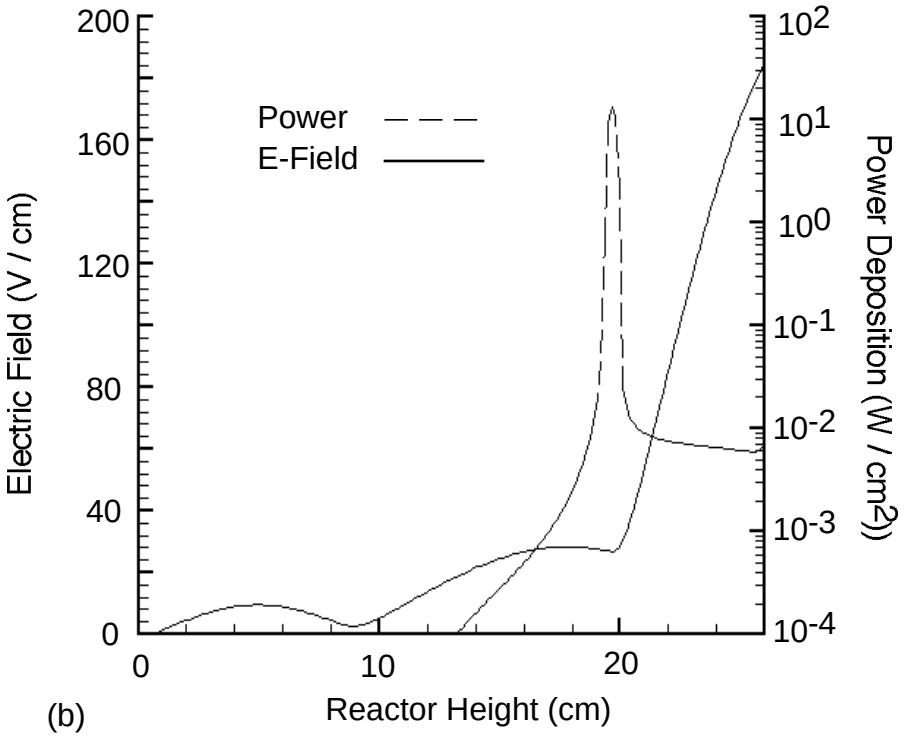

Figure 3.4 Axial profiles of (a) plasma conductivity and static magnetic field (b) azimuthal electric field intensity and power deposition for base case conditions at a radius of 5 cm.

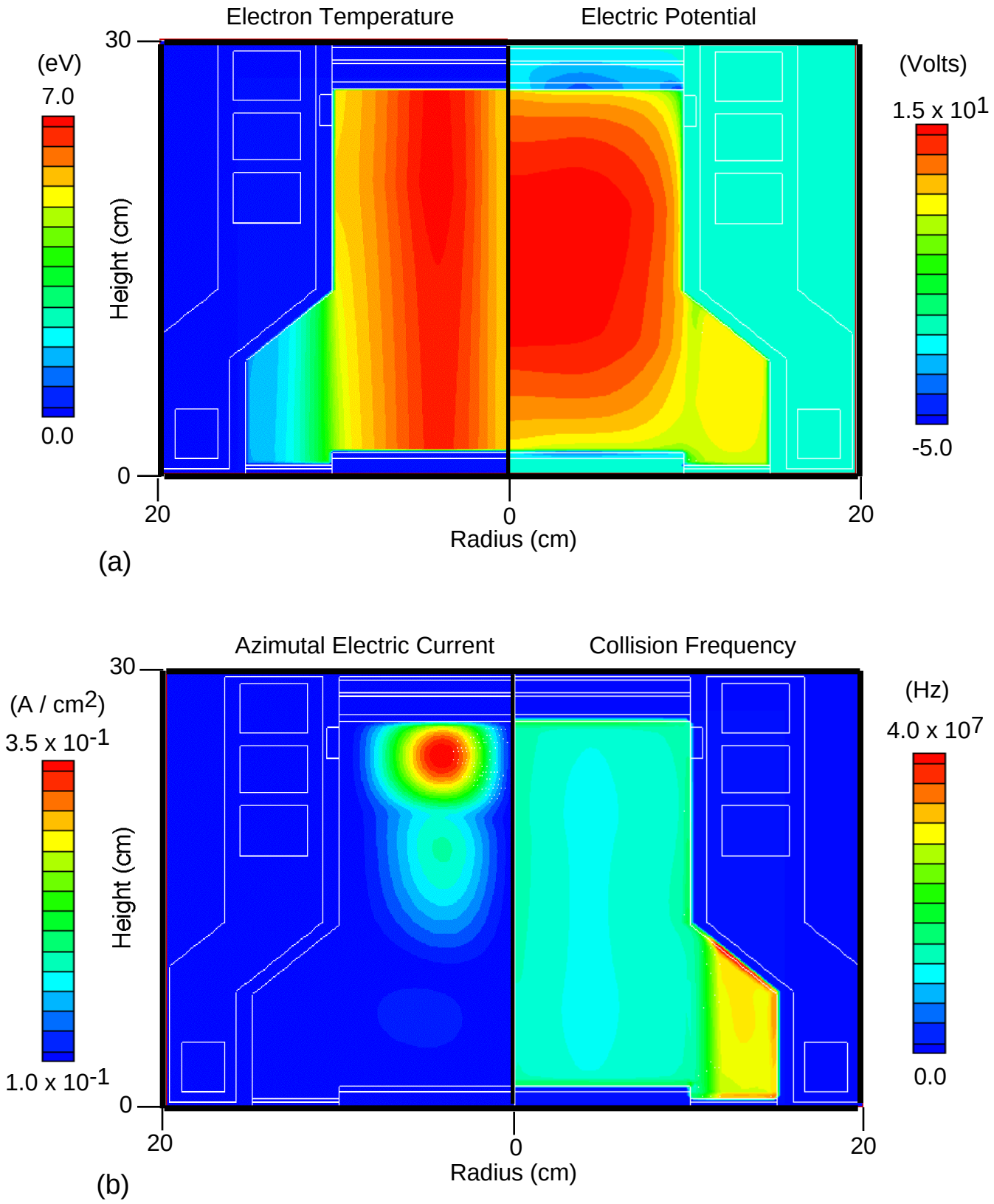

Figure 3.5 (a) Electron temperature and electric potential (b) azimuthal electric current and momentum transfer collision frequency inside the ECR processing tool for base case conditions.

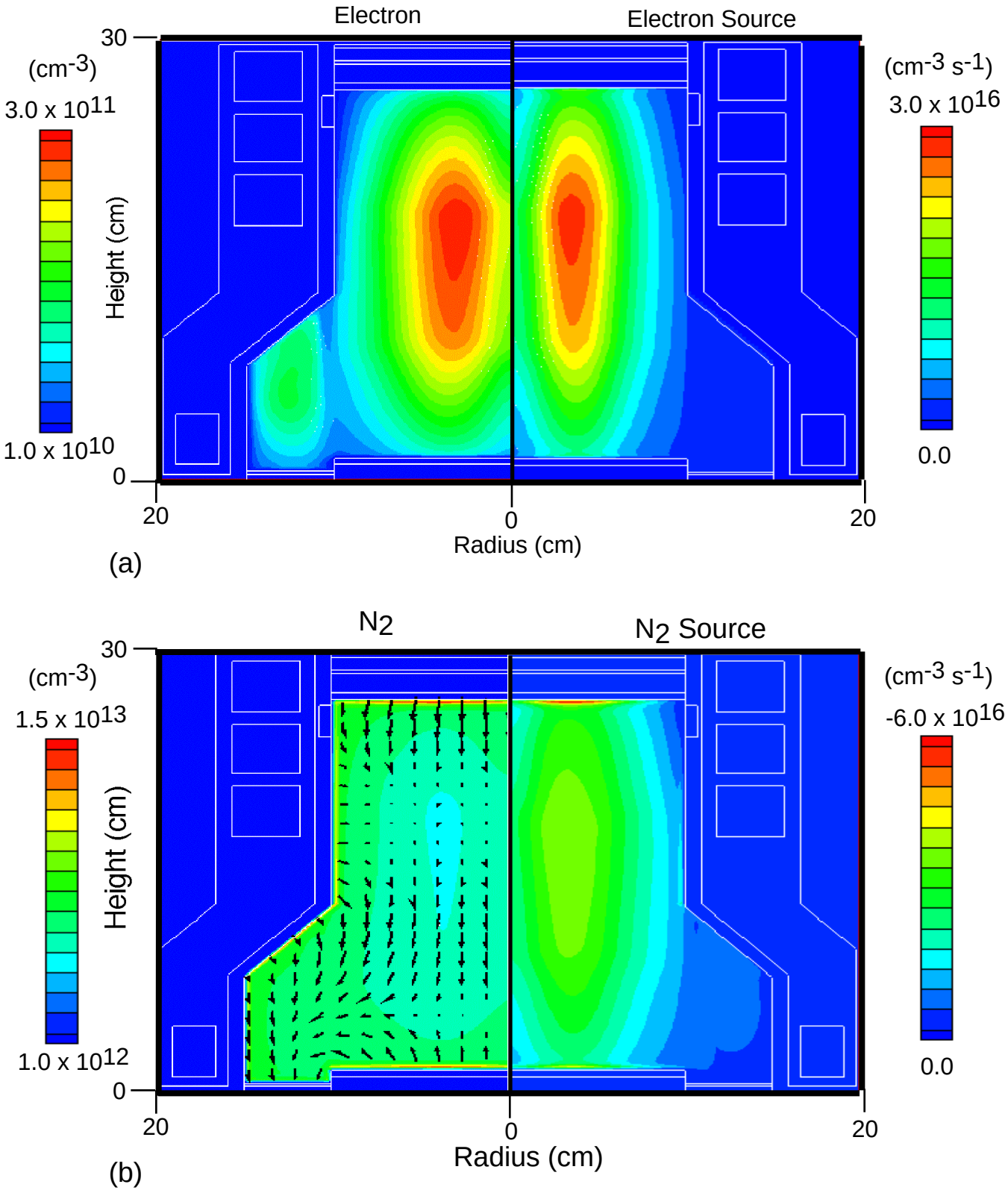

Figure 3.6 (a) Electron density and electron source (ionization rate) (b) N_2 gas density and N_2 source inside the ECR processing tool for base case conditions. Black vector lines in (b) represent gas flow.

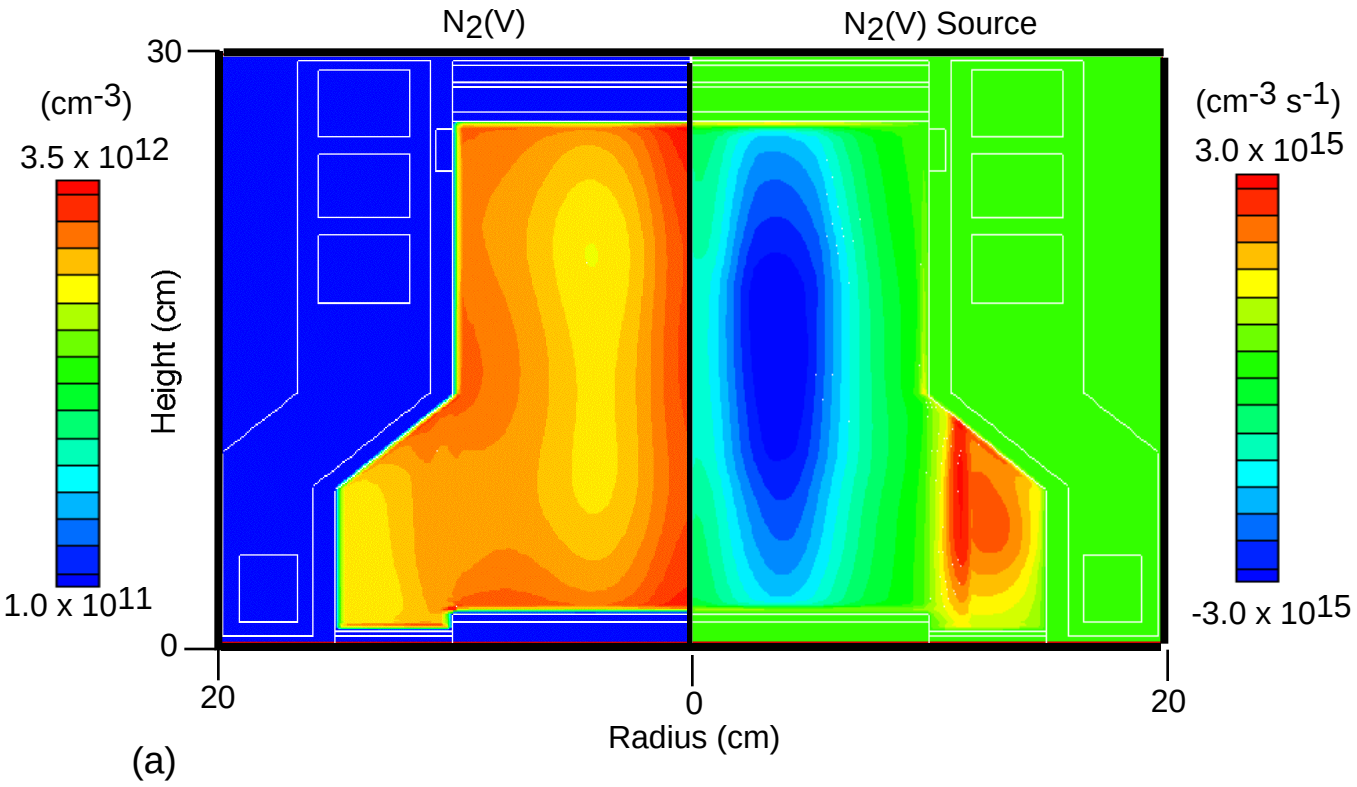

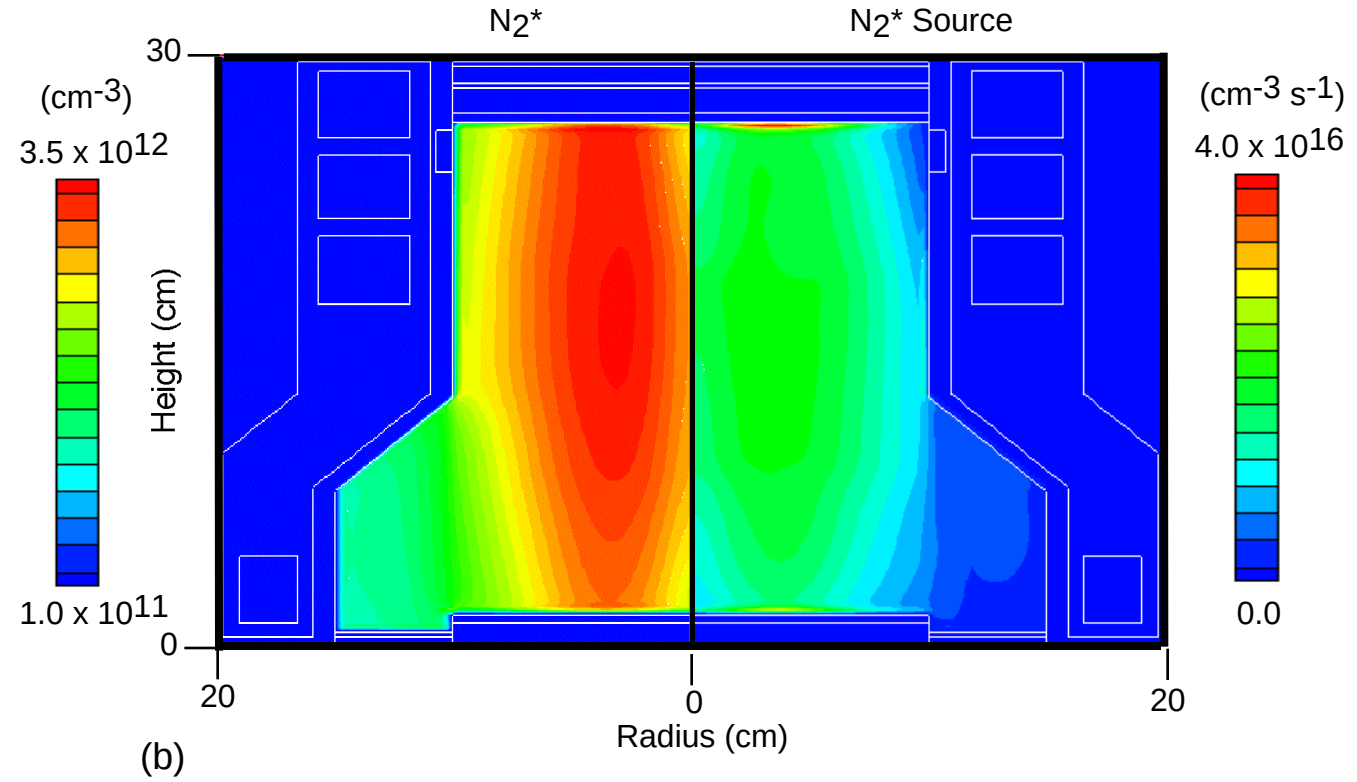

Figure 3.7 (a) N_2(v) density and N_2(v) source (b) N_2* density and N_2* source inside the ECR processing tool for base case conditions.

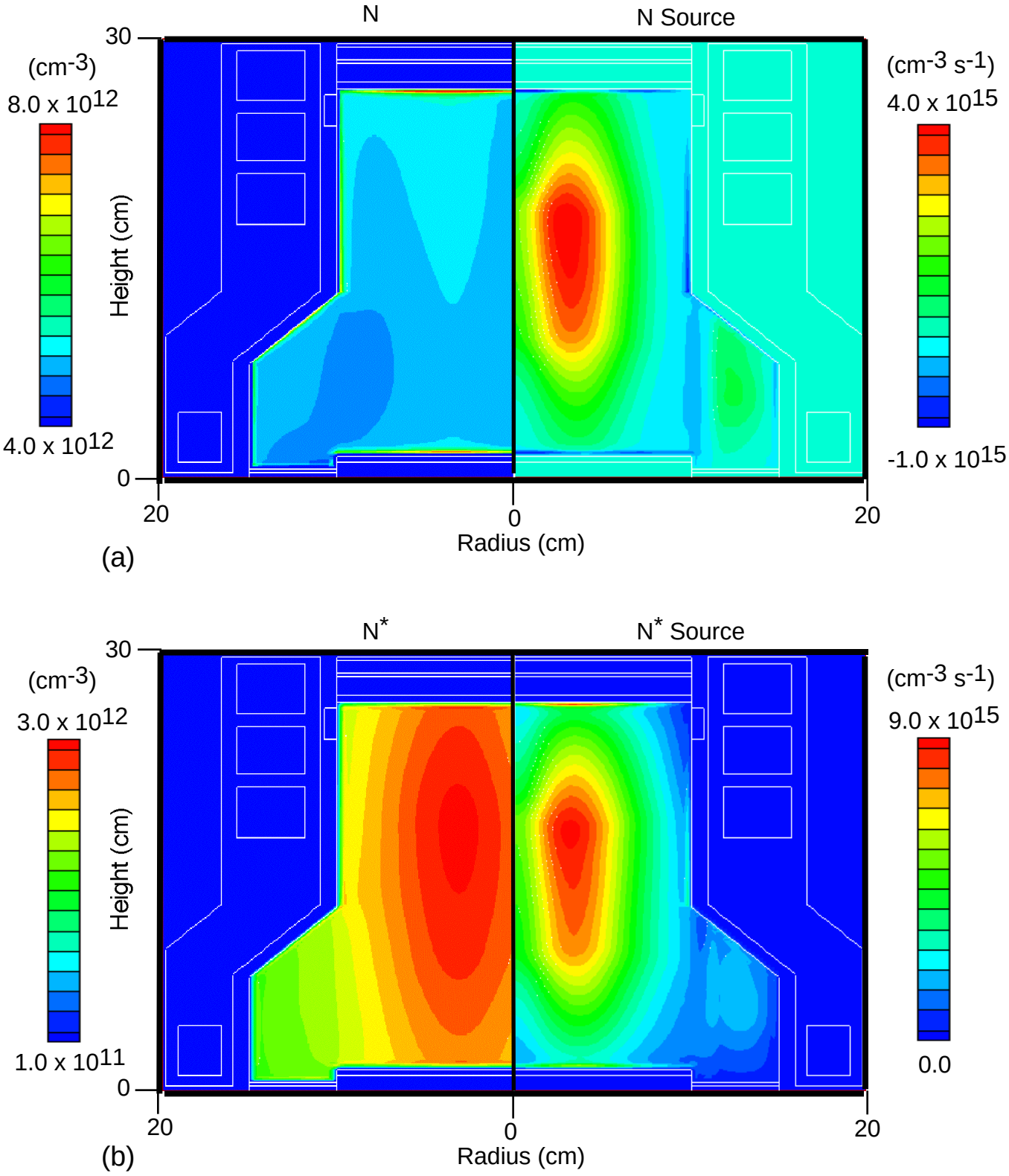

Figure 3.8 (a) N density and N source (b) N* gas density and N* source inside the ECR processing tool for base case conditions.

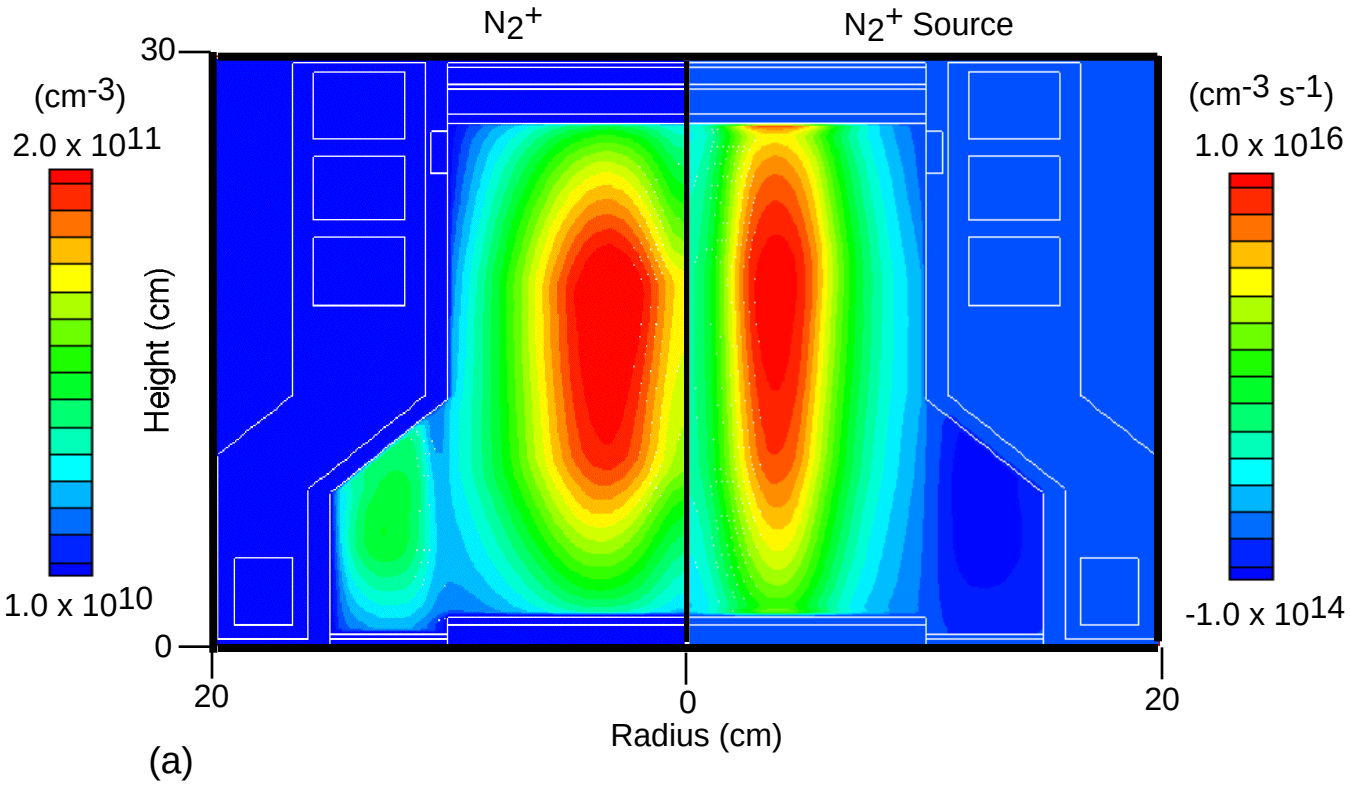

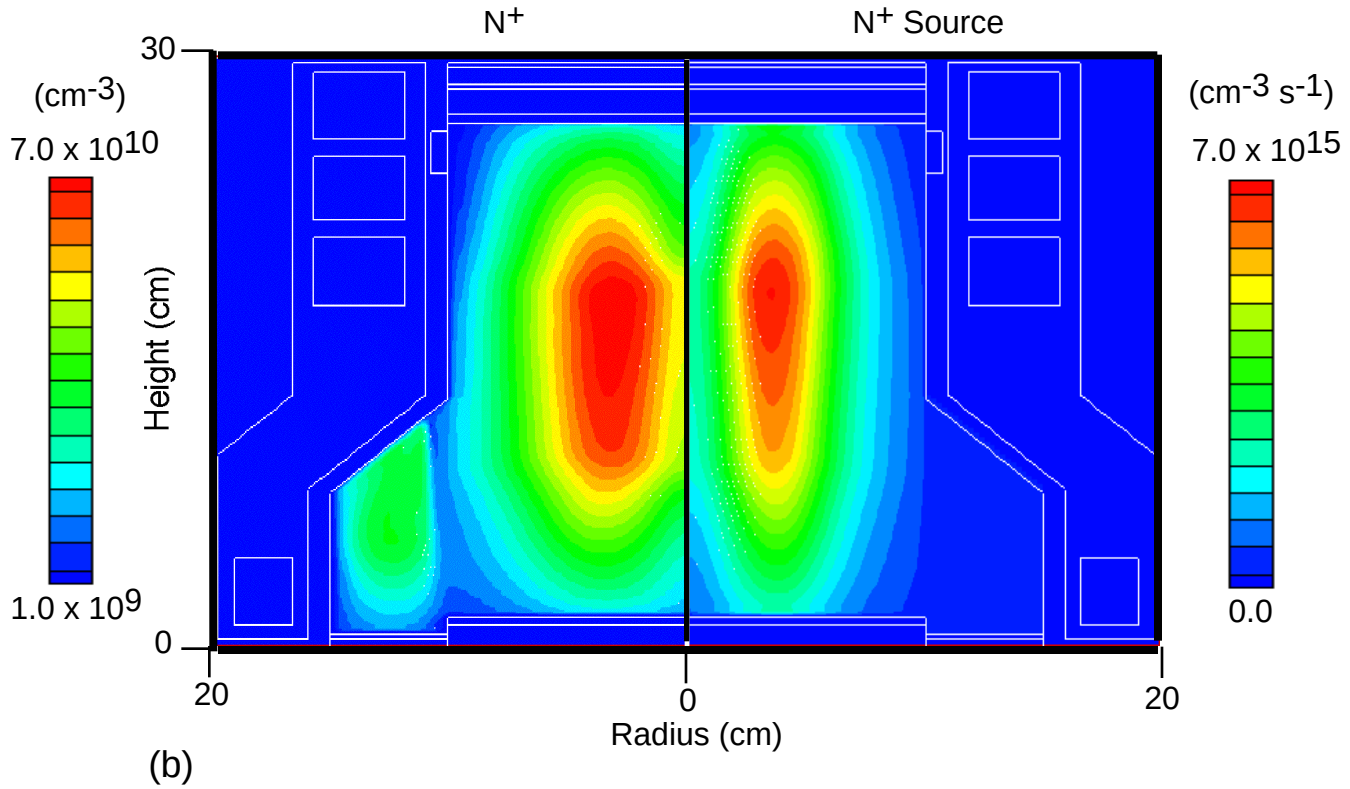

Figure 3.9 (a) N_2^+ density and N_2^+ source rate (b) N^+ density and N^+ source inside the ECR processing tool for base case conditions.

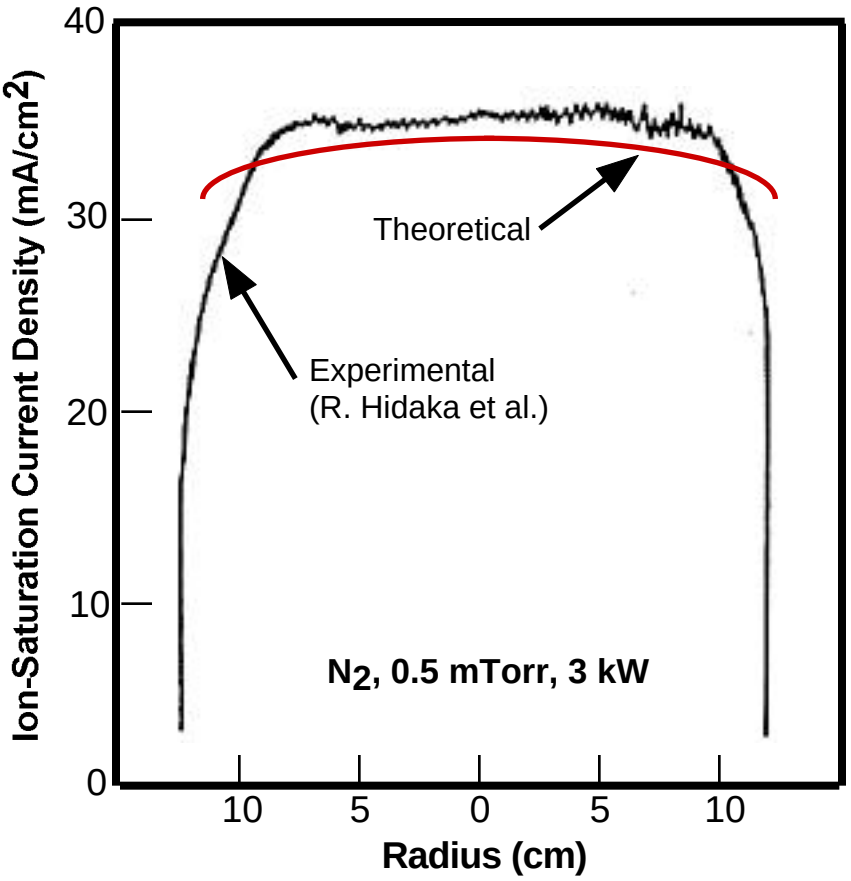

Figure 3.10 Experimetal and computed radial profiles of the ion saturation current density in an ECR processign tool for a TE_{01} electric field mode.

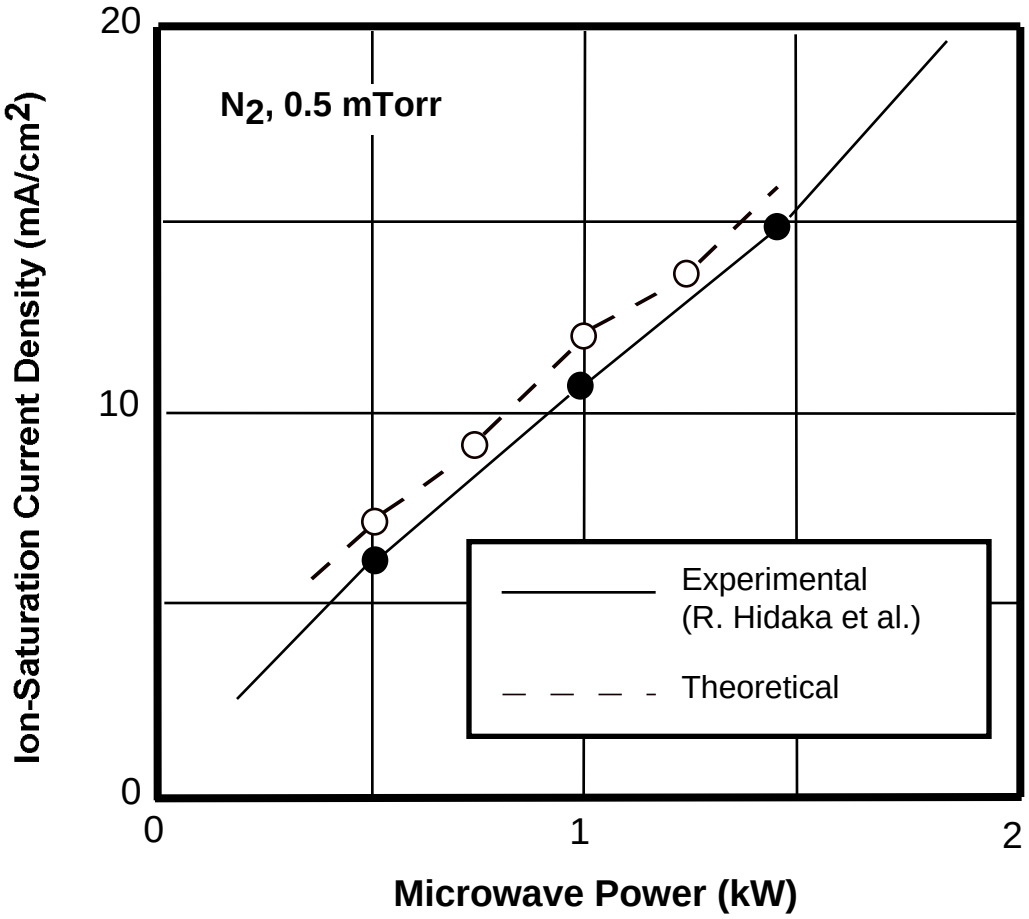

Figure 3.11 Experimetal and computed values of the ion saturation current density for a TE_{01} electric field mode with varying power.

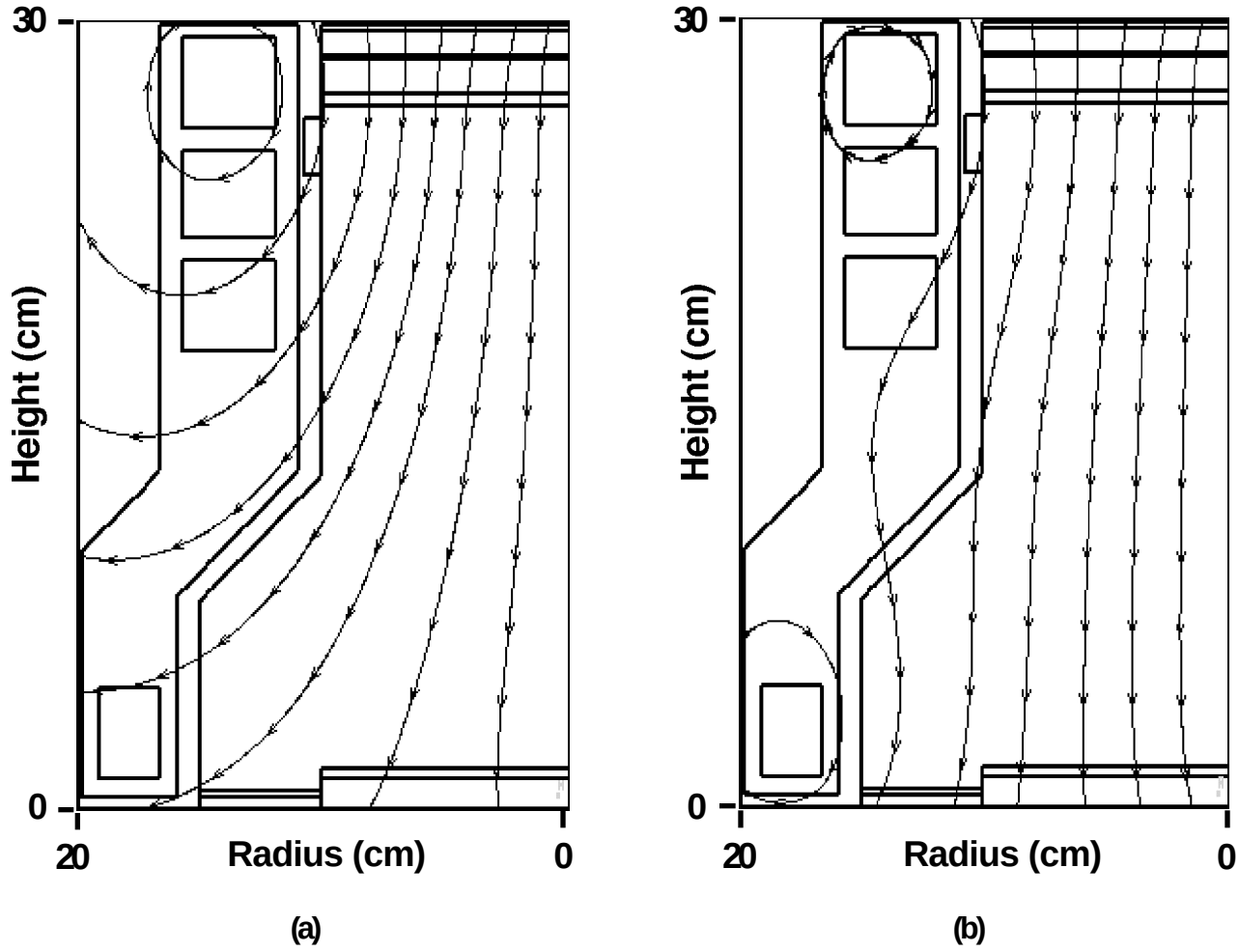

Figure 3.12 Magnetic flux in the ECR processing tool (a) without activation of the magnetic subcoil (b) with activation of the magnetic subcoil.

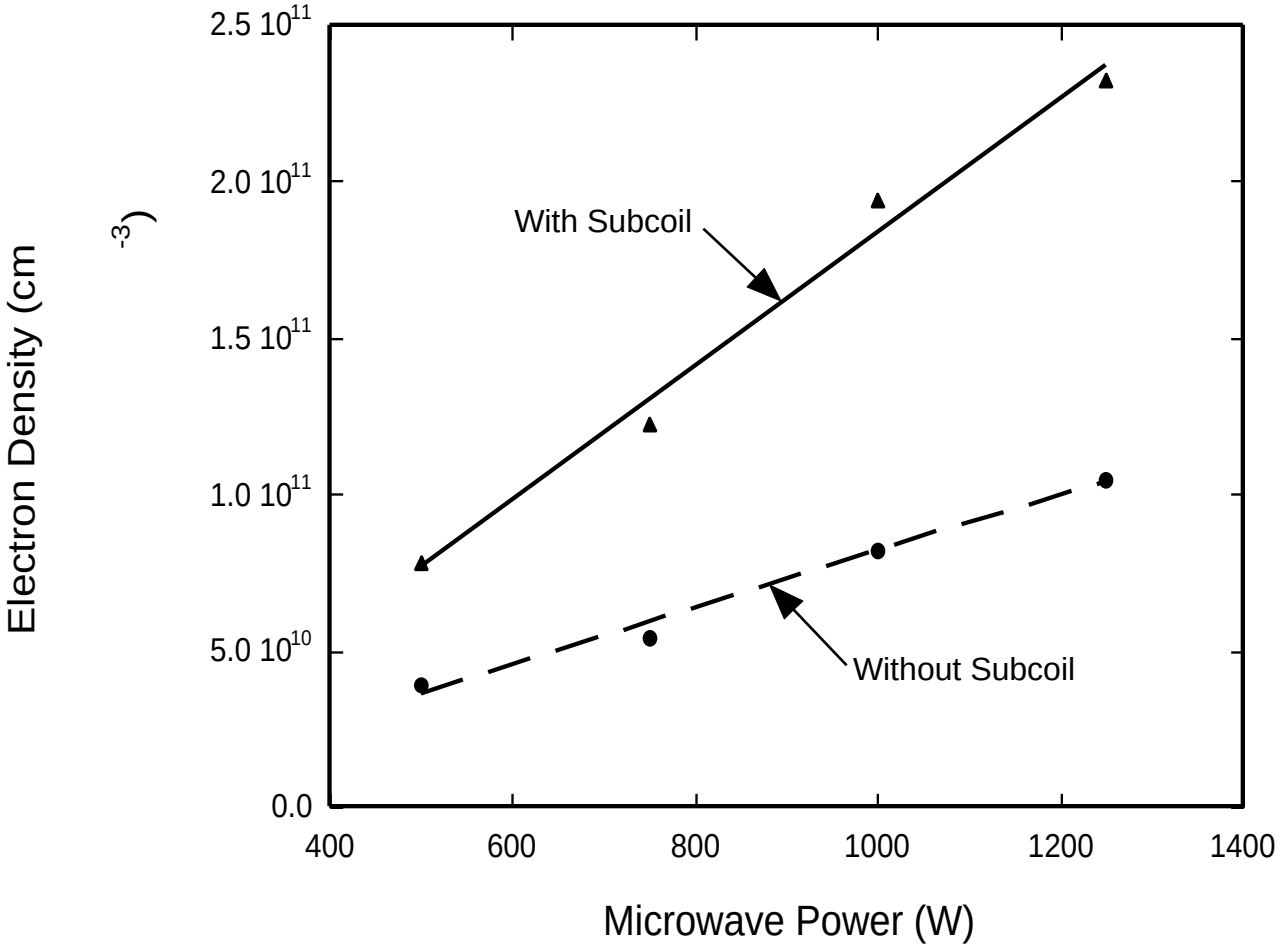

Figure 3.13 Average reactor electron density with and without activation of the magnetic subcoil as a function of power.

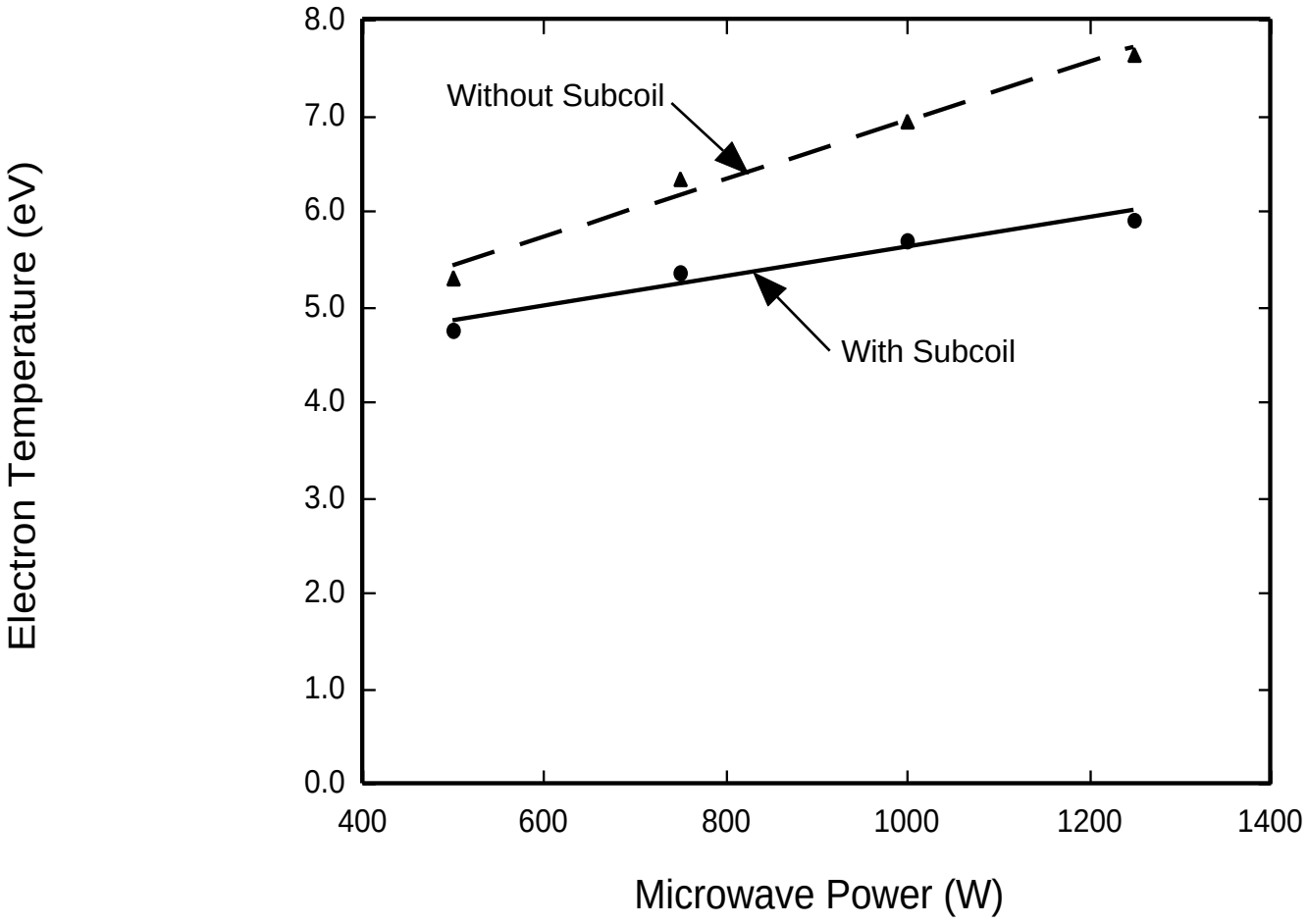

Figure 3.14 Average reactor electron temperature with and without activation of the magnetic subcoil for varying power.

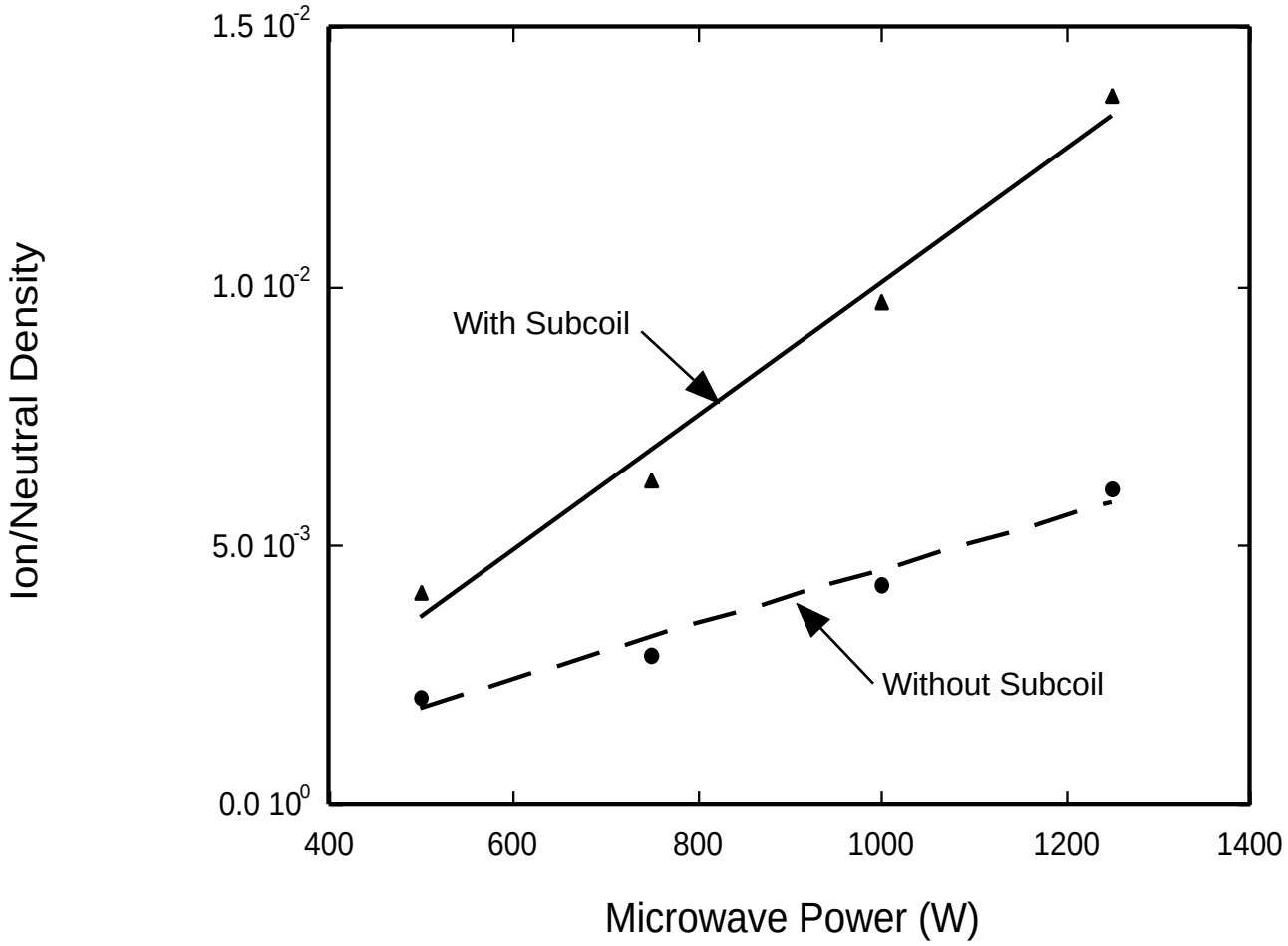

Figure 3.15 Ion to neutral density with and without activation of the magnetic subcoil as a function of power.

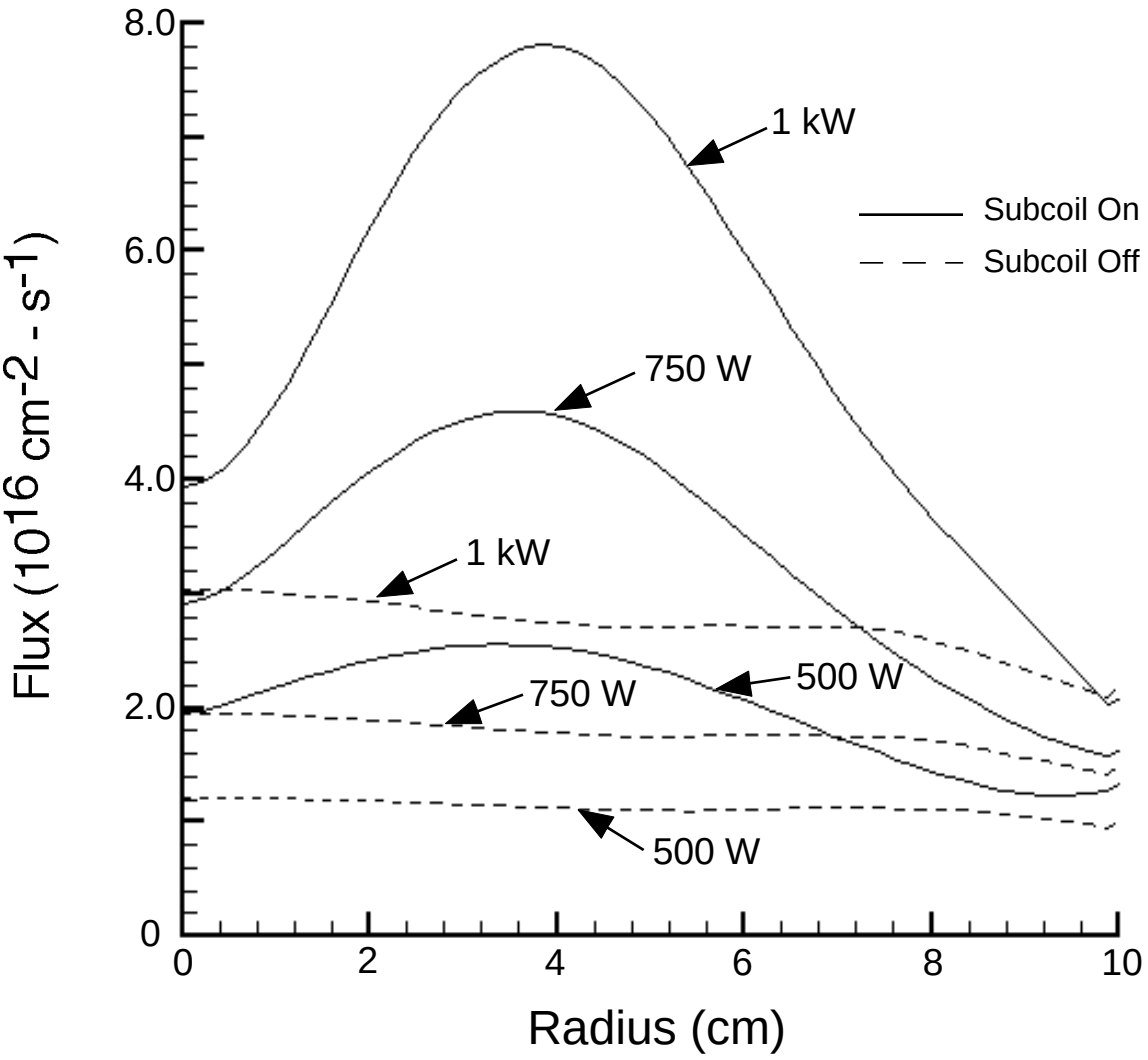

Figure 3.16 Ion flux to the substrate with and without activation of the magnetic subcoil for different powers.

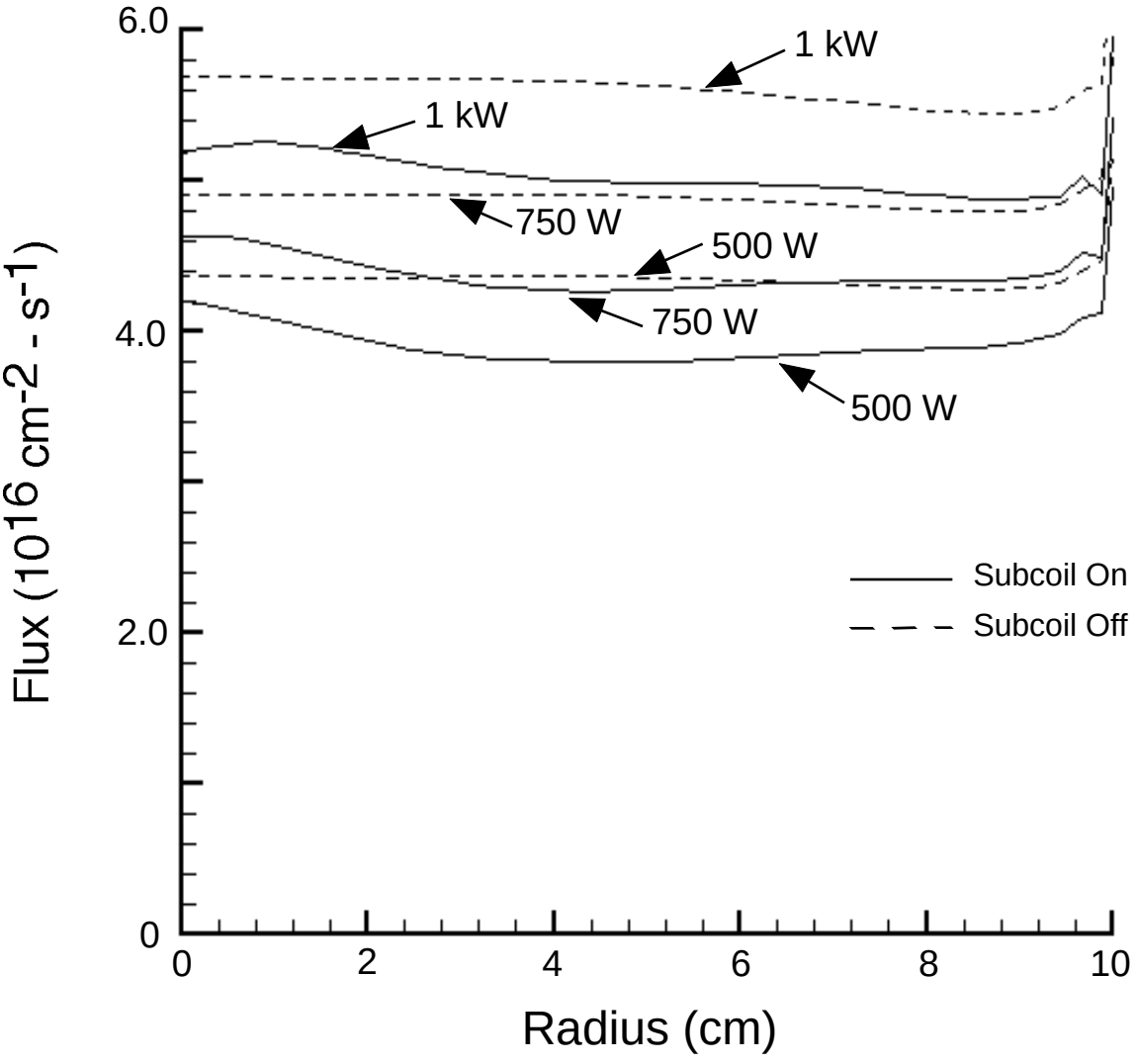

Figure 3.17 N_2(v) flux to the substrate with and without activation of the magnetic subcoil for different powers.

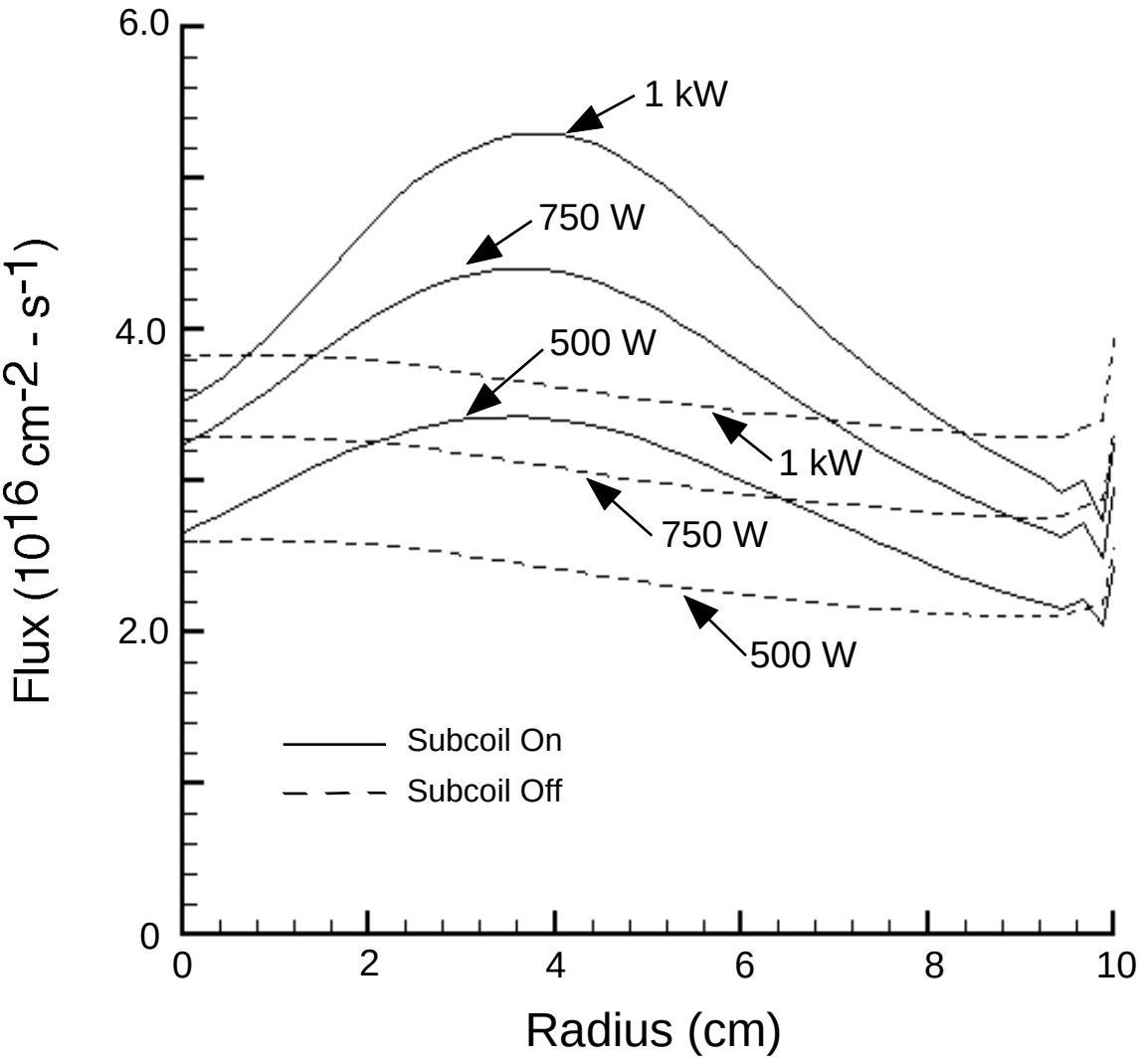

Figure 3.18 N_2^* flux to the substrate with and without activation of the magnetic subcoil for different powers.

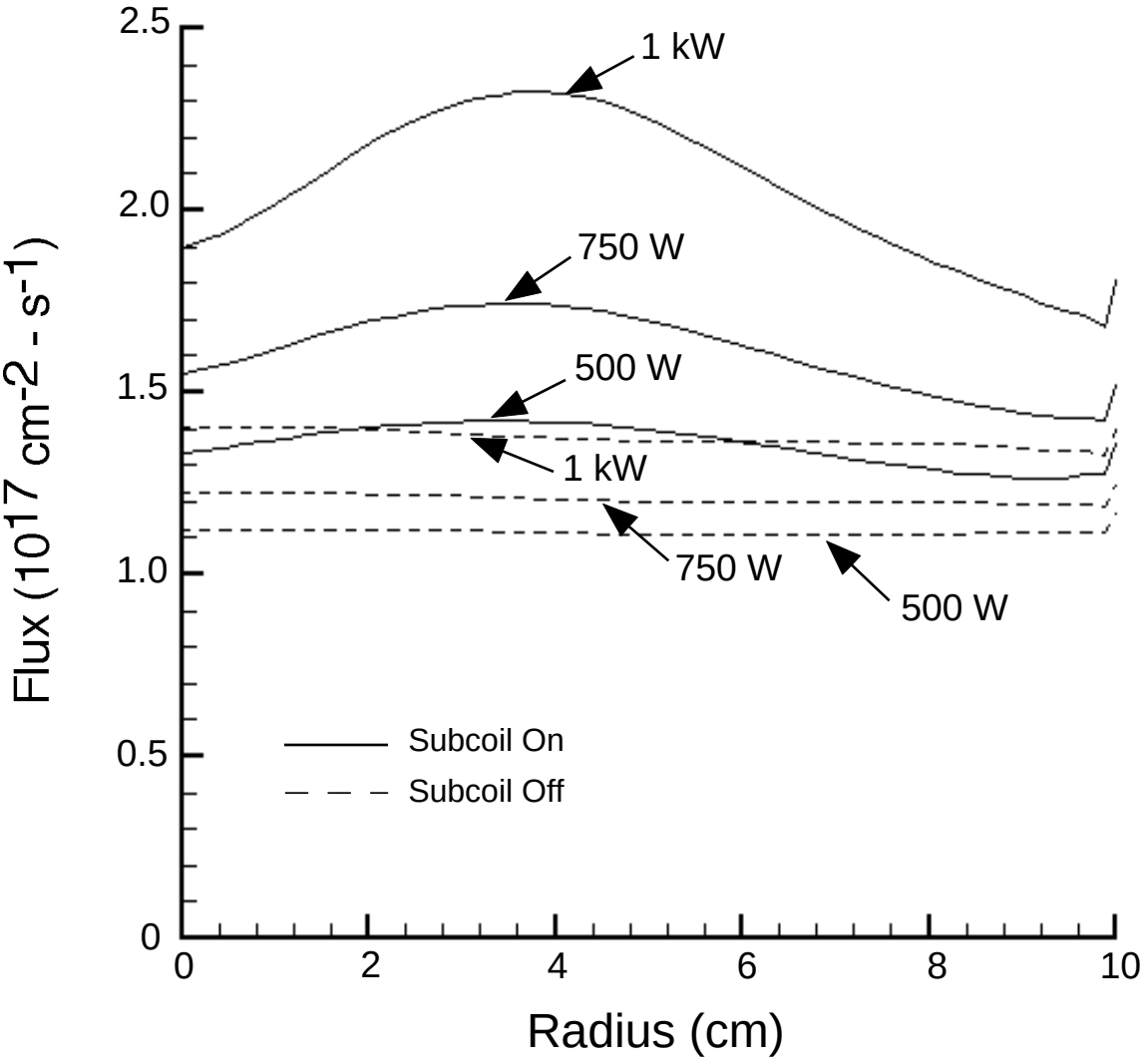

Figure 3.19 Atomic nitrogen, N, flux to the substrate with and without activation of the magnetic subcoil for different powers.

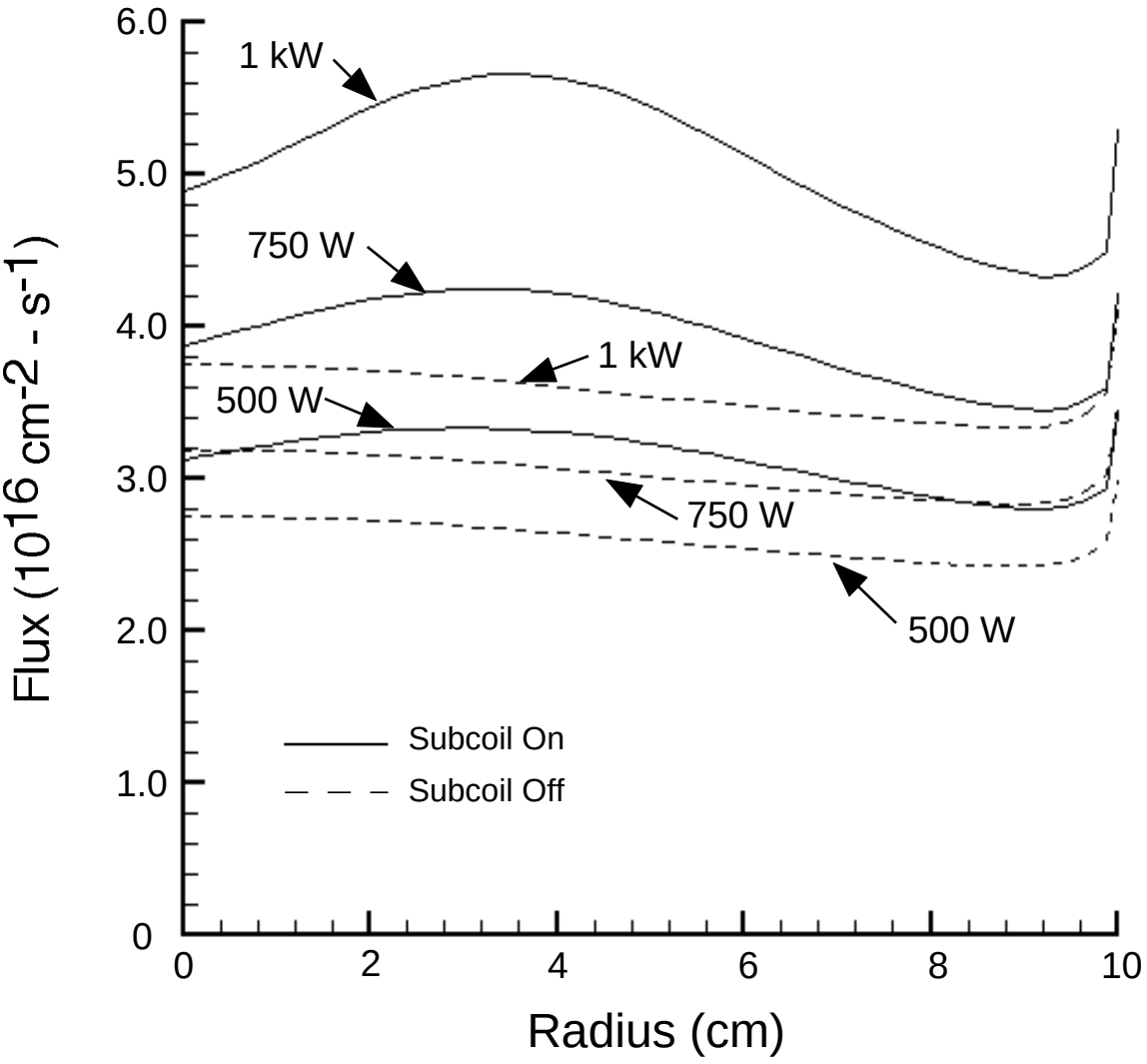

Figure 3.20 N^* flux to the substrate with and without activation of the magnetic subcoil for different powers.

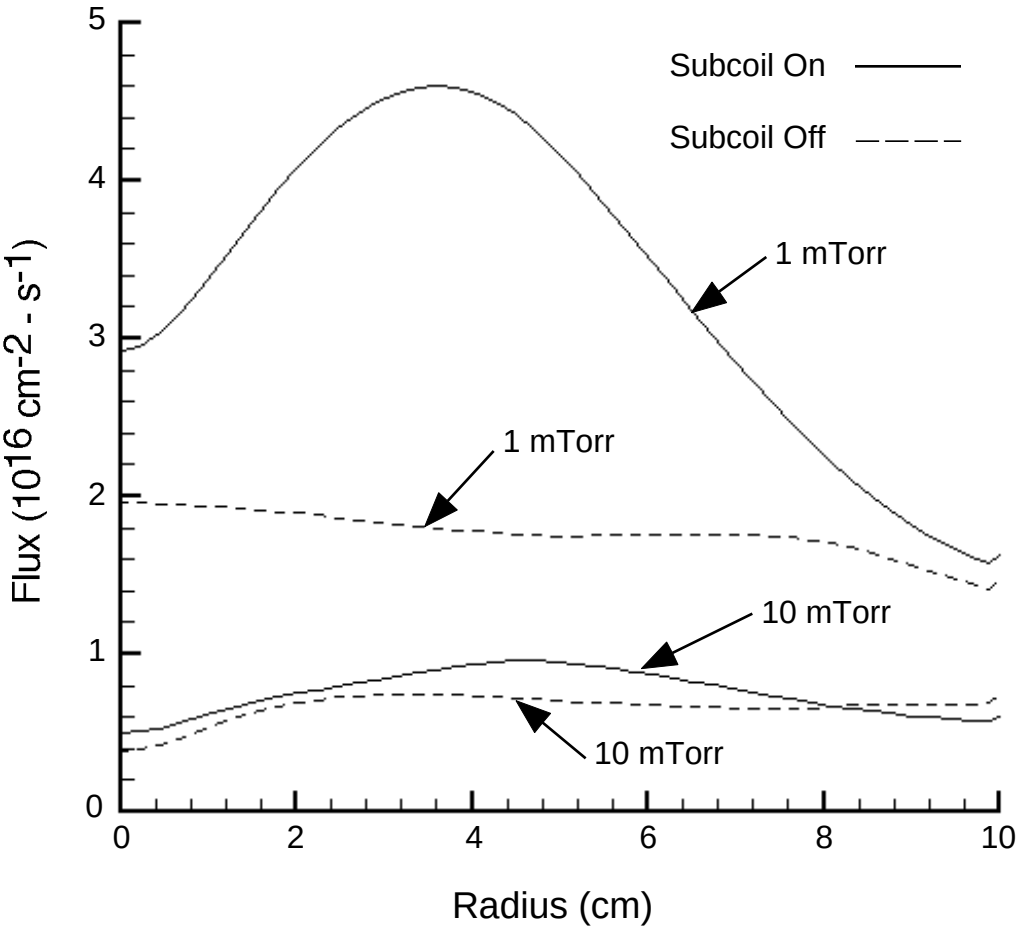

Figure 3.21 Ion flux to the substrate with and without activation of the magnetic subcoil for different pressures.

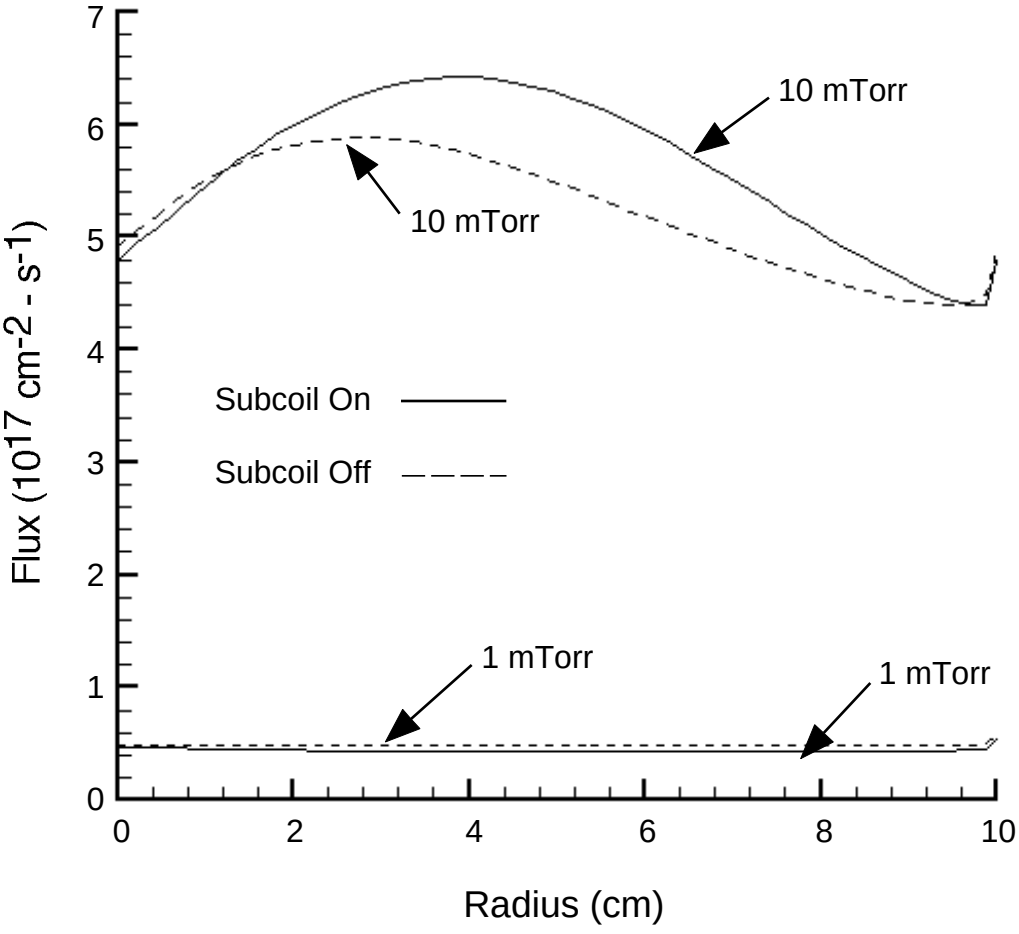

Figure 3.22 $N_2(v)$ flux to the substrate with and without activation of the magnetic subcoil for different pressures.

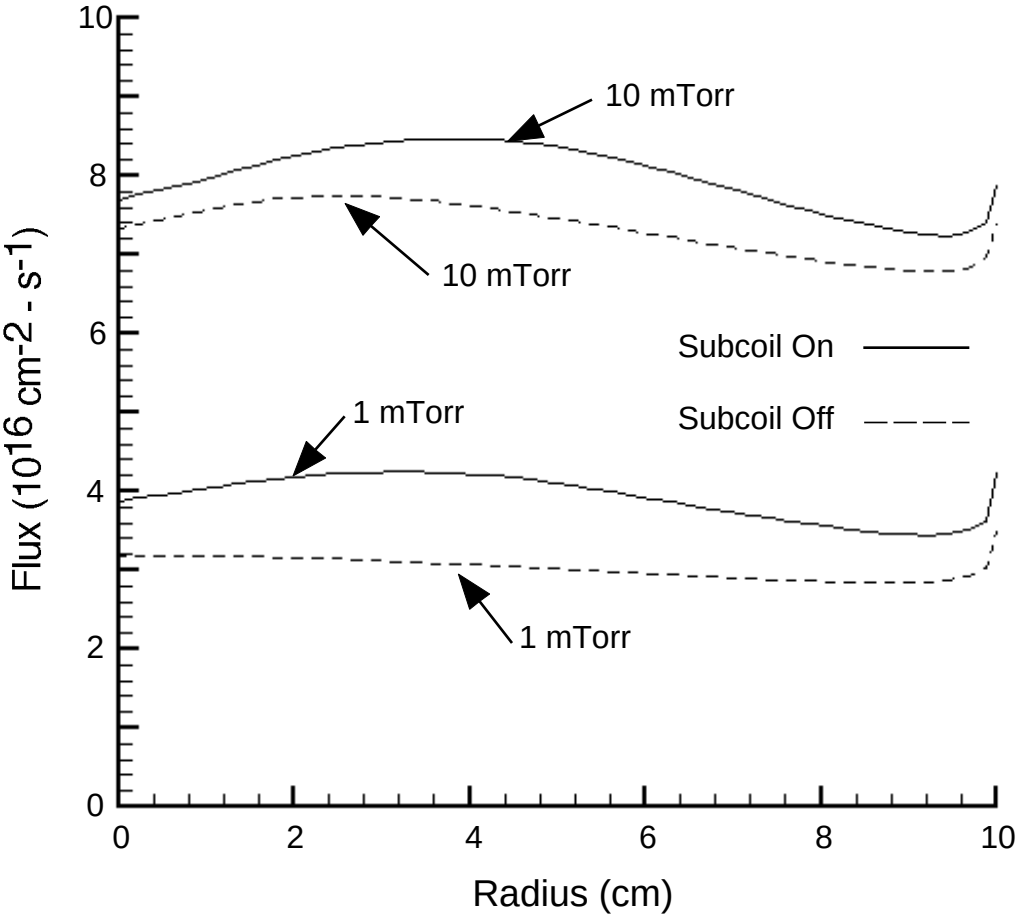

Figure 3.23 N* flux to the substrate with and without activation of the magnetic subcoil for different pressures.

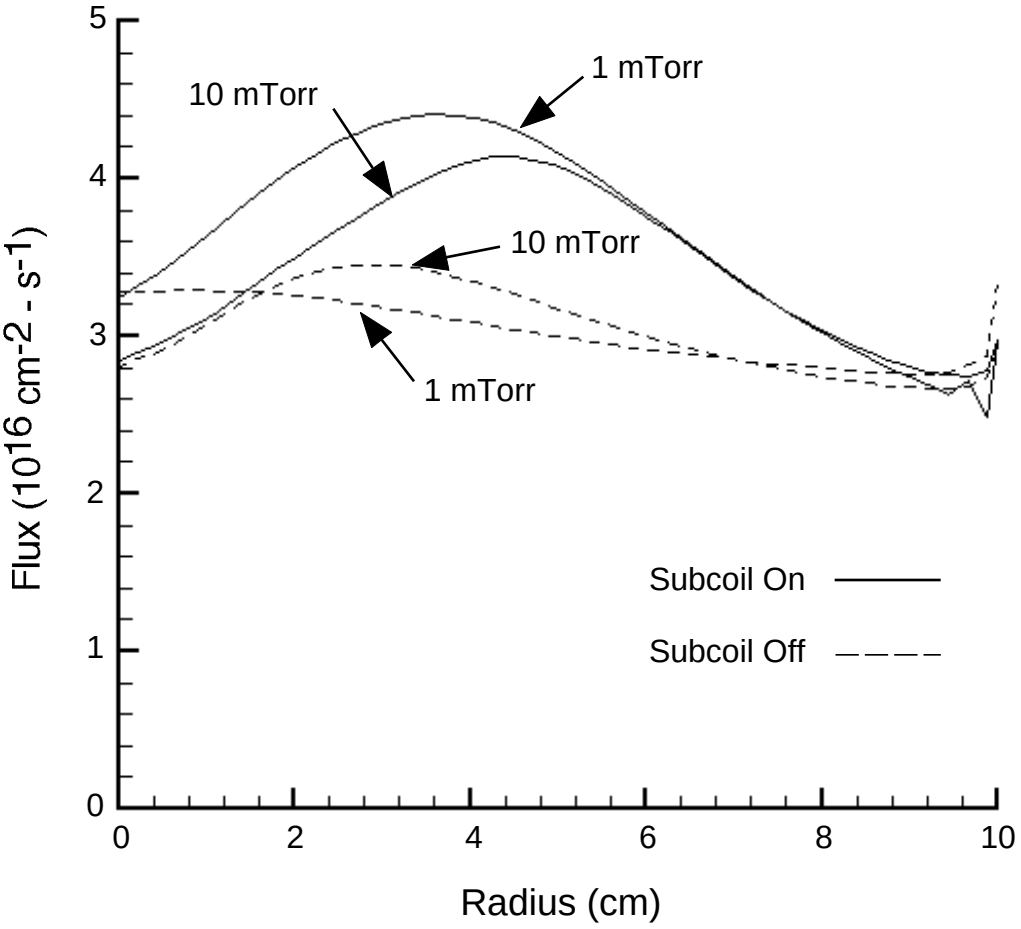

Figure 3.24 N_2^* flux to the substrate with and without activation of the magnetic subcoil for different pressures.

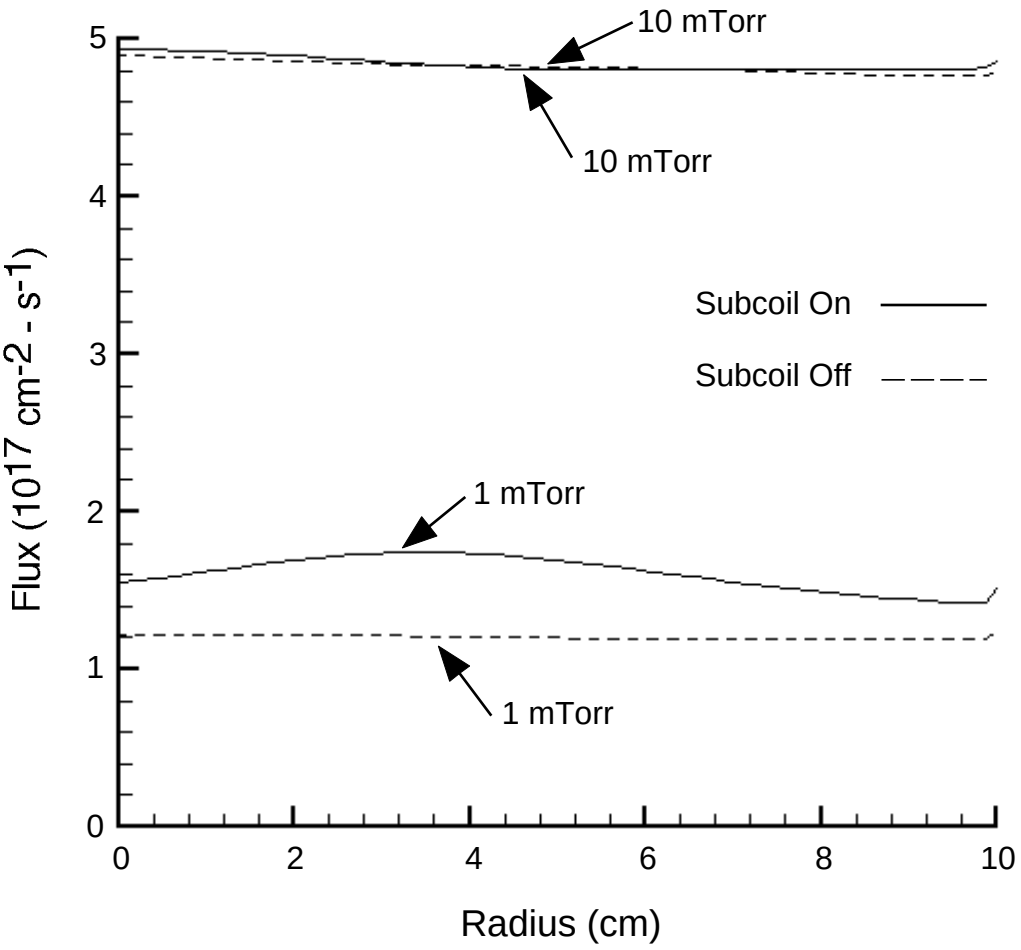

Figure 3.25 Flux of atomic nitrogen, N, to the substrate with and without activation of the magnetic subcoil for different pressures.

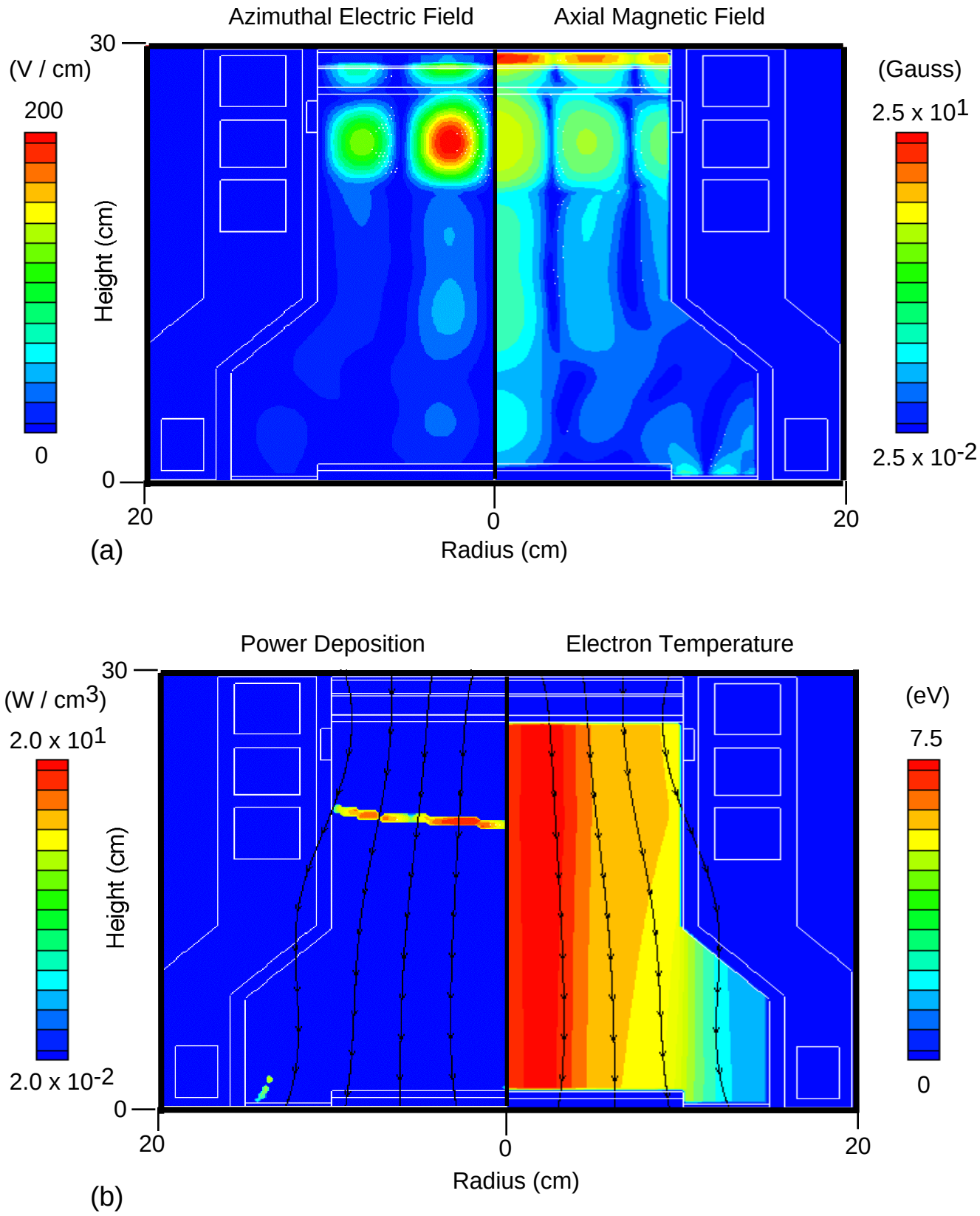

Figure 3.26 Azimuthal electric field component and axial magnetic field component of incident electromagnetic field (b) power deposition and electron temperature inside the ECR processing tool.

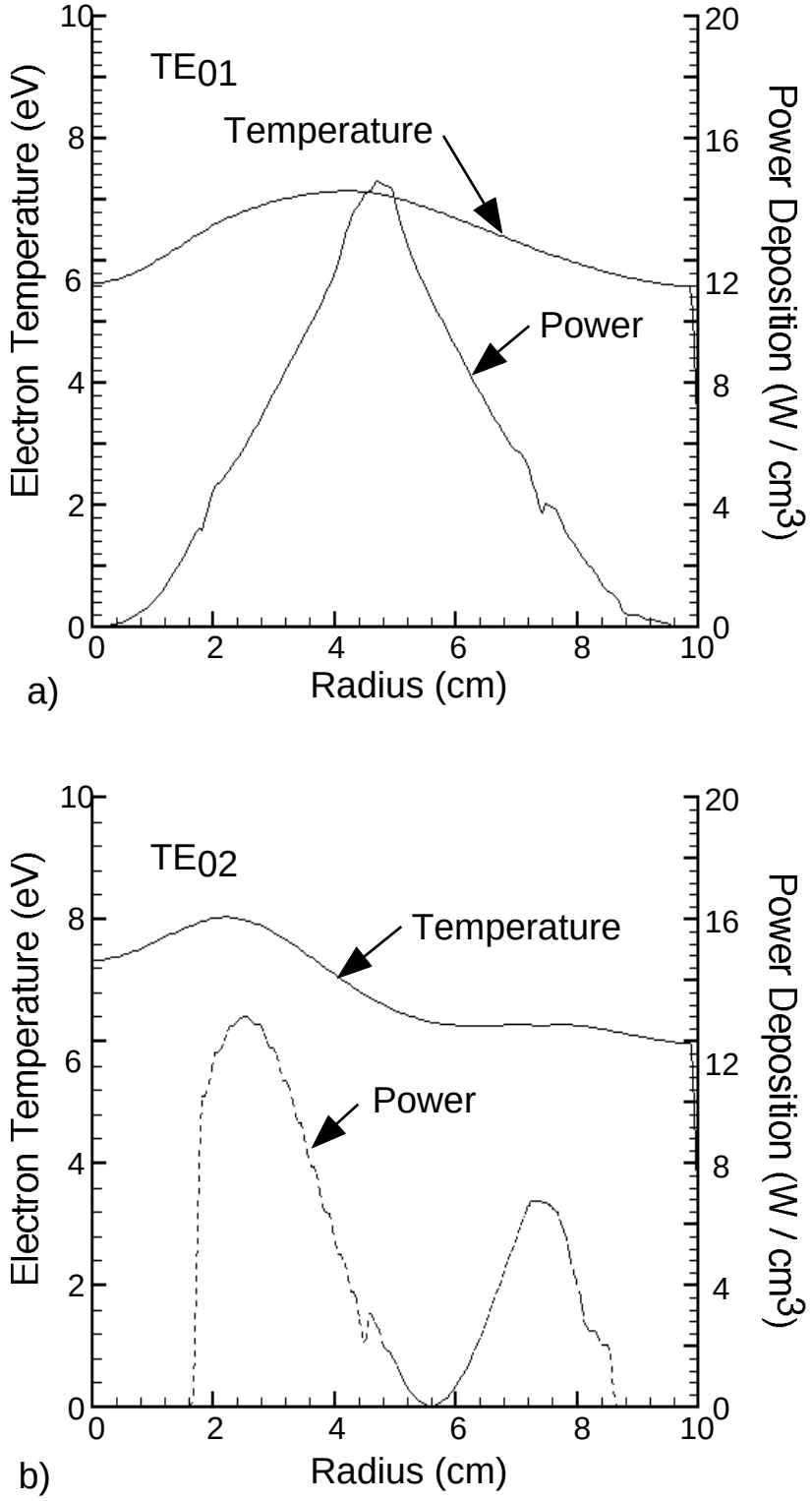

Figure 3.27 Radial profiles of electron temperature and power deposition for the (a) TE_{01} (b) TE_{02} mode in the resonance zone (z=20 cm).

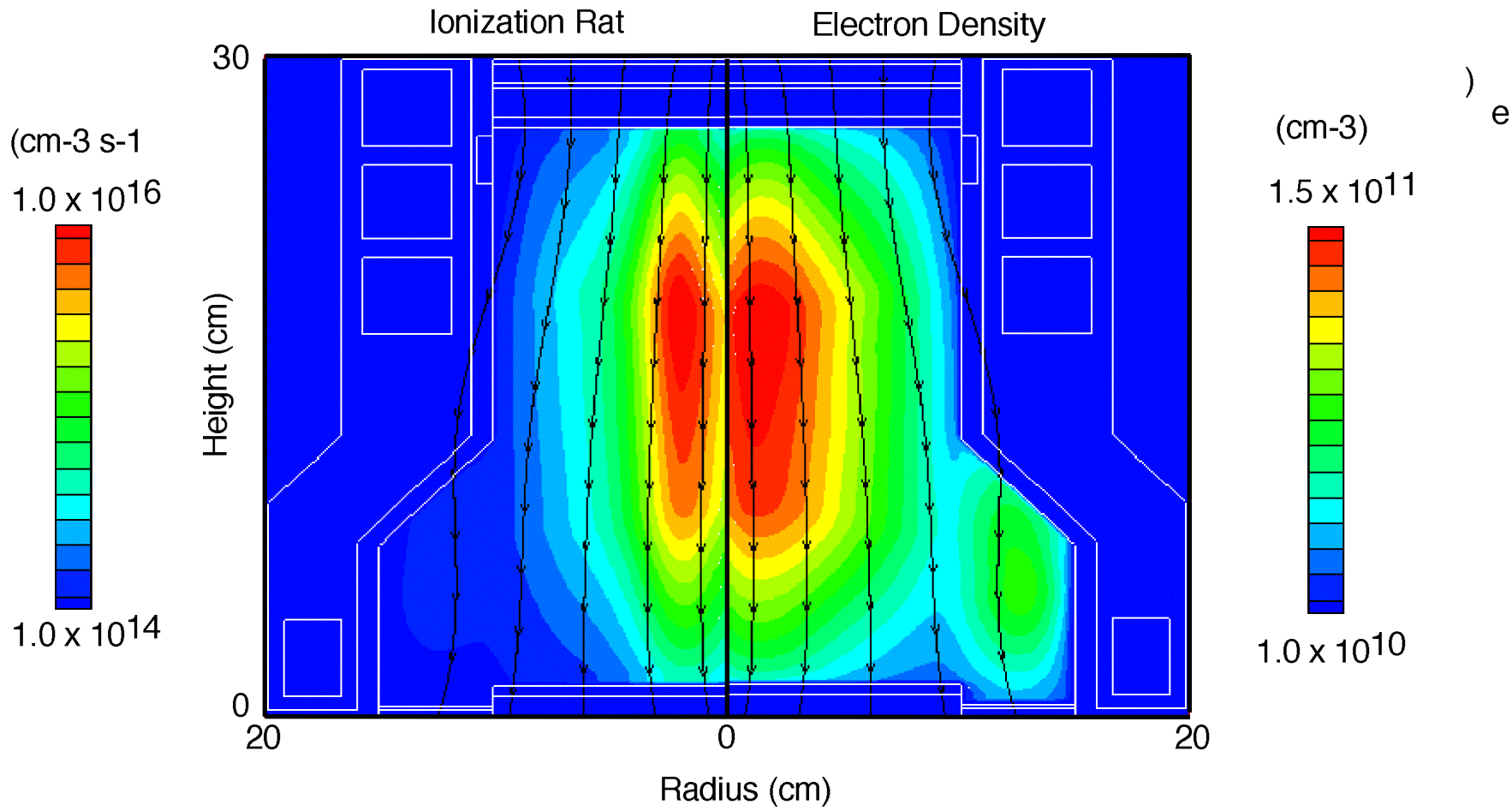

Figure 3.28 Ionization rate and electron density inside the ECR processing tool for a TE_{02} mode. Vector (black) represent magnetic flux lines.

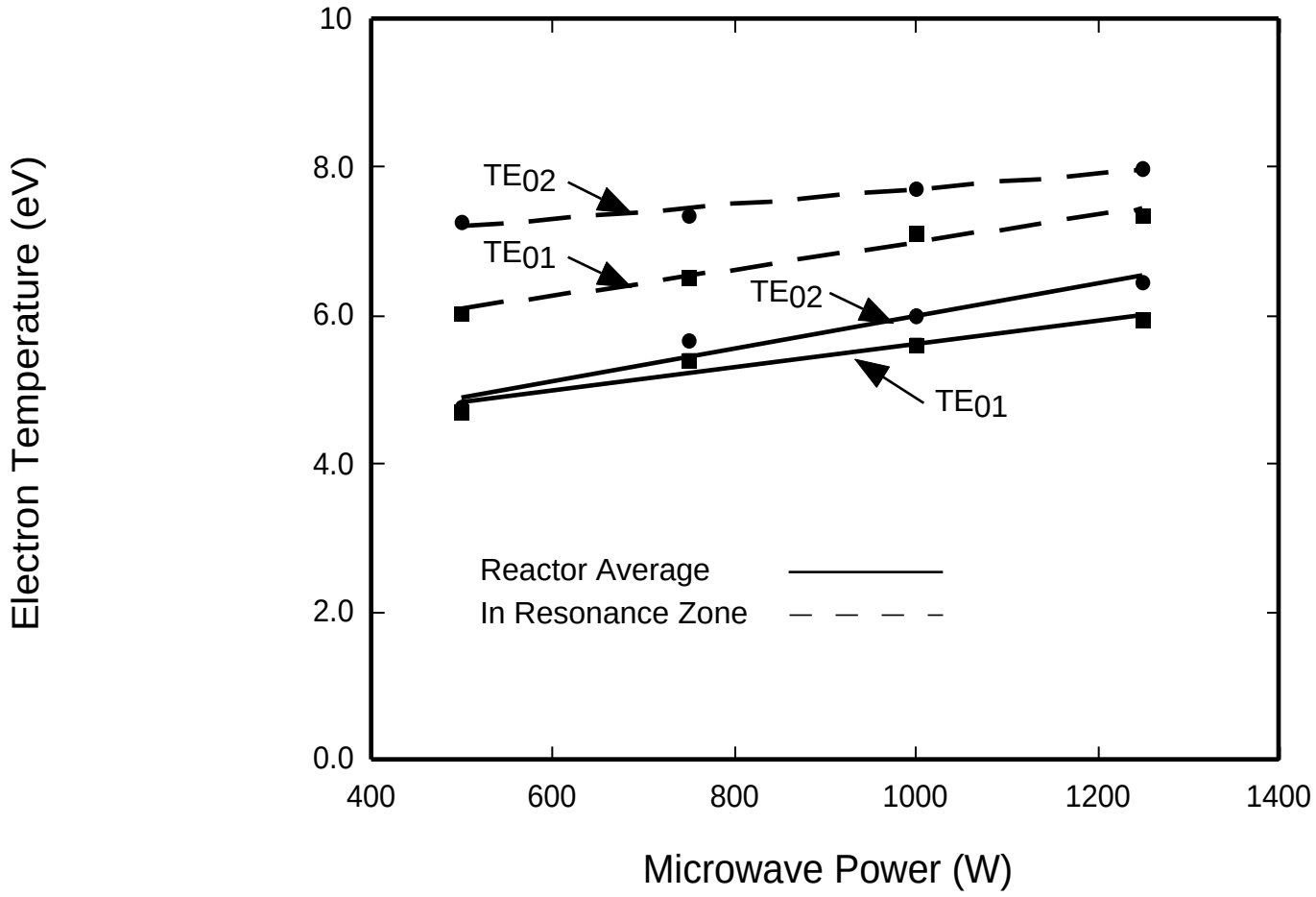

Figure 3.29 Reactor average electron temperature and average electron temperature in resonance zone for the TE_{01} and TE_{02} mode as a function of power.

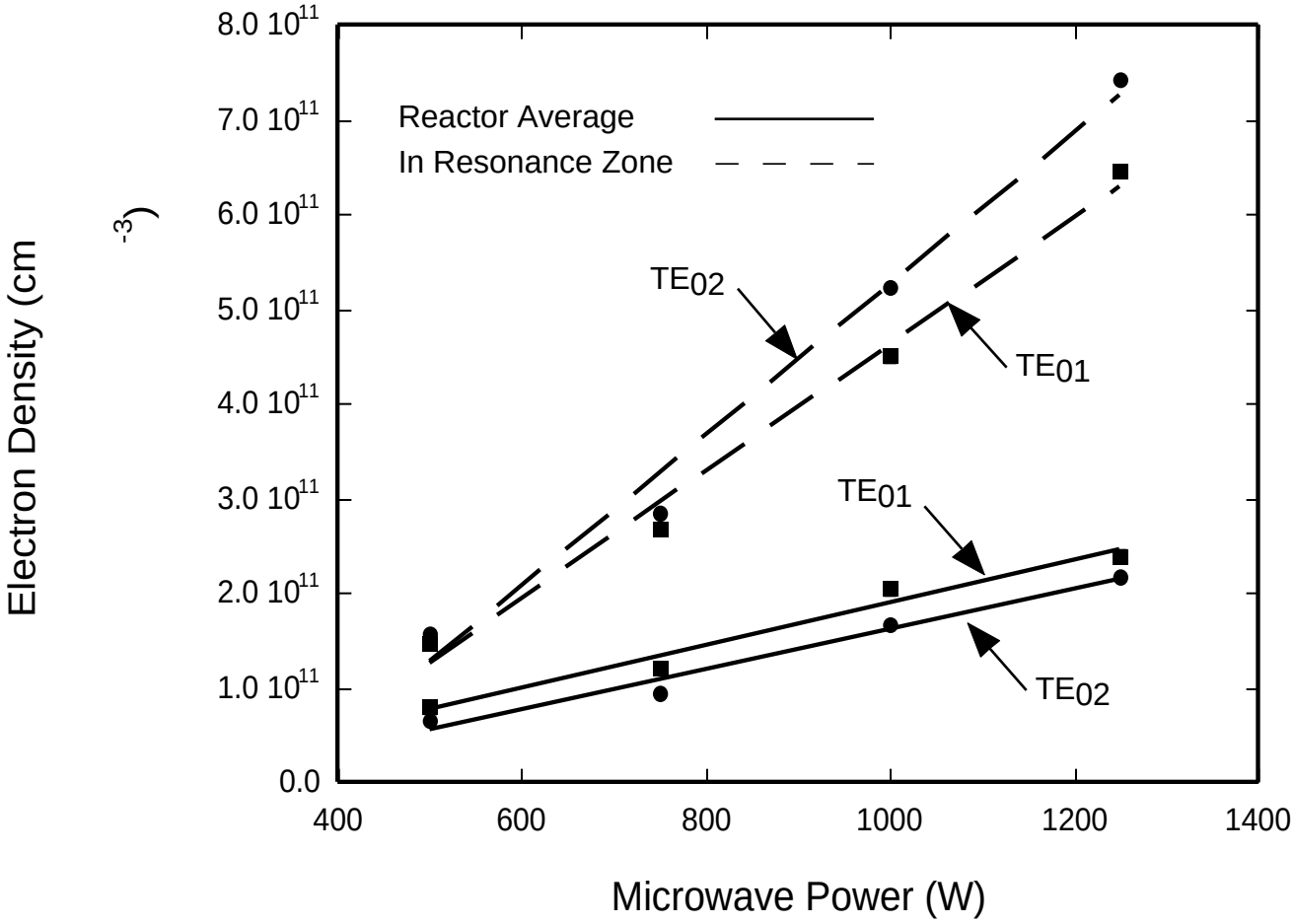

Figure 3.30 Reactor average electron density and average electron density in resonance zone for the TE_{01} and TE_{02} mode as a function of power.

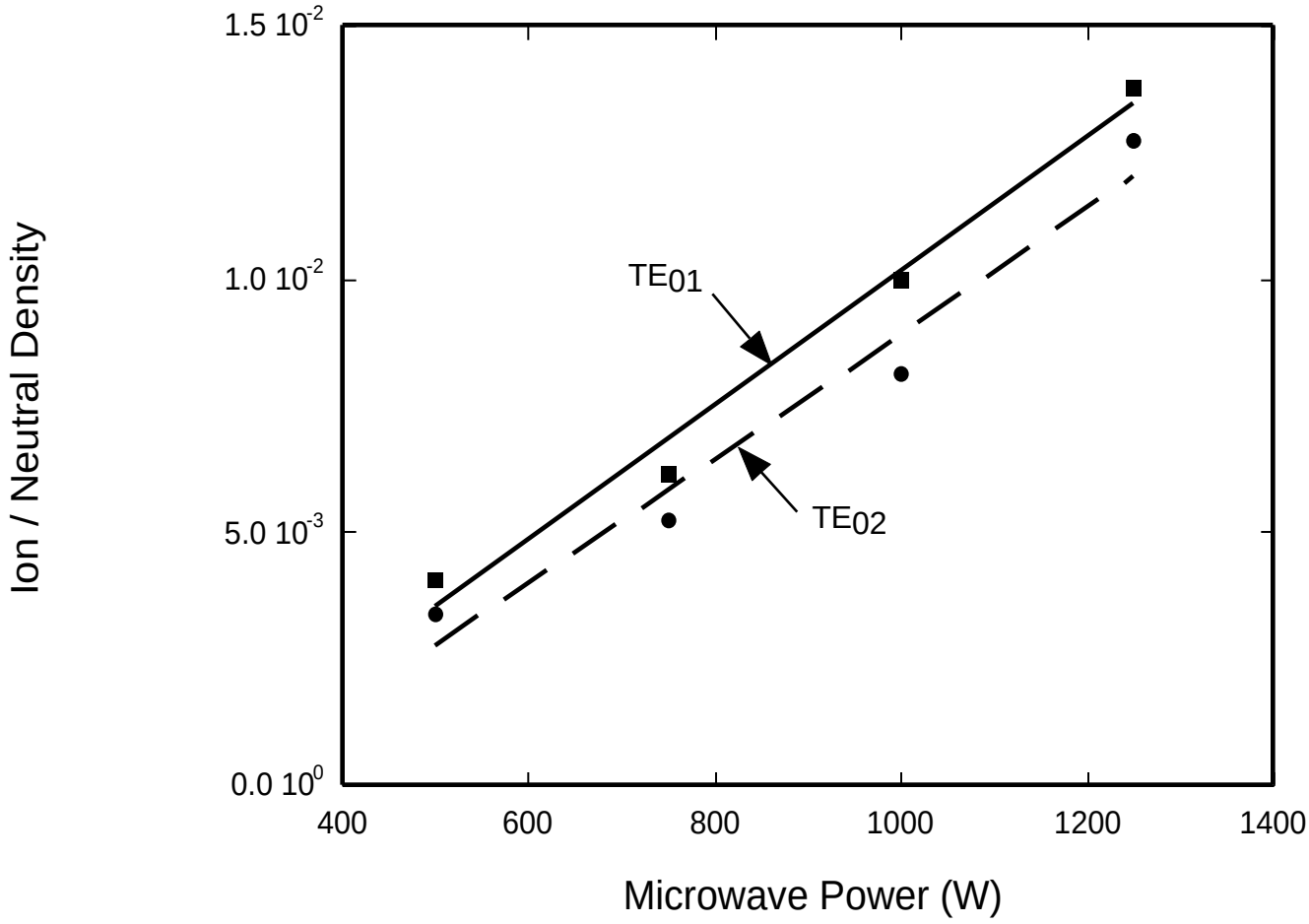

Figure 3.31 Ion to neutral density ratio for the TE_{01} and TE_{02} mode as a function of power.

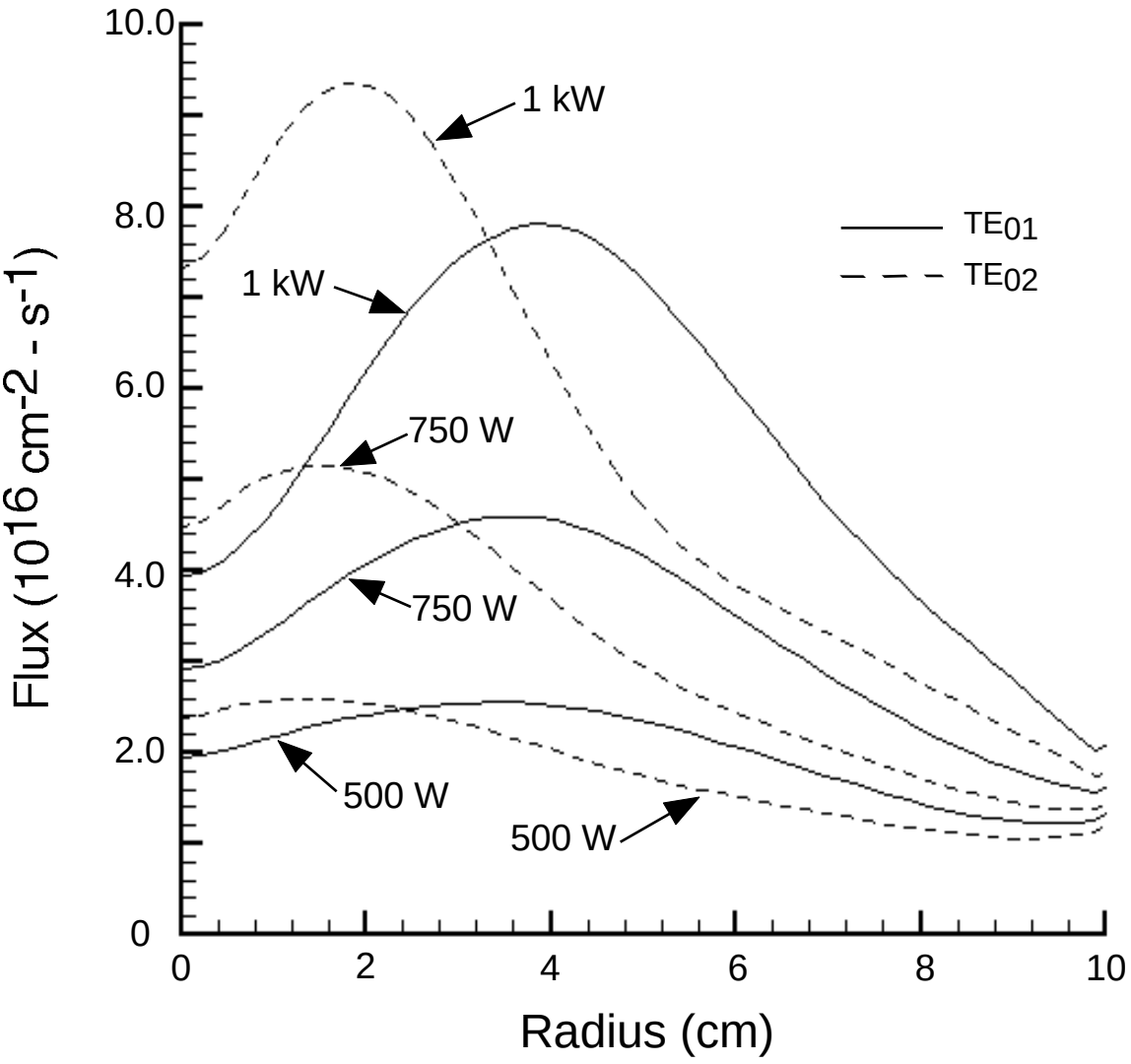

Figure 3.32 Ion flux to the substrate for the TE_{01} and the TE_{02} mode for different powers.

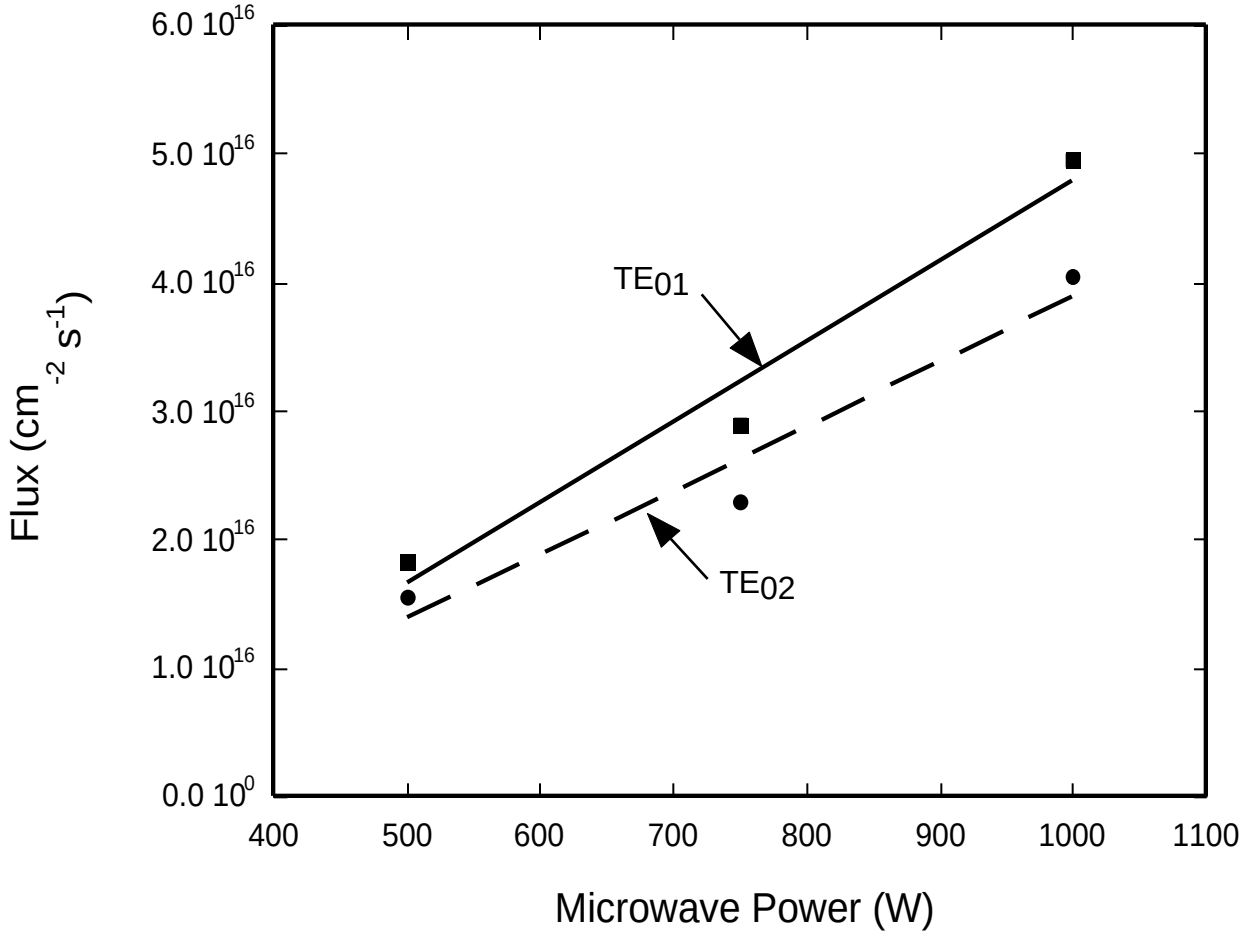

Figure 3.33 Average ion flux to the substrate for the TE_{01} and TE_{02} mode as a function of power.

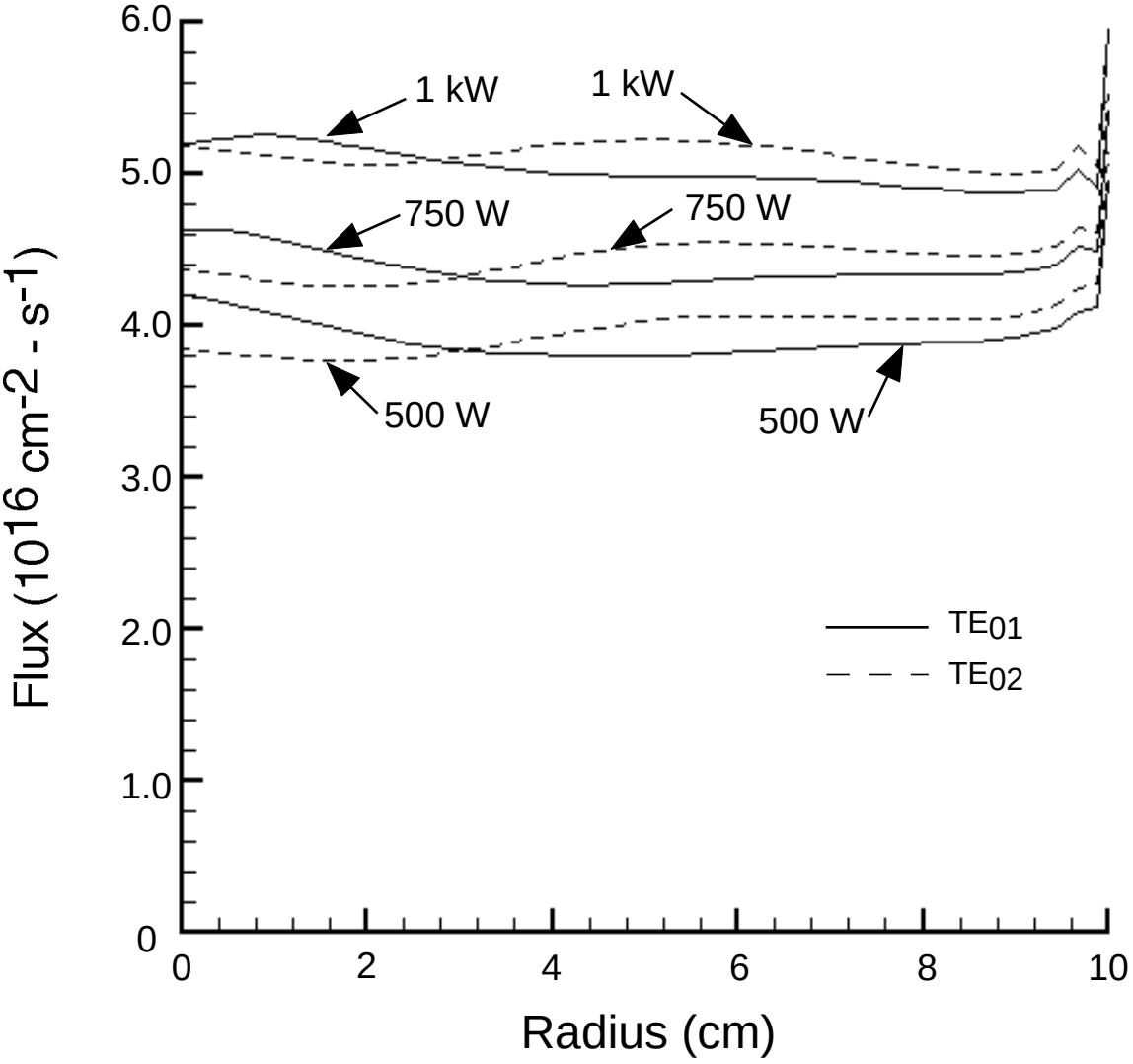

Figure 3.34 $N_2(v)$ flux to the substrate for the TE_{01} and the TE_{02} mode for different powers.

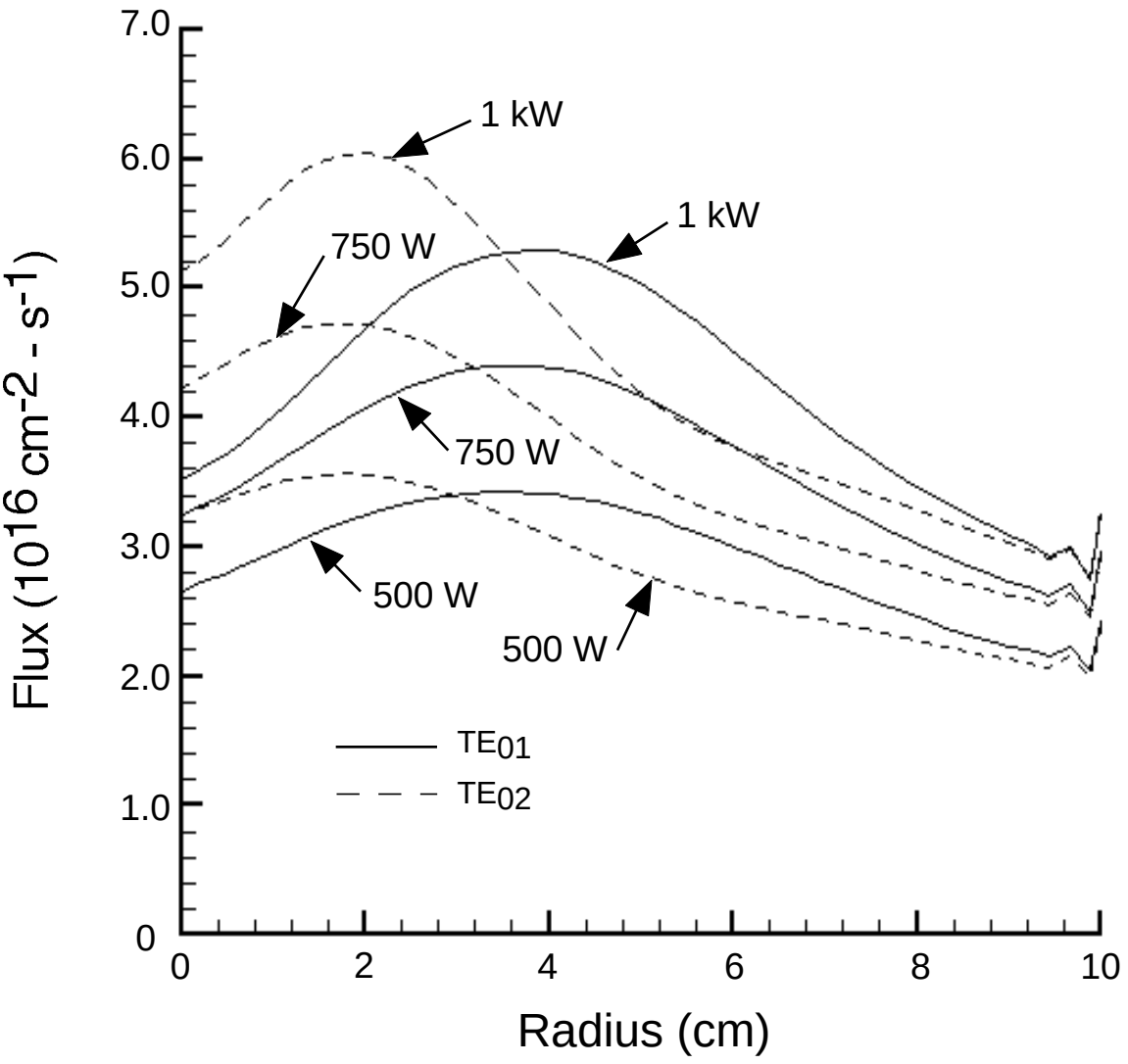

Figure 3.35 N_2^* flux to the substrate for the TE_{01} and the TE_{02} mode for different powers.

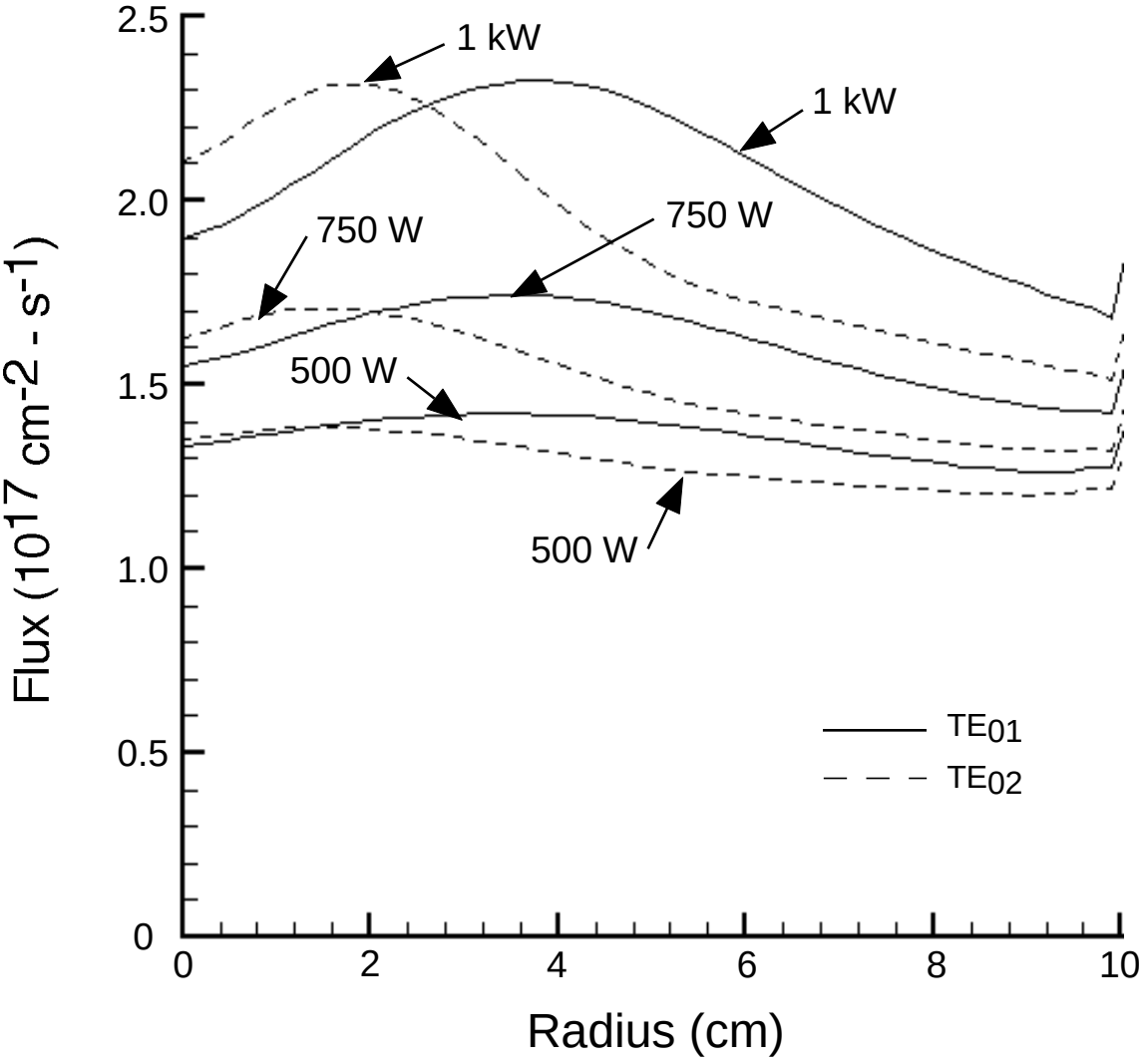

Figure 3.36 Flux of atomic nitrogen, N, to the substrate for the TE_{01} and the TE_{02} mode for different powers.

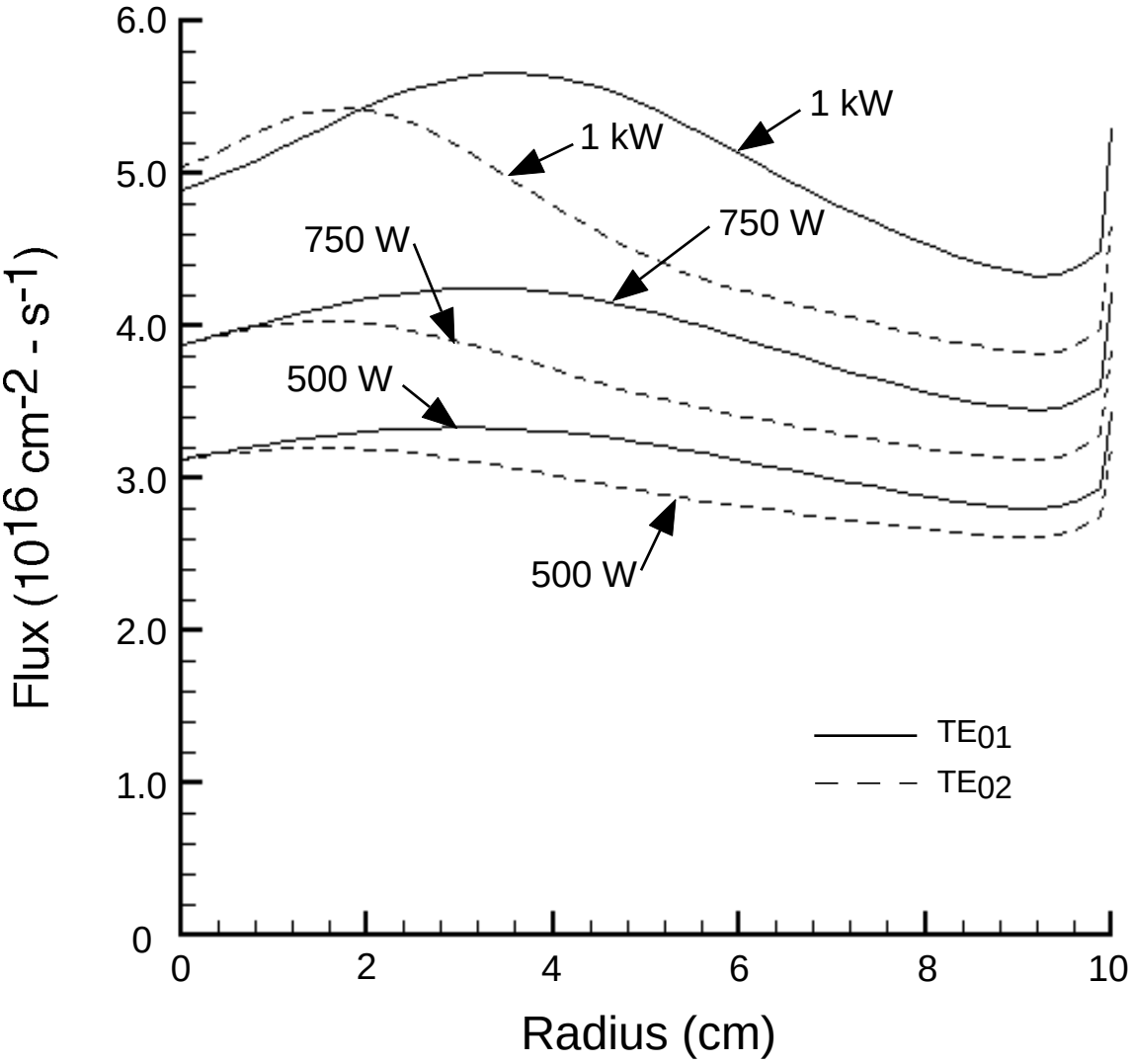

Figure 3.37 N^* flux to the substrate for the TE_{01} and the TE_{02} mode for different powers.

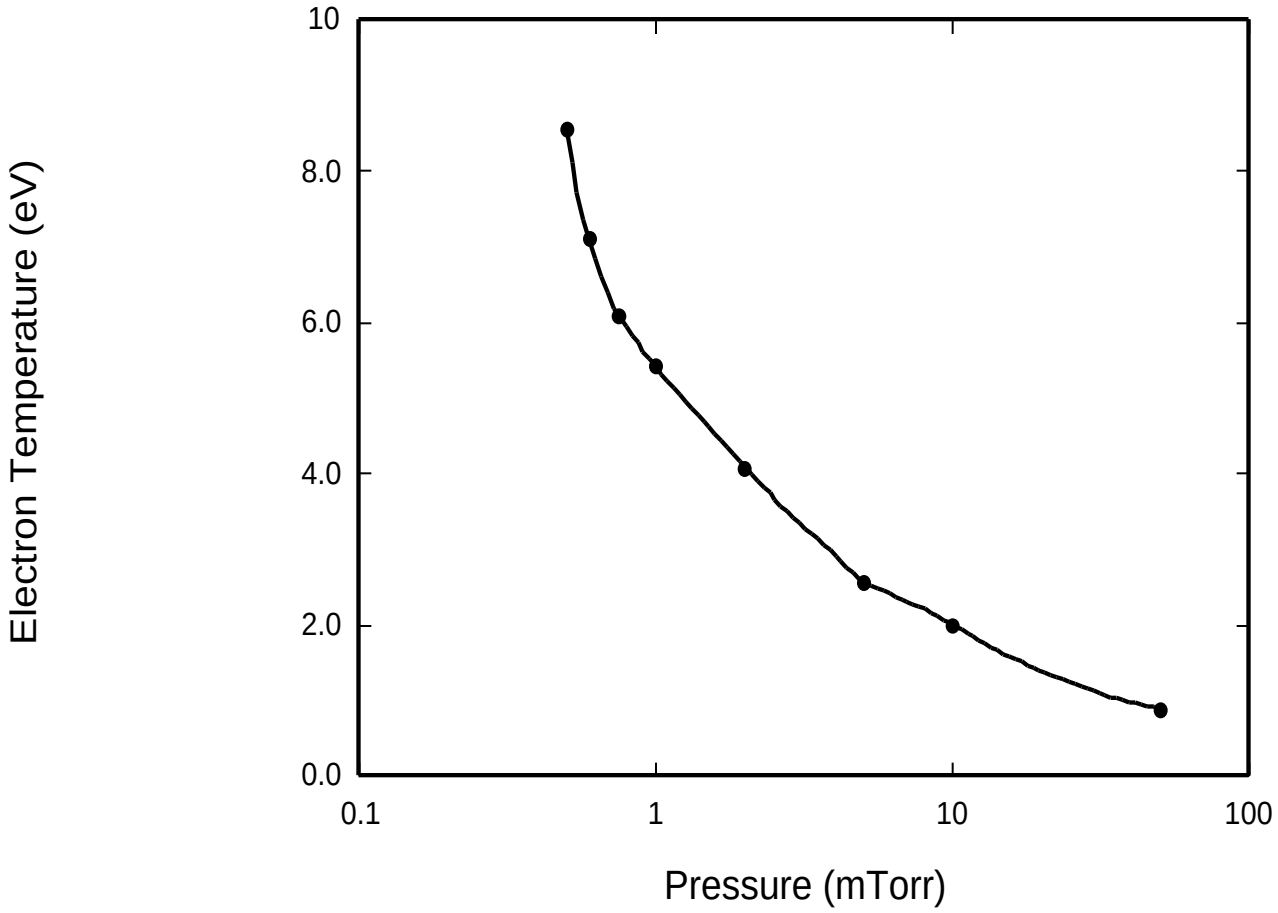

Figure 3.38 Average electron temperature as a funciton of pressure.

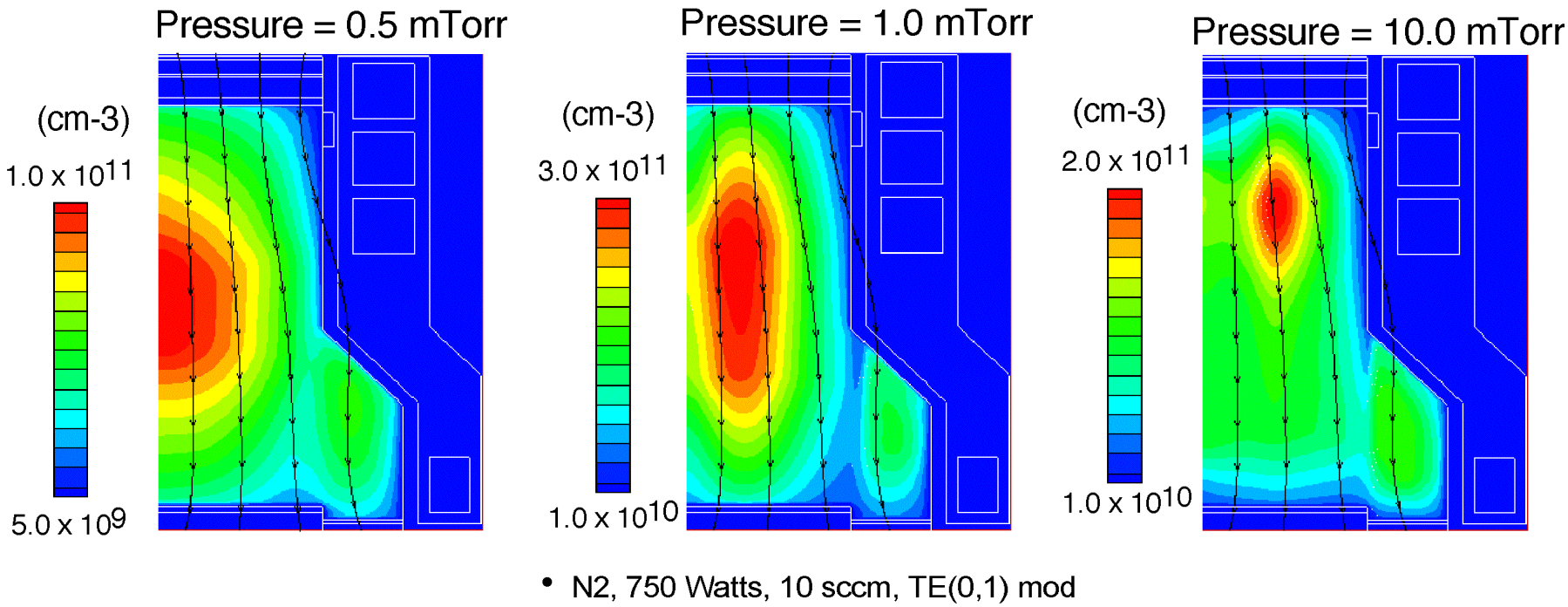

Figure 3.39 Electron density for varying pressure inside the ECR processing tool.

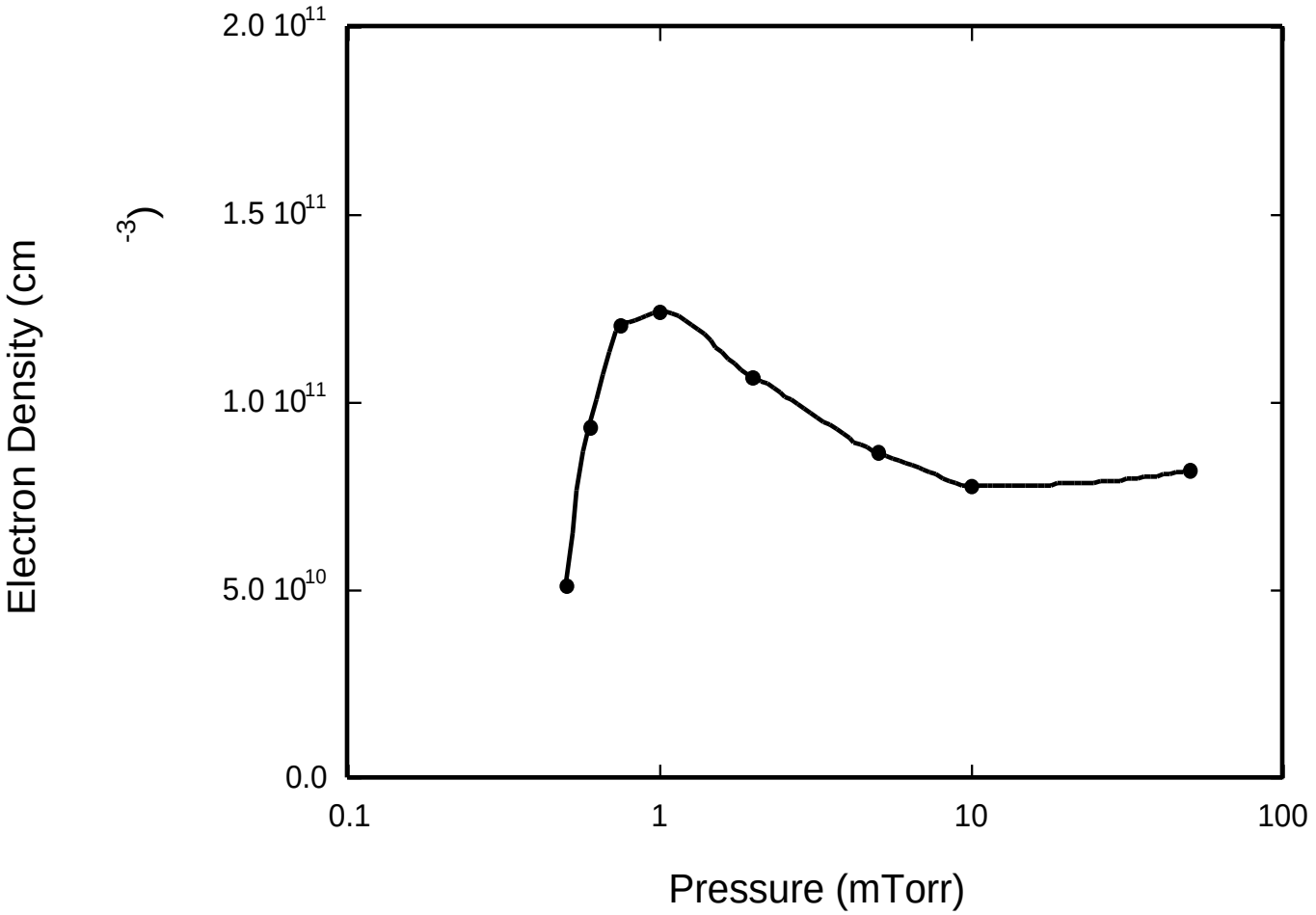

Figure 3.40 Reactor average electron density as a function of pressure.

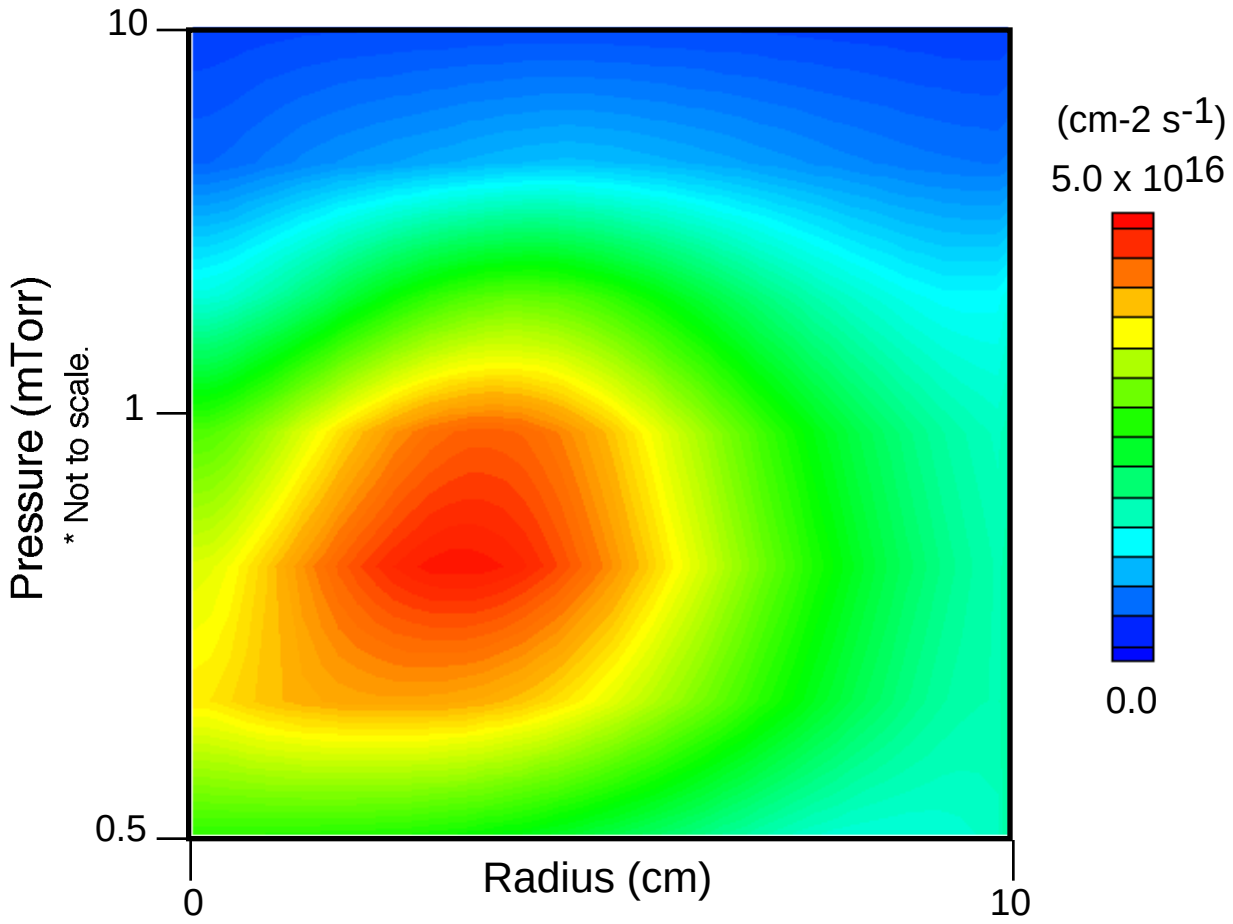

Figure 3.41 Ion flux as a function of radius for varying chamber pressure.

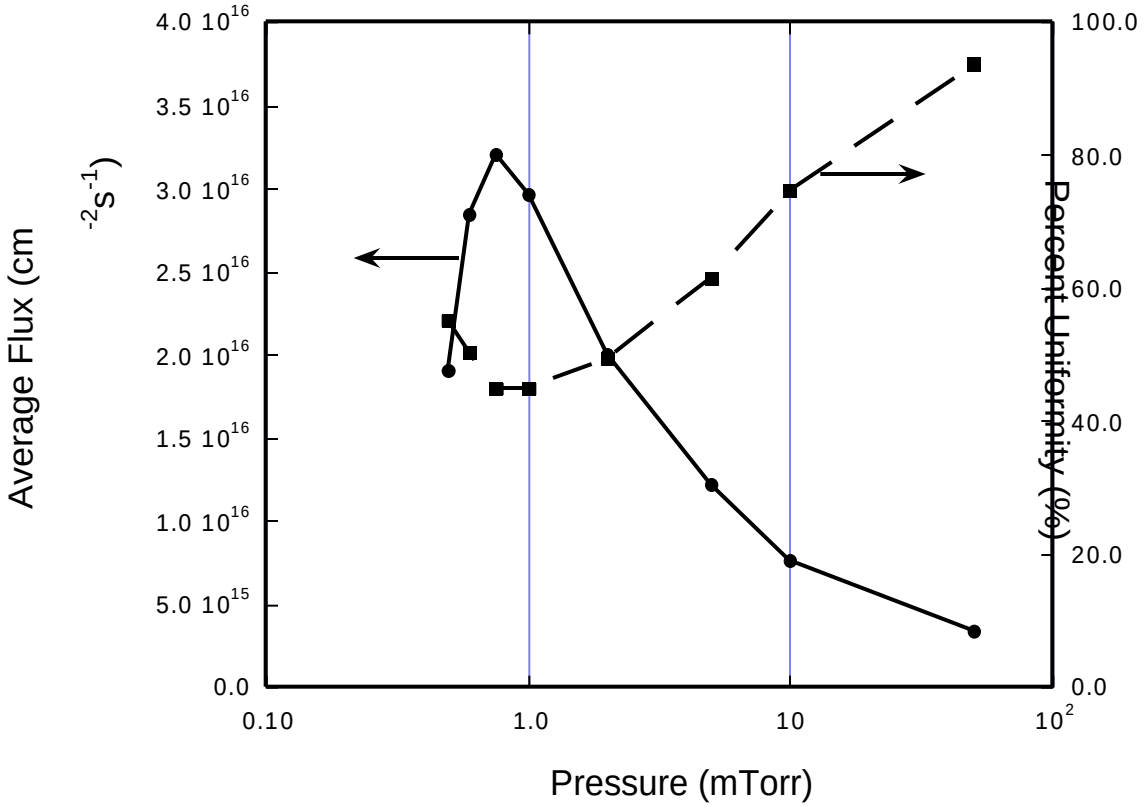

Figure 3.42 Average ion flux and the percent uniformity of the ion flux to the substrate as a function of pressure.

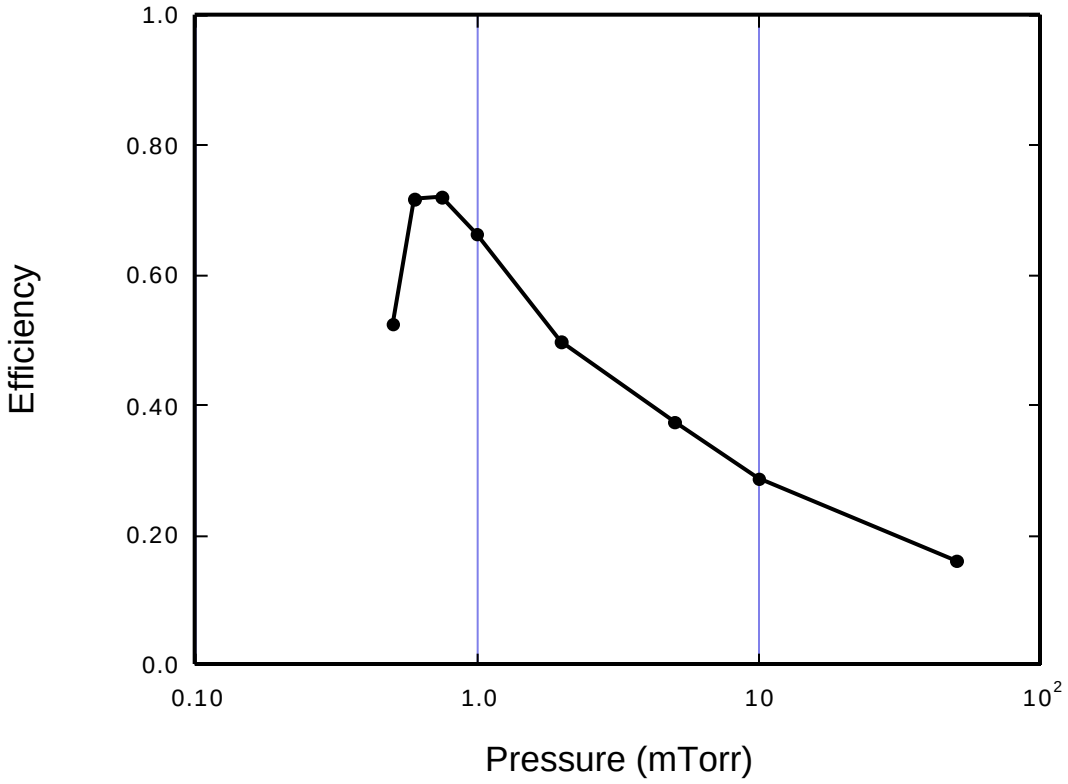

Figure 3.43 Efficiency as a function of pressure. The “efficiency” is defined as the product of the average flux and the percent uniformity.

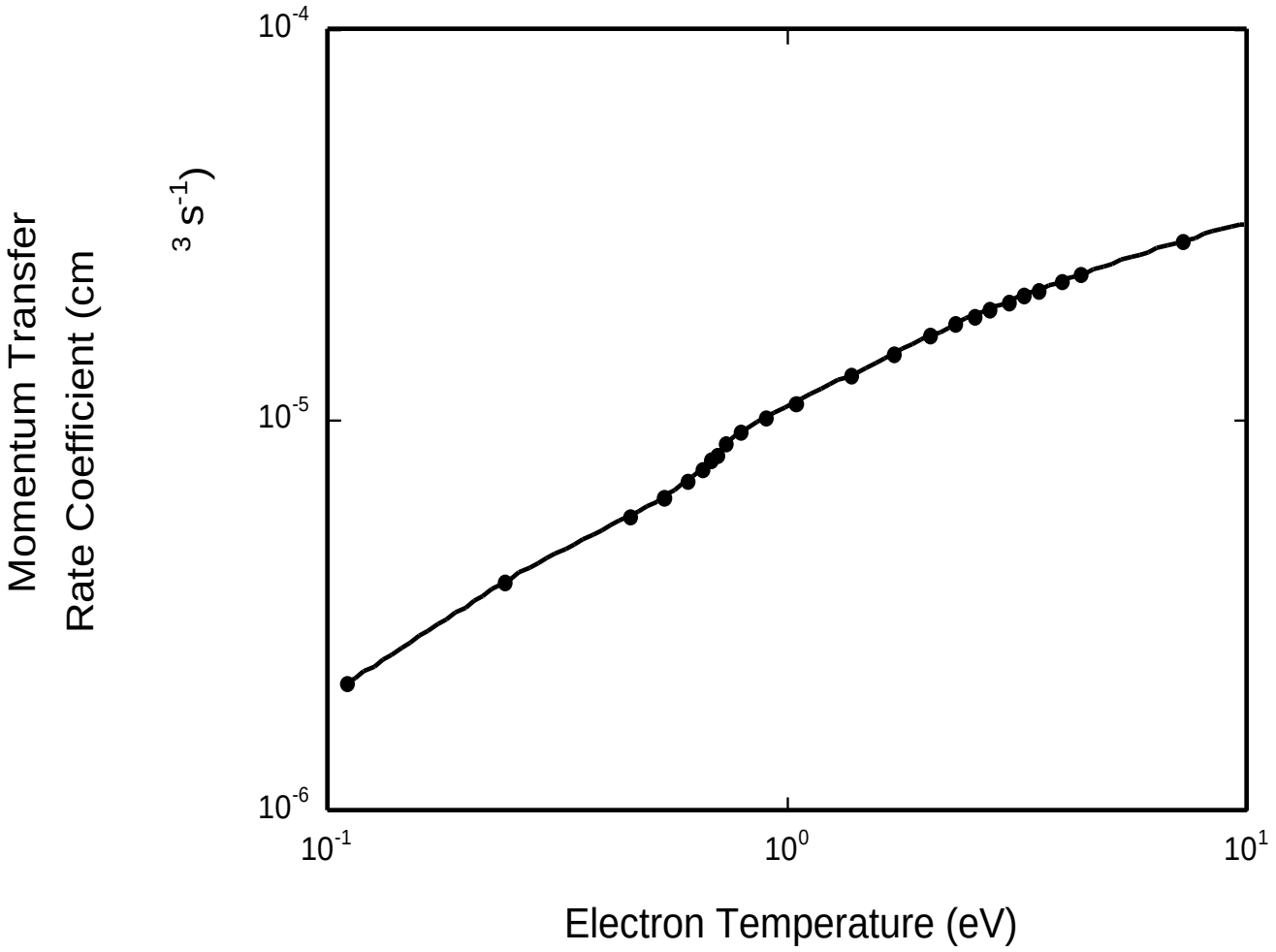

Figure 3.44 Momentum transfer rate coefficient as a function of electron temperature.

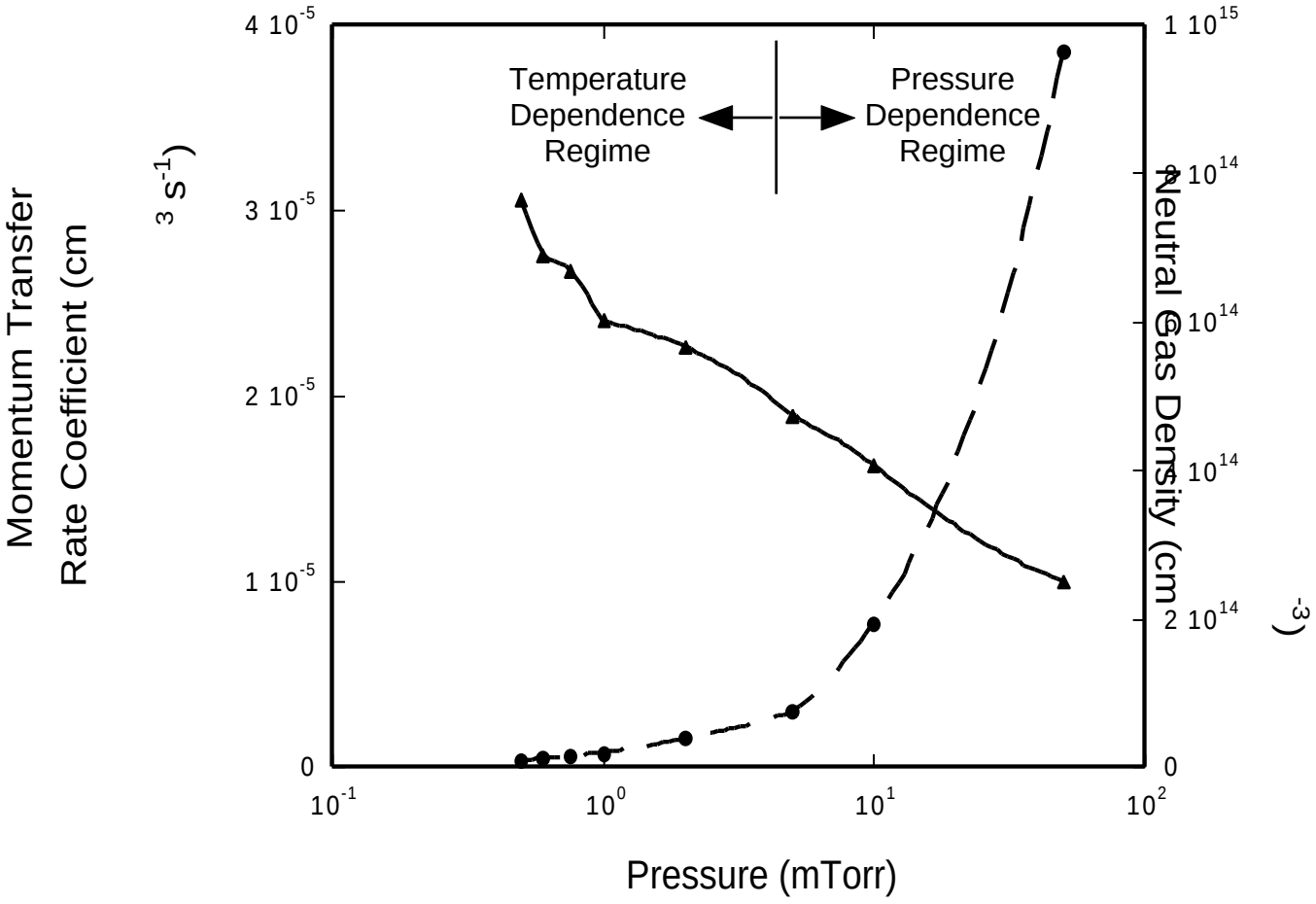

Figure 3.45 Average mometum transfer rate coefficient and neutral gas density as a function of pressure.

IV. Conclusions

A finite-difference-time-domain (FDTD) simulation for microwave injection and propagation has been developed to examine the spatial coupling of microwave radiation to the plasma in an electron cyclotron resonance (ECR) reactor. Microwave coupling is a concern due to issues related to the uniformity of dissociation, electron heating, and ultimately process uniformity. The FDTD simulation was incorporated as a module in the 2-dimensional Hybrid Plasma Equipment Model (HPEM). Plasma dynamics were coupled to the electromagnetic fields through a tensor form of Ohm's law. Power deposition calculated in the FDTD module is then used in solving the electron energy equation. Consequences of mode structure, magnetic field configuration, and operating conditions on plasma parameters and fluxes to the substrate in ECR sources for materials processing were examined with this model.

The computed radial distribution of the ion saturation current density showed good agreement with experiment. The radial ion saturation current density in the case of the TE_{01} mode was uniform within 5% over an 8 inch diameter. Parametric studies in which microwave power was varied showed that theoretical predictions followed experimental trends, with the saturation current increasing linearly in proportion to microwave power.

Results with varying magnetic coil configurations showed that when operating with the subcoil the ion flux to the substrate reflected the reactor ion density profiles. An increase in power level leads to the enhancement of any non-uniformities present in the

flux profile. At higher pressures the sensitivity of the ion flux to activation of the subcoil is decreased and the uniformity of the ion flux is increased.

It was shown that the higher order circular TE_{on} modes have several off axis peaks in the electric field depending on the harmonic mode, *n*, used. The power deposition exhibits a semi-Lorentzian line shape in the axial direction and reflects the incident electric field profile in the radial direction. However, production of several off axis peaks in the power deposition does not necessarily enhance the uniformity of the flux incident onto the substrate. The distance of the resonance zone to the substrate and the magnetic field configuration determined the extent that higher order modes enhanced uniformity of the flux to the substrate. Overall, diffusion losses are enhanced in both the low and high pressure regimes. Results suggest that there is an optimal pressure for charged particle confinement, maximizing ion flux to the substrate surface, and flux profile uniformity.